POLITECNICO DI TORINO

Corso di Laurea Magistrale in Ingegneria Aerospaziale

Tesi di laurea magistrale

Vibroacoustic analysis in the cabin of a regional turboprop with innovative materials by Actran

Candidato:
Martino Carlo Moruzzi

Relatore:
Prof.ssa Maria Cinefra

Correlatore:
Dott.ssa Ing. Sara Bagassi

Luglio 2019

Abstract

The main goal of this work is to evaluate the acoustic comfort, hence the sound pressure levels, in the cabin of a regional turboprop under multiple tonal and broadband noise components characterizing the noise generated by the engines during cruise flight conditions. In particular, we aim to show the higher acoustic performances of innovative passive Noise & Vibration technologies, such as metamaterials, with respect to classical soundproofing solutions. Furthermore, the effect of windows on acoustic pressure in the cabin is calculated in order to evaluate the possible advantages of a windowless configuration, in terms of noise reduction.

Multa, quae impedita natura sunt, consilio expediuntur.

Hannibal Barca, quoted in Tito Livio, XXV, 11.

Contents

List of Figures

List of Tables

Introduction

The main goal of this work is to evaluate the acoustic comfort, hence the sound pressure levels perceived by human ear (dBA scale), in the cabin of a regional turboprop under multiple tonal and broadband noise components characterizing the noise generated by the engines during cruise flight conditions. In particular, we aim to show the higher acoustic performances of innovative passive Noise & Vibration technologies, such as metamaterials, with respect to classical soundproofing solutions. Furthermore, the effect of windows on acoustic pressure in the cabin is calculated in order to evaluate the possible advantages of a windowless configuration, always in terms of noise reduction.

Actually, there is a lack of reliable and useful numerical models, valid for innovative materials, able to predict the structural response and the radiated acoustic power. The availability of a numerical tool, especially for regional aircrafts which are subject to very different customer requests, is a fundamental need together with the confidence of the users of such tools who should have the ability for a correct, realistic interpretation of the results produced numerically. In parallel, the possibility of studying innovative materials and configurations is a driving factor for approaching the problem of the aircraft interior noise.

Since acoustic loads considered stand in low-frequencies range, Finite Elements Method (FEM) can be adopted for the present vibroacoustic simulation. In this framework, Actran is a powerful FEM tool of MSC Software for the acoustic and vibroacoustic analysis of complex structures, accounting for various geometries, load conditions and innovative materials: among these, porous materials, 3D orthotropic materials and materials with unconventional properties such as metamaterials that can present negative, complex and frequency-dependent mechanical and mass properties. Moreover, this software allows different types of analysis which have been validated through many applications, as direct frequency response and modal extraction.

In this study, propeller aerodynamic loads in cruise conditions have been computed with a Blade Element Momentum Theory (BEMT) and they are used for computing the acoustic pressure on the fuselage skin through a FW-H (Ffowcs Williams and Hawkings) integral approach. The first three Blade Passage Frequencies (BPF) at 100 Hz, 200 Hz and 300 Hz, being the dominant contribution, have been converted in acoustic loads for the subsequent vibroacoustic analysis. Sandwiches with metamaterial core are employed as lining panels of the cabin for improving sound absorption through the fuselage and the averaged interior noise level at seated person ear height is numerically evaluated. The computational model is a 20 meters fuselage, composed by structural (panels and beams) and acoustic (air cavities) elements. The results obtained by Actran reveal a significant reduction of Sound Pressure Level in overall the frequency range and in the whole cavity considered over the cabin by the use of metamaterial. While for the windowless configuration, the results reveal that the absence of windows do not lead to significative reduction of sound pressure in the passengers cabin.

In the first chapter of this thesis, the physical phenomena, at origin of cabin noise, is discussed, focusing on acoustic sources, parameters, used to define the noise. In the second chapter the technologies applied to reduce cabin noise (metamaterials and windowless configuration) are described, within their framework, moreover a brief description of the mathematical model, that describe the physical problem in the field of vibroacoustics, is given. The third chapter is about the simulation tool: MSC Actran, particularly regarding on the element size criterion and on interfaces between structure and fluid. The model for simulation is defined in the fourth chapter, both from a physical (materials, geometry, etc) and from computational (in Actran) point of view, particularly it is explained how pressure loads are applied on the fuselage model in Actran. In this chapter the reader can also find information about mesh quality and modal extraction performed on this model. In the last chapter the results of the analysis are showed in terms of SPL (sound pressure level) and OASPL (overall sound pressure level).

Chapter 1

Aircraft's noise: overview

1.1 Historical review

The noise problem has affected some engineers since the dawn of aviation, as described by Basset and Zand [1]. The first studies, despite the few data available, began in 1928-1929, with poor results. In 1932 the Sperry Gyroscope Company renewed previous efforts by carrying out a series of in-cabin measurements on the EAT Condor (numbers 2 and 5), getting the results in Fig. 1.1. It was possible to arrive at some important results, both from the point of view of understanding the phenomenon and the reduction of noise in the cabin which decreased from 97 dB to 85 dB.

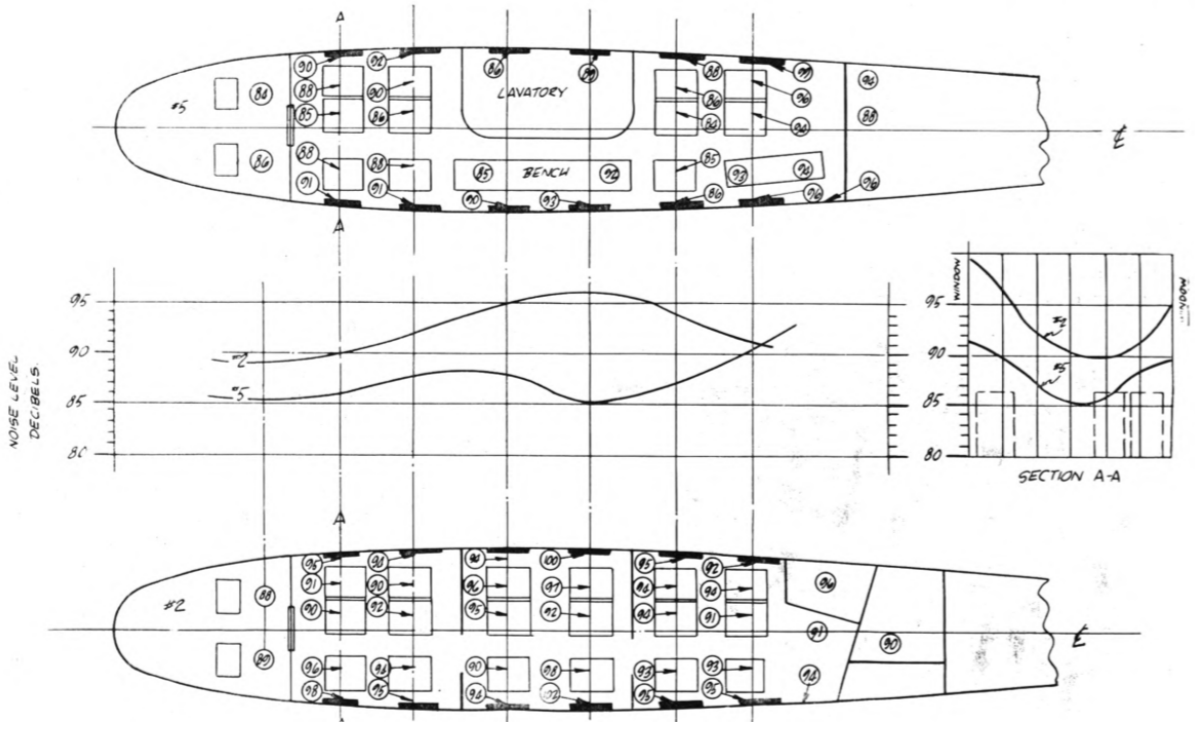

Figure 1.1: Sound pressure level distribution on Condor numbers 2 and 5.

In the sixties, in the United States, there are the first FAA regulations regarding external noise.

However, only in the last twenty years effective studies have been carried out to understand how noise is generated and spread in the cabin [2], how to reduce it [3, 4] and the effects on the

human body [5].

Finally, in the last few years, comfort in the cabin is becoming an important requirement, leading to the realization of future regulations and objectives, also at a global level, reversing the sentence of Basset and Zand [1]: "No attention has been paid to noise, however, until now. Pilots and early passengers took it for granted that the noise was just an unavoidable evil that went with flying and high speed." Within this wave of studies there is the Clean Sky 2 project, and in particular CASTLE (CAbin Systems design Toward passengers welLbEing).

An example of modern insulation system is shown in Fig. 1.2[1], produced by Aearo Technologies LLC.

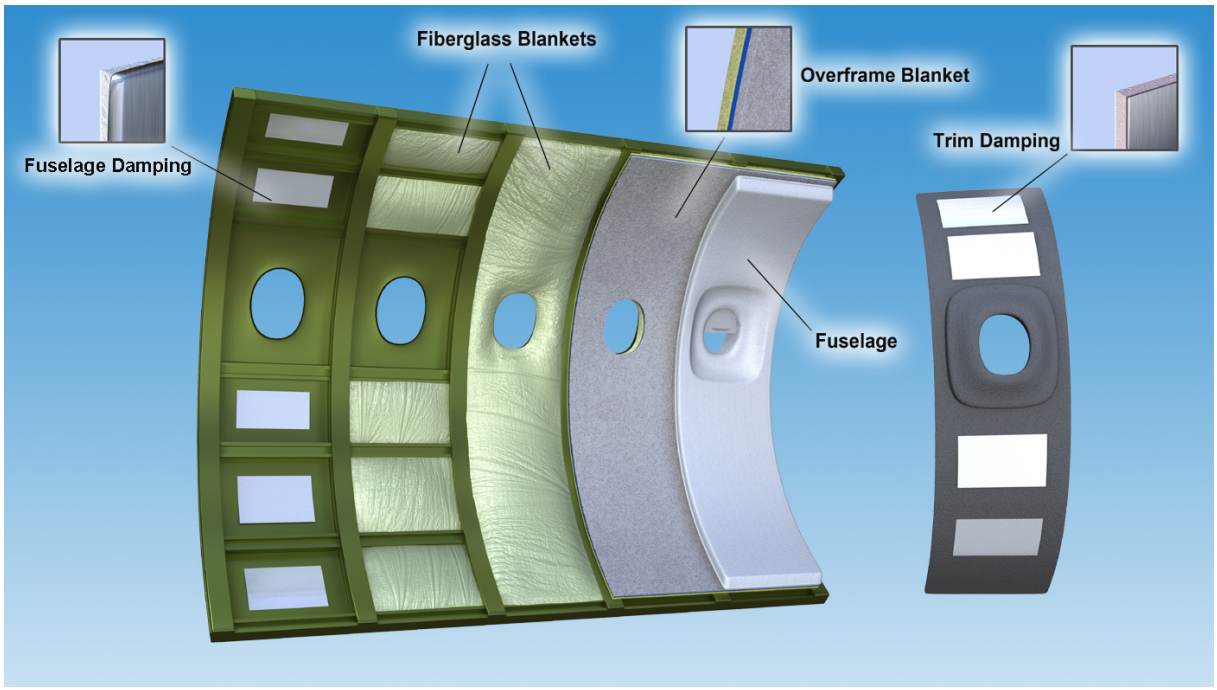

Figure 1.2: Thermal acoustic system from Aearo Technologies LLC.

1.2 Clean Sky 2 and CASTLE

"Clean Sky 2 Joint Undertaking (CSJU) is a successful public-private partnership between the European Commission and the European aeronautics industry that is on the way to achieving its environmental performance targets." [6]. The second phase Clean Sky 2 is built on the success of the first phase Clean Sky 1:

- continuing to integrate breakthrough technologies in aircraft;
- exploiting innovative configurations in aircraft, enabling changes in environmental and economic performance.

The purpose of CSJU is to help the environment. Through the technologies developed by Clean Sky 2, the aircrafts will be able to:

[1] https://earglobal.com/en/aircraft/applications/fuselage extracted on the 15th of March 2019.

- cut fuel burn and related CO_2 emissions by 20-30%;
- cut noise levels (compared to 2014) by a similar amount.

An internal project of Clean Sky 2 is referred to turboprop regional aircrafts. The purpose is to increase the regional aviation's potential, using innovative technologies, to more than 10000 units over the 2025-2050 timeframe and to rise the market-share of a new European regional turboprop program to 30-40%, doubling what it is today [7]. An important aspect for modern aviation, both for turboprop and for turbojet aircrafts, is the comfort in the cabin, which is discussed in the CASTLE project, inside Clean Sky 2.

In the CASTLE proposal the aim, relatively to regional aircraft, is "to achieve an improved and optimized passengers cabin environment by means of an innovative and integrated design approach mainly based on Human factor issues regarding ergonomics, anthropometrics, as well as effects of vibration, noise and motion on passenger, crew and PRM[2]; Noise and vibration, including active and passive treatments; Environmental friendly cabin materials to improve human interaction with cabin materials in terms of comfort and health issues; Safety-related systems, including fire worthiness concepts and procedures; Main cabin system (cabin lighting, passengers seats, galley, lavatory, lining panels, stow bins, thermal insulation blankets) interfacing with passenger, flight attendant and PRM in their living and operative spaces."[8]. In this work we study and evaluate passive treatments to mitigate noise and vibration, see Sub Topic 2 in [8].

The objective, relatively to noise and vibration (N&V), is "to reach several enhancements for the Noise & Vibration of the cabin interiors items." [8]. The strategic topic (ST) are shown in Fig. 1.3. From the CASTLE proposal the following solutions emerge for the reduction of noise in the

Objective	Description
ST2 - OB1	Multidisciplinary and concurrent optimization of human-centered N&V treatments
ST2 - OB2	Passive and active N&V control treatments with respect to human perception and psychoacoustics
ST2 - OB3	Novel NVH design of comfortable seats
ST2 - OB4	Optimization and efficient use of passive and active means by consideration of perception related acoustics including the early primary structure design
ST2 - OB5	Various contributions focused on multifunctional design and optimization

Figure 1.3: Objectives of Acoustic - Noise & Vibration for Regional Aircraft, strategic topic 2.

cabin, "novel concepts for soundproofing to increase the sound insulation without added mass fuselage-trim side wall" [8]:

- composite orthotropic skin and trim (e.g. linings) panels embedding viscoelastic layers;
- Passive Dynamic Vibration Absorbers based on "wire rope absorber";
- metallic foams and sandwich panels, as metamaterials structures;
- Active Structural Vibration Control to isolate trim panel by acting on rods/connectors;
- Active Structural Acoustic Control on panel and cavity;
- Active Dynamic Vibration Absorbers (ADVAs);

[2]PRM: people with reduced mobility.

- active constrained layer damping patches .

Particularly in this work it has been considered the third solution: metamaterials structures.

1.3 Noise generation

1.3.1 Sources

Commercial aircrafts generate noise, that spreads in the passengers cabin. This noise could be classified referring to the physical phenomena responsible of its generation or referring to the source understood as a component of the aircraft.

From a physical point of view, referring to [9], the noise is generated by:

- fuselage boundary layer;
- turbojet exhaust;
- turbo-machinery;
- cabin conditioning and pressurization system;
- structure-borne noise, due to the interaction between the fluid and the structure (vibro-acustic);
- aerodynamic flow;
- other noise sources (hydraulic and electrical actuators, etc.).

The first two sources are the most important, however only the first has been considered in this thesis together with the structure-borne noise. In general noise is transmitted from the engine (or from other source) through air-borne paths and structure-borne paths (engine mount, wing, fuselage sidewall, etc.).

The mechanical component responsible for producing noise, referring to [10], are the following (Fig. 1.4):

- landing gear, the noise is produced by the interaction of landing gear with a turbulent flow;
- high-lift devices (flaps, slats and Krueger), for slats and flaps the noise is produced by the presence of turbulence in the gap;
- wing and tail, the turbulence in the leading edge is responsible of noise generation;
- spoilers and speed breaks, which lead to the separation of the flow;
- engine, which involves different acoustic phenomena for its different components (fan, outlet jet, combustion chamber, turbine and compressor).

The importance or simply the presence of each component in noise generation depends on the operating conditions, for example the landing gear becomes an important source only during the final approach. The acoustic phenomena linked with these components are not always completely

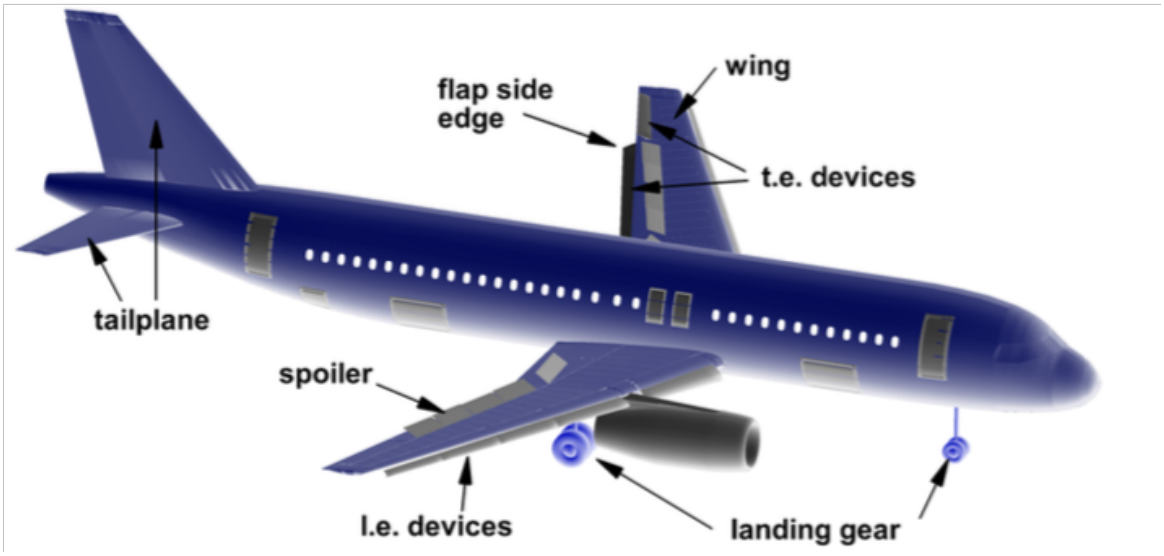

(a)

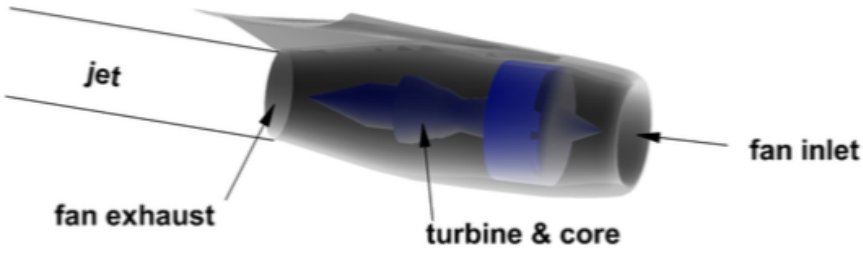

(b)

Figure 1.4: The various noise generating components on-board of an aircraft. (a) Airframe contribution. (b) Engine contribution.

understood and so it is difficult to quantify their noise production. It must be considered also the interaction and installation effects (jet with flap, engine pylons with wing, spoiler on flap and slat, shielding effect of engine noise). The engine is the most important source and so it is the only source considered in this thesis. To these sources we must be add the airflow noise that it is not linked with a specific component and the noise generated inside the passengers cabin (air conditioning system and human noise) and inside the cockpit. Another source of noise, in the airport, is the Auxiliary Power Unit (APU).

Due to the high number of components involved there are many different parameters that influence the intensity of the noise in the passengers cabin, starting with the type of aircraft (turboprop or turbojet, see section 1.3.2) and the flight phase (take-off, landing, cruise, etc.) up to the specific features of the single components (aerodynamic, geometric, structural, etc.).

1.3.2 Turboprop's noise level

Applying the Lighthill equation [11], it is possible to preliminary estimate the acoustic intensity I as a function of the engine or propeller diameter D. The hypothesis are low Mach number M (and speed U), so constant density ρ, and constant thrust $T \propto \rho \cdot U^2 \cdot D^2$. A quadrupolar source, due to turbulence, is used, and so we obtain $I \propto D^2 \cdot U^8$. Considering two engines with different

diameter $D_2 = k \cdot D_1$ where k is a proportionality constant, the speed could be expressed through thrust: $T \propto \rho \cdot U_1^2 \cdot D_1^2 = \rho \cdot U_2^2 \cdot D_2^2$ so $U \cdot D = cost$ and a relation for the two speeds is obtained:

$$U_2 = \frac{U_1}{k} \, . \tag{1.1}$$

Then it si possible to calculate the ratio of intensities:

$$\frac{I_1}{I_2} = \frac{D_1^2 \cdot U^8}{D_2^2 \cdot U^8} = k^6 \tag{1.2}$$

The acoustic power is expressed as $P \propto (U \cdot D)^3$ and therefore the ratio is obtained:

$$\frac{P_1}{P_2} = \frac{D_1}{D_2} = k \tag{1.3}$$

For example, if the diameter of the engine is doubled ($k = 2$), the intensity is increased of 18 dB and the acoustic power of 3 dB. This preliminary result shows as a turboprop, at same level of thrust, is more noisy than a turbofan, because it displays a major front diameter. However in this simple analysis, the turbine and fan noise are not considered, and also the isotherm nature of the outlet jet.

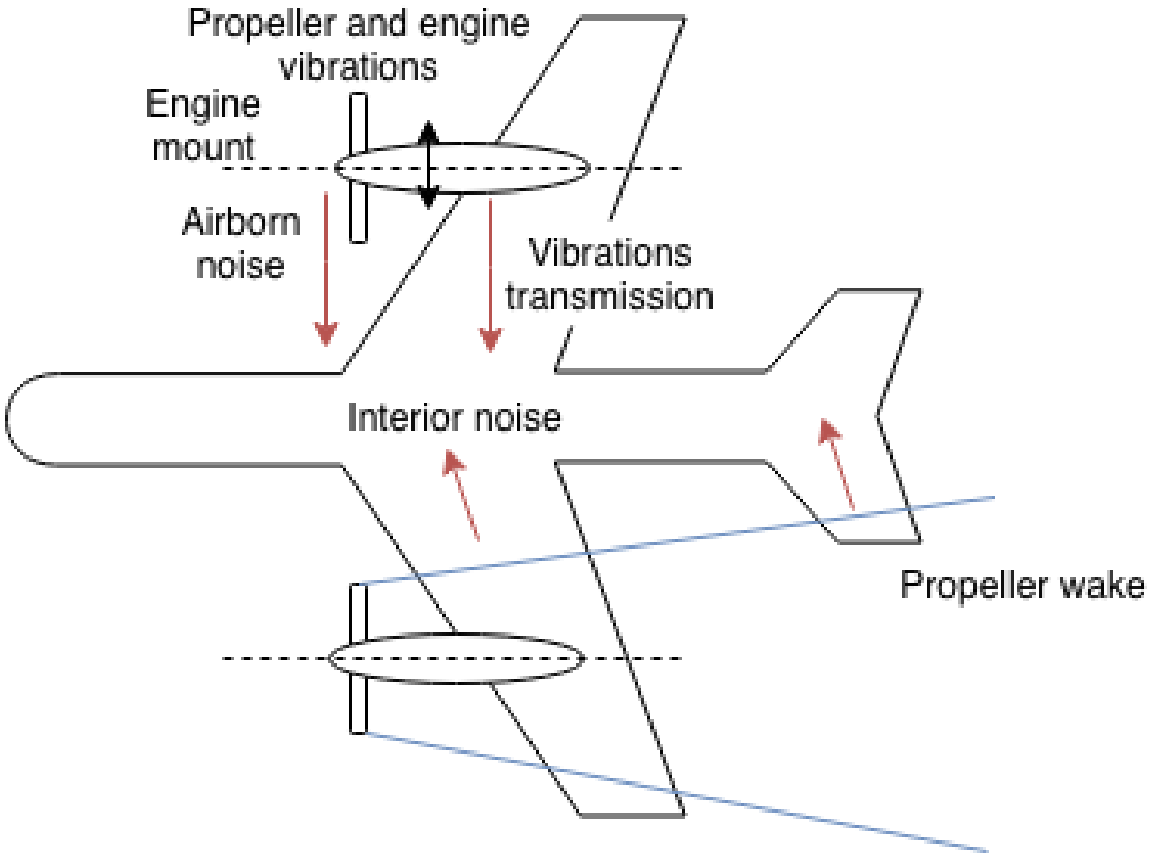

Figure 1.5: Effects of the propeller on the noise in the passengers cabin.

In this work, a turboprop aircraft in cruise condition is considered. For this kind of aircraft, the near field excitation is mainly due to the propeller and therefore the major part of the acoustic energy is concentrated in the low frequencies range (0-300 Hz), although for last generation turboprop aircraft, the near field noise excitation is also due to turbulent boundary layer.

Therefore this low frequency nature of noise is particularly troublesome because is conventionally linked with not light solutions, in terms of weight. Furthermore there could be a resonance between natural frequencies of the skin panel and the propeller tonal frequencies, that increases noise transmission. The only considered source is the propeller, which noise transmission in the passengers cabin is shown in Fig. 1.5.

There are no regulations concerning cabin noise. Noise limitations are dictated by passengers comfort and safety. As reference value, cabin pressure level must be comprised between 60 and 88 dB. A long exposure to pressure level of 85 dB could cause hearing loss, within fatigue and reduction of concentration, not only for the passengers but also for the crew.

1.4 Cabin noise parameters

1.4.1 The Decibel scale

The decibel (dB) is used to represent, in logarithmic scale, the ratios of electromagnetic stresses and power waves or mechanical pressures and wave powers. The dB (with no other letter) it is a relative quantity and represents a ratio of homogeneous quantities on a logarithmic scale. It is a pure number and therefore does not have a physical dimension. It becomes an absolute value of a physical quantity and therefore it has physical dimensions, when the ratio refers to a defined absolute value, called reference value. In acoustic it is called Sound Pressure Level (SPL):

$$dB_{SPL} = 20 \cdot \log_{10} \frac{p}{p_{ref}} \tag{1.4}$$

where $p_{ref} = 20$ μPa for air and p is the pressure in Pascal. Therefore we have the following equivalence 0 $\mathrm{dB_{SPL}} = 20$ μPa.

Based on statistical values, the average listener has a sensitivity to perceive variations in pressure levels in the micro-Pascal order. Therefore we choose, as a reference, the pressure of 20 μPa at the frequency of 1000 Hz, which corresponds to the minimum value convertible into a subjective sound sensation for the average of the generality of people aged between 18 and 38 years. The maximum pressure value that causes pain sensations corresponding to about 20 Pa, was also statistically measured. Thus the dynamics of the human ear receiver covers, in terms of ratio between the maximum and minimum value of pressure, as many as six orders of magnitude (20 / 0.00002), hence the convenience of expressing the measurement of the pressure level in a logarithmic scale.

Therefore the $\mathrm{dB_{SPL}}$, the unit of measurement of sound pressure level, was defined as the ratio between the average value of the integrated pressure variation, over a given time, and the variation in pressure level, established as a minimum.

Conventionally the sound pressure level is defined as omitting the subscript:

$$SPL = 20 \cdot \log_{10} \frac{p}{p_{ref}} \text{ dB} \tag{1.5}$$

where the pressure p in Pascal depends on the given frequency.

We could define the Overall Sound Pressure Level (OASPL) as:

$$OASPL = 20 \cdot \log_{10} \frac{\sqrt{\int_{f_{min}}^{f_{max}} p^2 dp}}{p_{ref}} \text{ dB} \tag{1.6}$$

where f_{min} and f_{max} are minimum and maximum frequency on which the pressure p is calculated. Finally, the Transmission Loss TL is defined as:

$$TL = 10 \cdot \log_{10} \left| \frac{W_i}{W_t} \right| \text{ dB} \tag{1.7}$$

in which W_i is the power of incident wave coming towards the defined region and W_t is the power of transmitted wave going away from the defined region.

1.4.2 Sound weighting factors

The human ear does not have a constant frequency response. Indeed it has the maximum sensitivity between 800 Hz and 2000 Hz and attenuates strongly the sounds below 400 Hz. Furthermore, the amplitude response towards frequency is not linear and varies according to the average noise level of the environment. So there are curves called equal-loudness contours (or isophonic) which indicate the dB_{SPL} value necessary to perceive a sound always at the same loudness along each curve. We refer to the work of Fletcher and Munson [12] in 1933 and the updated work of Robinson and Dadson [13] in 1953. The obtained curves are compared in Fig. 1.6

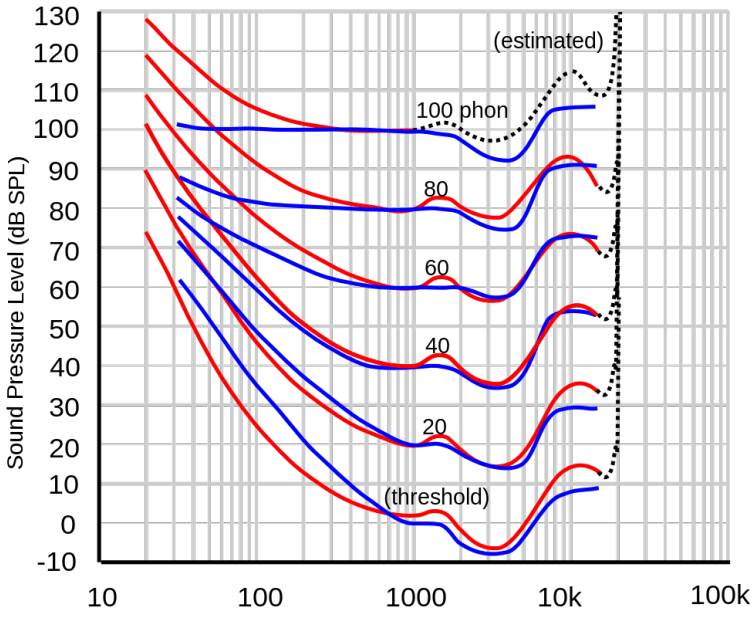

Figure 1.6: Equal-loudness contours.

These curves allow to have a reference how the human ear reacts to different frequencies in terms of perceived sound pressure. It is noted that the ear has a different perception of sound intensity with varying frequency. The reference frequency for each curve is 1 kHz and at this frequency,

the dB_{SPL} value is equal to the value that identifies a particular curve, that takes the name of phon.

In order to obtain an instrumental sound pressure measurement as similar as possible to the acoustic sensation of the human ear, it would be necessary to combine the measuring instrument, the dB_{SPL} and the thirteen filters. Each of these filters have the reversed trend of the amplitude response towards the human ear, based on the values of the environmental phons.

In practice, the pressure level is measured after inserting four types of normalized equalization, called type filters: A, B, C and D. The weighted pressure levels, measured downstream of the insertion of the these filters, are indicated as:

- dBA, the response curve corresponds to the isophonic curve at 40 phons of the human ear and allows accurate measurements of modest sound pressures such as those generated during a normal conversation. It is the most used filter for several noise pollution laws;
- dBB, the response curve corresponds to the 70 phons curve of the human ear. It is suitable for sound pressure measurements between 55 and 85 dB_{SPL};
- dBC, the curve has an almost costant response. It is suitable for measurements greater than 85 dB_{SPL};
- dBD, used for very high sound pressure measurements as in airports.

In Fig. 1.7 the weights A, B, C and D are reported.

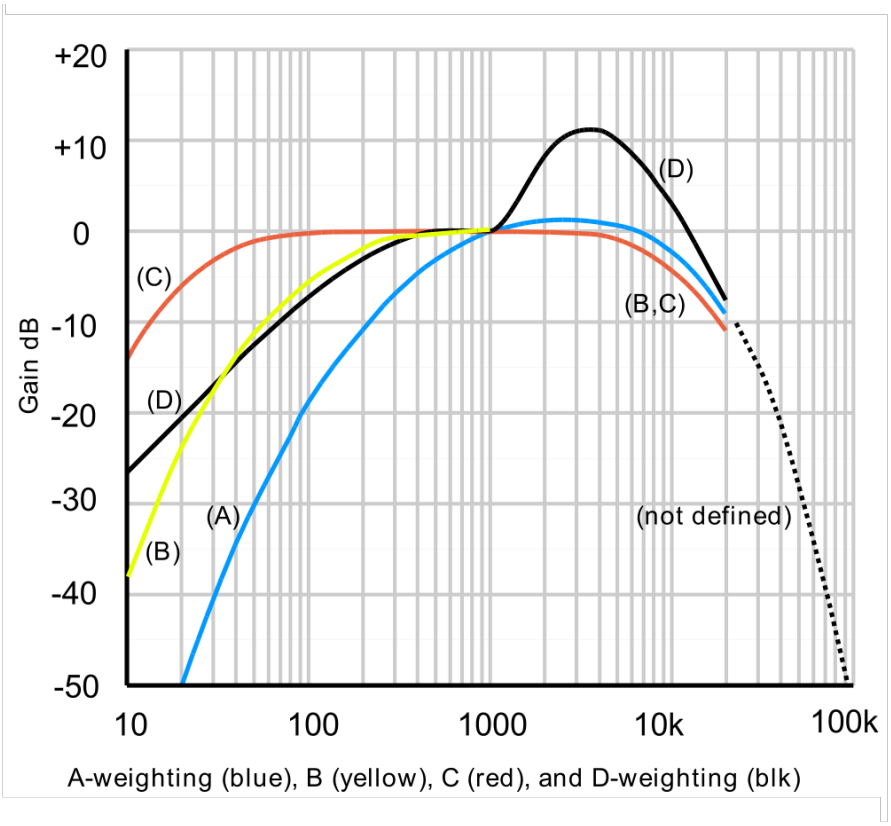

Figure 1.7: The curves of the A, B, C and D weights across the frequencies range from 10 Hz to 20 kHz.

1.4.3 Speech interference level

Speech Interference Level (SIL) is the arithmetic mean of unweighted sound pressure level in three or four octave bande in the frequency range from 500 Hz to 4 kHz. Particularly a SIL variant is used: SIL3, that represents the arithmetic mean of 1 kHz, 2 kHz and 4 kHz octave bands.

In this work SIL3 is not used because it needs measurements at high frequency, while we concentrate on low frequency.

Chapter 2

Aircraft's noise: solutions

2.1 Noise effects on health

The effects of noise are the consequences on the physical and psychological health of regular exposure at high and constant sound levels.

The first possible disease is the noise-induced hearing loss, that could be caused by a one-time exposure to an intense impulse sound or by steady state long-term exposure with sound pressure level higher than 75-85 dBA. The decrease in hearing is due to the loss of hair cells, responsible for the transmission of acoustic information to the central nervous system, which in mammals can not longer regenerate.

There are also non-auditory health effects, as:

- annoyance, that might be accompanied by negative response and stress-related symptoms;
- cardiovascular diseases, in fact a long-term exposure to environmental noise could affects the cardiovascular system and causes disease as hypertension, ischemic heart diseases and strokes;
- decrease of cognitive performance, particularly on children;
- sleep disturbance, that is the most annoying non-auditory effects of environmental noise exposure, in fact maximum sound pressure level of 33 dBA could cause, during sleep, physiological reactions including autonomic, motor and cortical arousals;
- other effects, not yet fully understood or related to particular places, as hospital.

For more detail on health effect from noise see the work of Basner et al. [14].

Furthermore noise could have negative effects on animals as felines or canines.

2.2 Metamaterials

2.2.1 Metamaterials in electromagnetics

Metamaterial, in electromagnetic, is a material on which it is possible to tailor and manipulate the wave properties, enhancing performances and lowering weight and size [15]. They are artificial structures with periodically or non-periodically arranged sub-wavelength elements. The permittivity ε and the permeability μ of these materials could be influenced through inclusions, as in composite materials, but artificially fabricated in a specified host medium or surface. In this way, it is possible to have a large collection of degrees of freedom, relatively to both the host materials and the inclusions, Fig. 2.1.

In Fig. 2.2 it is presented the classification of metamaterial host, using macroscopic permittivity ε and the permeability μ of these materials.

Some applications of metamaterial to control electromagnetic flow are, for example, the perfect lens and the invisibility cloaks.

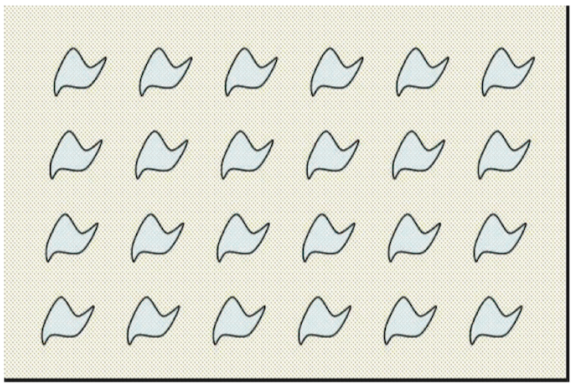

Figure 2.1: A generic metamaterial with inclusions inside a host material.

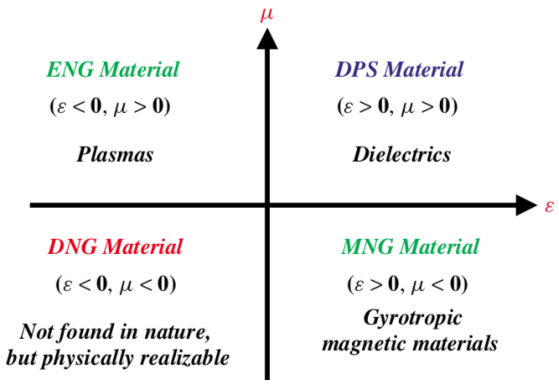

Figure 2.2: Classification of metamaterial hosts.

2.2.2 Metamaterials in acoustics

The Acoustic MetaMaterials (AMMs) have the same paradigma of their electromagnetic relatives. In fact they try to regulate the acoustic behavior, resulting in negative effective mass density and negative effective bulk modulus based on localized resonance mechanisms and dispersion properties [16]. Furthermore AMMs, due to negative mass density, demonstrate excellence performances at low frequencies.

A clear description of AMMs is made in *Review on acoustic metamaterials of Josè Sanchez-Dehesa*, as shown in Fig.. 2.3, within the homogenization process. AMMs are classified in four categories based on the bulk modulus and mass density, Fig. 2.4. In the next sections are presented the most relevant AMMs developed in last years, particularly referring to airborne noise. One important critical issue of this new material is the low structural characteristics, which is a major problem in the potential uses in aeronautics. In this work metamaterials are used to made the trim panel.

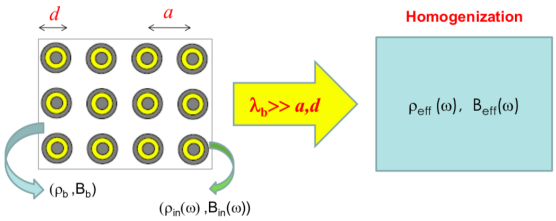

Figure 2.3: Acoustic metamaterial within the homogenization process.

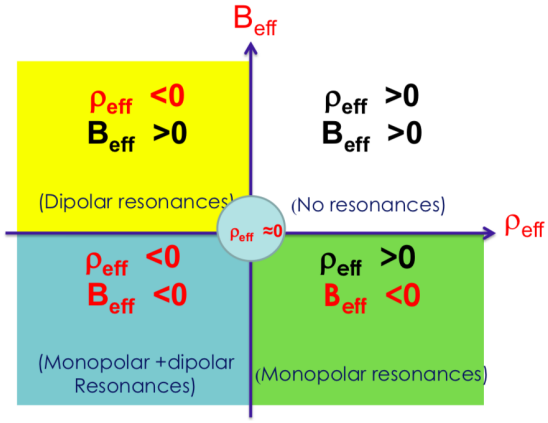

Figure 2.4: Classification of AMMs, Li and Chan, PRE (2004).

AMMs with negative mass density and density near zero

The first reported example is based on the work by Yang et al. [17]: membrane-type acoustic metamaterial with negative dynamic mass, operating in the 100-1000 Hz frequency range. This metamaterial is made by a circular elastic membrane (20 mm in diameter and 0.28 mm thick) with boundary fixed by a relatively rigid grid and with a small weight attached to the center. This small mass is a hard disk with a diameter of 6 mm, it is also possible to increase the disk mass up to 0.3 kg. Acoustic waves are incident perpendicular to the membrane plane. The results obtained in [17] are reported in Fig. 2.5(a). The results differ from the transmission amplitude predicted by the mass density law with the same average area mass density as the resonator, because the experimental results present two peaks at 145 Hz and 984 Hz and with a dip at 237 Hz, where the experimental value is 200 times lower than the expected value, implying near-total reflection at low frequencies. In Fig. 2.5(b) experimental results are compared with finite elements analysis. There are two transmission peaks at 146 Hz and 974 Hz, with a dip at 272 Hz. The effective dynamic mass ρ_{eff} is obtained using the following equation:

$$\rho_{eff} = \frac{\langle \sigma_{zz} \rangle}{\langle a_z \rangle} \tag{2.1}$$

in which $\langle \sigma_{zz} \rangle$ is the averaged stress and $\langle a_z \rangle$ is the averaged acceleration normal to the membrane plane at rest over the whole membrane structure. Fig. 2.6 shows the results of such calculations. Close to the transmission dip frequency, the effective dynamic mass turns from positive to negative. Then it jumps to positive at the dip frequency and then approaches the actual value of the system of about 0.1 kg/m^2 at high frequencies. In the first transmission peak, at low frequency, the corresponding eigenmode has the membrane and the weight vibrating in unison. In the second transmission peak, at high frequencies, the corresponding eigenmode has only the membrane vibrating while the central weight remains almost motionless. Therefore the first peak depends strongly on the central weight, while the second peak not. Using different masses there are the same feature of twin peak with a dip in between. The first transmission peak and the dip shift significantly to higher frequencies with the reduction of the mass, while the second transmission peak shifts only by a very small amount.

The second example is referred to the publication of Mei et al. [18]: dark acoustic metamaterials as super absorbers for low-frequency sound. The purpose of these material is to totally absorb

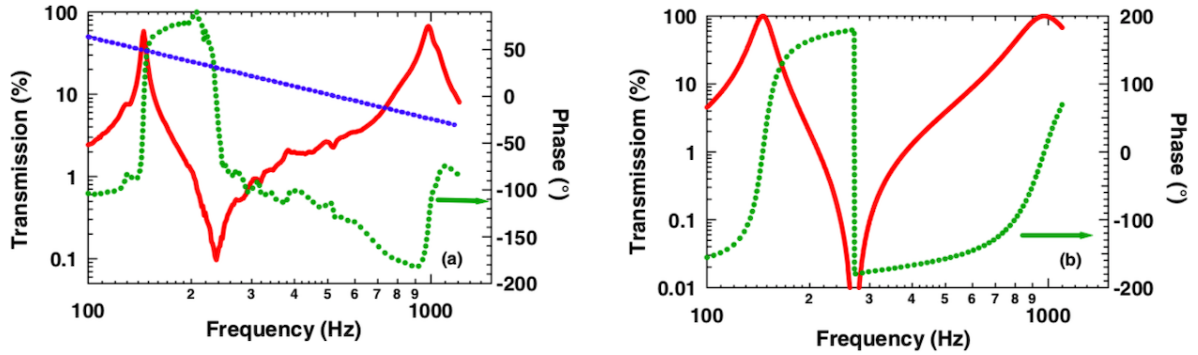

(a) **(b)**

Figure 2.5: (a) Experimental transmission amplitude (solid red curve), phase (dotted green curve) of the membrane resonator and the theoretical results for transmission amplitude (blue dashed line). (b) Theoretical transmission amplitude (solid red curve) and phase (dotted green curve) of the membrane resonator.

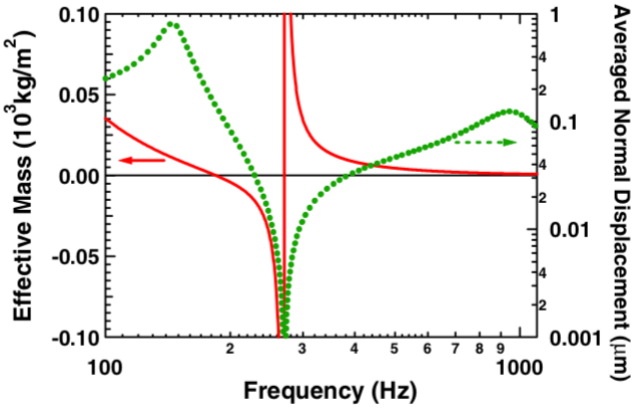

Figure 2.6: The calculated effective dynamic mass of the resonator (red solid curve, left axis) and the in-plane averaged normal vibration amplitude (green dotted curve, right axis).

low-frequency airborne sound at selective resonance frequencies ranging from 100 Hz to 1000 Hz. To reach this aim two sample were been used. A sample A comprising a rectangular elastic membrane that is 31 mm by 15 mm and 0.2 mm thick. The elastic membrane was fixed by a relatively rigid grid, decorated with two semi-circular iron platelets with a radius of 6 mm and thickness of 1 mm. The iron platelets are asymmetrical so as to induce flapping motion. The sample B has the following size: 159 mm by 15 mm and comprises 8 identical platelets decorated symmetrically as two 4-platelet arrays (with 15 mm separation between the neighboring platelets) facing each other with a central gap of 32 mm. Sample B is used to attain near-unity absorption of the low-frequency sound at multiple frequencies. They obtain [18] the following results:

- for sample A (Fig. 2.7) there are three absorption peaks around 172, 340, and 813 Hz. In the first peak more than 70% of the incident acoustic wave energy has been dissipated. That phenomena depends on the membrane resonance;
- using two layer of sample B with an aluminum reflector placed 28 mm behind the second layer (Fig. 2.8), eigenmodes mostly remain unchanged in character due to the similar layout, but it displays a better absorption performance. There are many absorption peaks

around 164, 376, 511, 645, 827, and 960 Hz. The absorption peaks at 164 Hz and 645 Hz are seen to be about 99%. So sample B absorb almost the total of low-frequency sound.

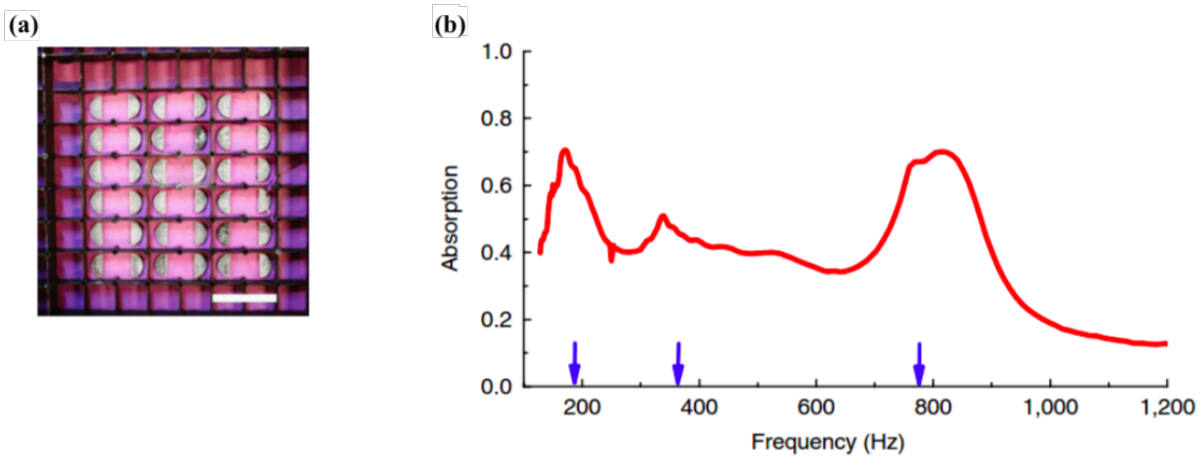

Figure 2.7: (a) Photo of sample A. The scale bar is 30 mm. (b) The measured absorption coefficient (red curve) and the positions of the absorption peak frequencies predicted by finite-element simulations (blue arrows).

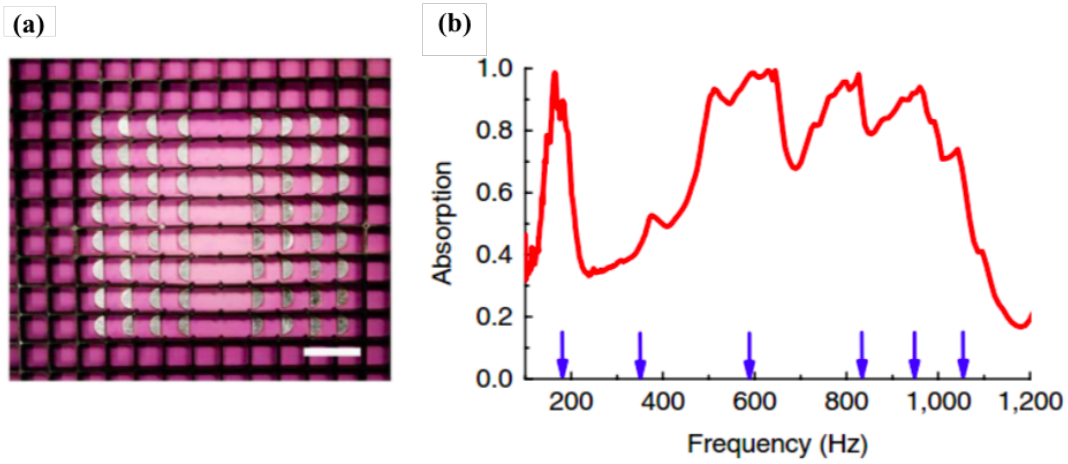

Figure 2.8: (a) Photo of sample B. The scale bar is 30 mm. (b) The measured absorption coefficient (red curves) and the positions of the absorption peak frequencies predicted by finite-element simulations (blue arrows).

In the end we focus on the work of Zheng et al. [19] about Zero-Refractive-Index (ZRI) material: acoustic cloaking by a near-zero-index phononic crystal. ZRI materials are unconventional materials that display zero refractive indices. The authors design and fabricate a near ZRI material using a phononic crystal (PC) composed of a square array of densely packed square iron rods in air. The results, relatively to the effective medium parameters of the PC, are reported in Fig. 2.9. The effective mass density ρ_{eff} and reciprocal of bulk modulus B_{eff} display a drastic change near the frequency of about 0.5437 c/a. Then, the effective mass density gradually increases as the frequency increases. At 0.5443 c/a, it is equal to zero. The transmission T and reflection R coefficients changes as the frequency increases. The transmittance comes to a peak value of 0.5443 c/a.

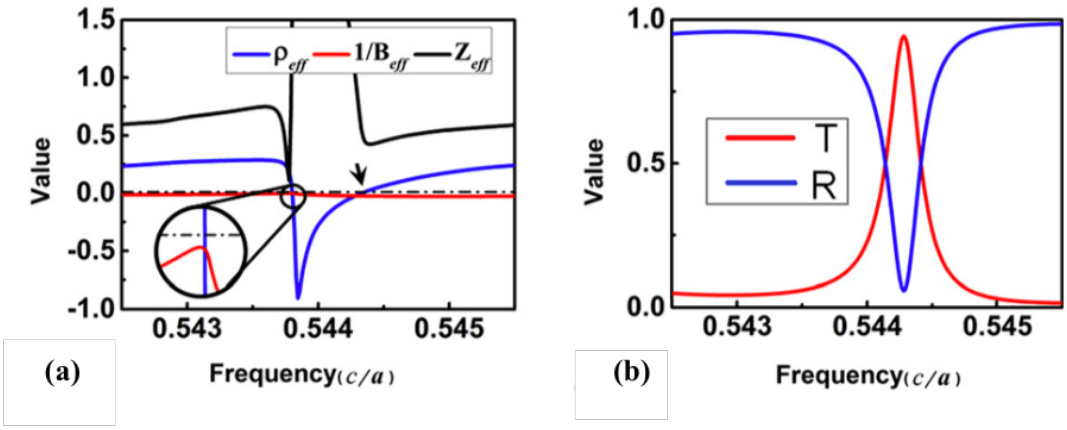

Figure 2.9: (a) Effective medium parameters of the PC. (b) The transmittance and reflectance changes with frequency.

AMMs with negative bulk modulus

As first example, for 1D AMMs, the work of Fang et al [20] is reported: ultrasonic metamaterials with negative modulus. In their paper the authors present a new class of ultrasonic metamaterials "that have strong dispersive characteristics of elastic modulus with subwavelength resonant structural units" [20]. The building blocks of this metamaterial is the Helmholtz resonator, Fig. 2.10(a). The sample is made of aluminium, consisting of a rectangular cavity of $3.14 \times 4 \times 5$ mm, and a cylindrical neck 1 mm long and 1 mm in diameter. The cavity and neck are filled with water, and are connected at the same side to a square water duct with a 4×4 mm opening. The resonators are placed in a periodicity of 9.2 mm. In Fig. 2.10(b) the effective modulus E_{eff} is reported as function of frequency obtained with a combination of many Helmholtz resonators.

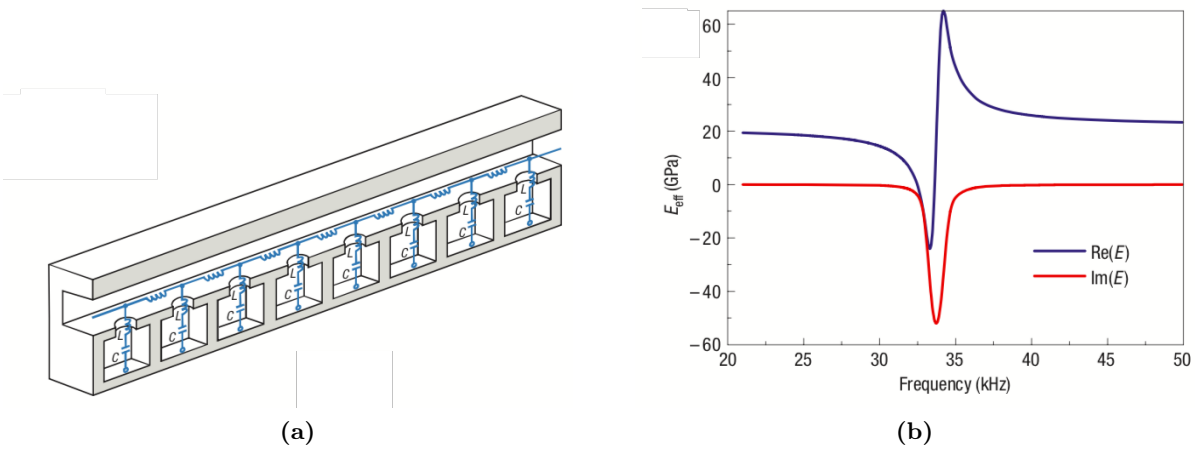

Figure 2.10: (a) Illustration of periodical daisy-chained Helmholtz resonators. (b) The calculated effective bulk modulus in the above one-dimensional subwavelength Helmholtz resonators.

The second example, always for 1D AMMs, refers to the experiment carried out by Lee et al. [21]: acoustic metamaterial with negative modulus. The sample used is represented in Fig. 2.11(a) and it is composed by a unit cell: a short tube with a side hole (SH) of 10 mm diameter. Unlike the Helmholtz resonator, this unit cell does not resonate acoustically by itself. Connecting the unit cells, a tube (32.3 mm of inner diameter) with regular array of SHs is obtained spaced by 70

mm distance. The results in Fig. 2.11(b), show that the sound waves above 450 Hz propagated well, but sounds below 450 Hz were completely blocked by the metamaterial. So this AMM blocks the low frequencies.

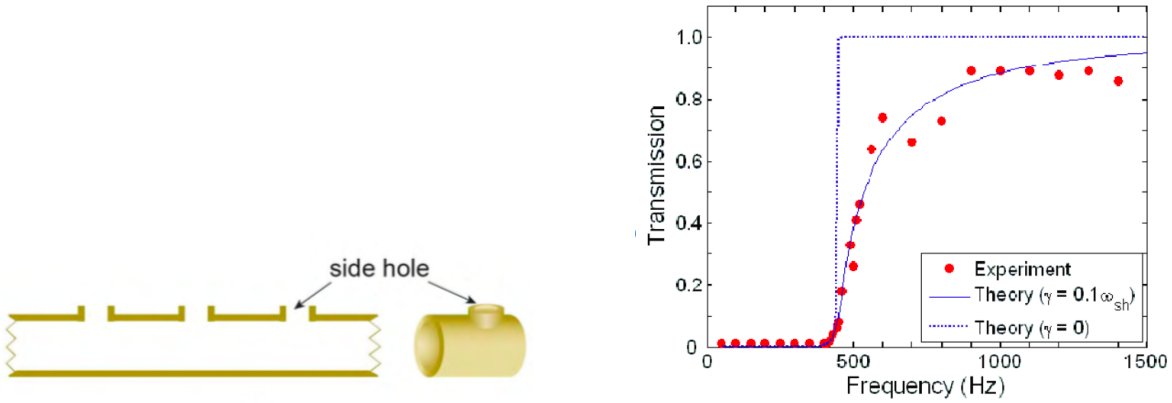

Figure 2.11: (a) Structure of the used sample of metamaterials. (b) Experimental and theoretical values of transmission in the metamaterial..

AMMs with double negative parameters

For this kind of AMMs the paper of Lee et al. [22] is reported: composite acoustic medium with simultaneously negative density and modulus. Three samples are created: the first with a negative density structure, the second with a negative modulus structure and the third with negative density and negative modulus structure. The samples are represented in Fig. 2.12(a). They are composed by a unit cell. The first structure presents an array of thin membranes, the second structure has lateral holes and the last consists of interspaced membranes and side holes. The length measures 70 mm and the inner diameter 32.3 mm. The membranes and the side

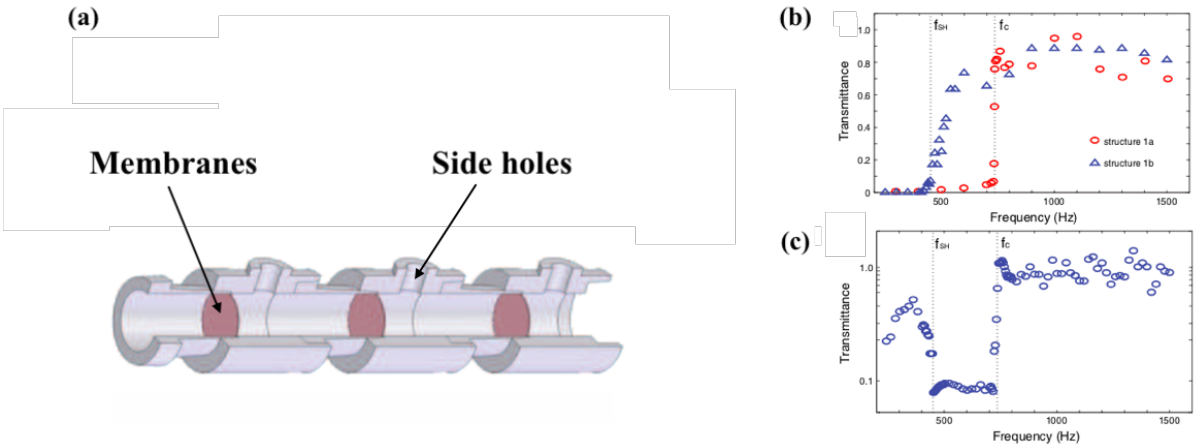

Figure 2.12: (a) The composite structure consisting of interspaced membranes and side holes (b) Transmission data for the first two AMMs. (c) Transmission data for the third AMM.

holes in the third structure are respectively identical to those of the first and second structure. Results are represented in Fig. 2.12(b) for the first and the second AMMs, in Fig. 2.12(c) for

the third AMM. Unlike the first two AMMs, the third, with negative density and modulus, has a non-transmission gap between 450 Hz and 735 Hz.

AMMs with inhomogeneous and anisotropic mass density

In the first example we focalize on gradient index (GRIN) sonic lenses based on two-dimensional sonic crystals (SC), studied by Climente et al. [23]: sound focusing by gradient index sonic lenses. A 2D sonic crystal is a periodic distribution of solid cylinders in air with their axis parallel aligned. It presents a frequency gap where the sound propagation is forbidden because of Bragg reflection. The GRIN lens and the region of data acquisition ($24 \times 24\ cm^2$) are shown in Fig. 2.13(a). The results are displayed, in terms of amplification maps, in Fig. 2.13(c) and 2.13(b) at a frequency of 4.5 kHz. It is possible to note the focusing effects: focal spot and diffraction lobes.

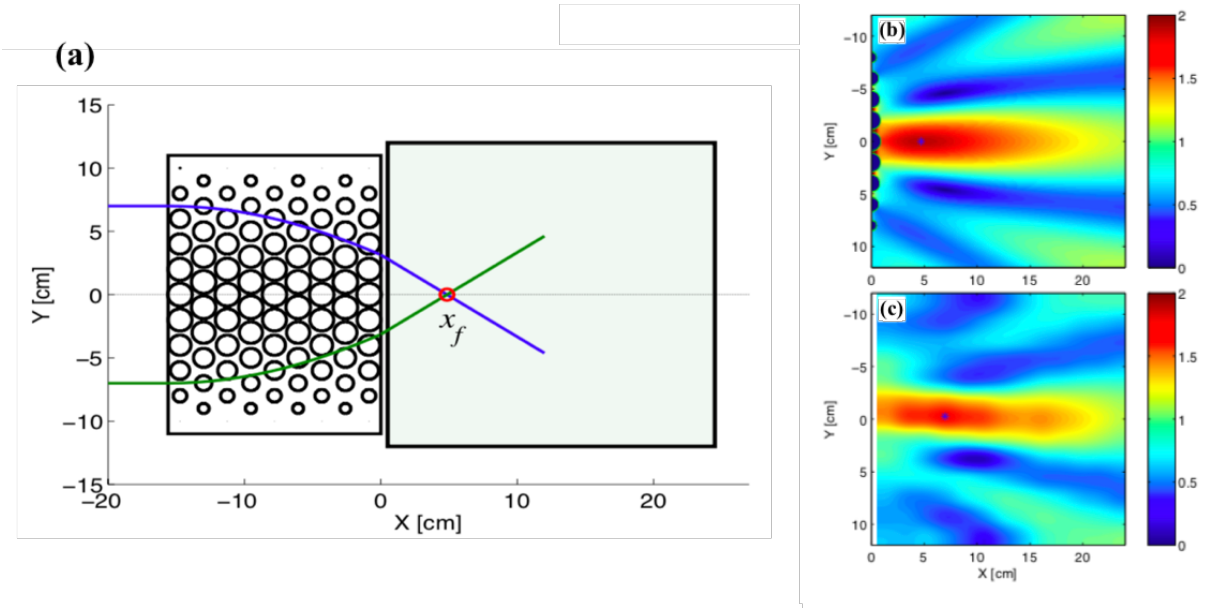

Figure 2.13: (a) Schematic view of a GRIN lens made of nine columns of metal rods (circles). (b) Sound amplification map generated by 4.5 kHz sound waves impinging a 9 layers thick 2D GRIN SC lens. (c) The corresponding map obtained by using a multiple scattering algorithm.

From the same authors Climente et al. we present "the design, construction, and experimental characterization of the acoustic analogue of the so called photonic black-hole" [24]. In Fig. 2.14 is represented the structure of the sample. It is composed by cylinders made of a plastic material, which could be considered acoustically rigid in the air medium due to the high impedance mismatch between these two media. There are two regions placed in an hexagonal lattice of lattice constant $a = 7.5$ mm:

- a core region with radius of 80 mm containing cylinders with constant diameter of 7.2 mm, the air is forced to pass through the narrow channels left between cylinders due to the high filling fraction of hexagonal lattice (84%);
- the surrounding shell has an external radius of 120 mm and it is separated from the core by the line of defects. The cylinders diameter decreases increasing the distance from the centre. It is designed as a SC GRIN lens.

In Fig. 2.14(a) the sample is represented with the trajectory of rays inside the sample itself. In Fig. 2.14(b) the results for the core and the whole black-hole sample are shown in terms of absorption coefficient. For almost any frequency, the core's absorption is strongly enhanced by the complete structure (core and shell), which demonstrates the functionality of the shell.

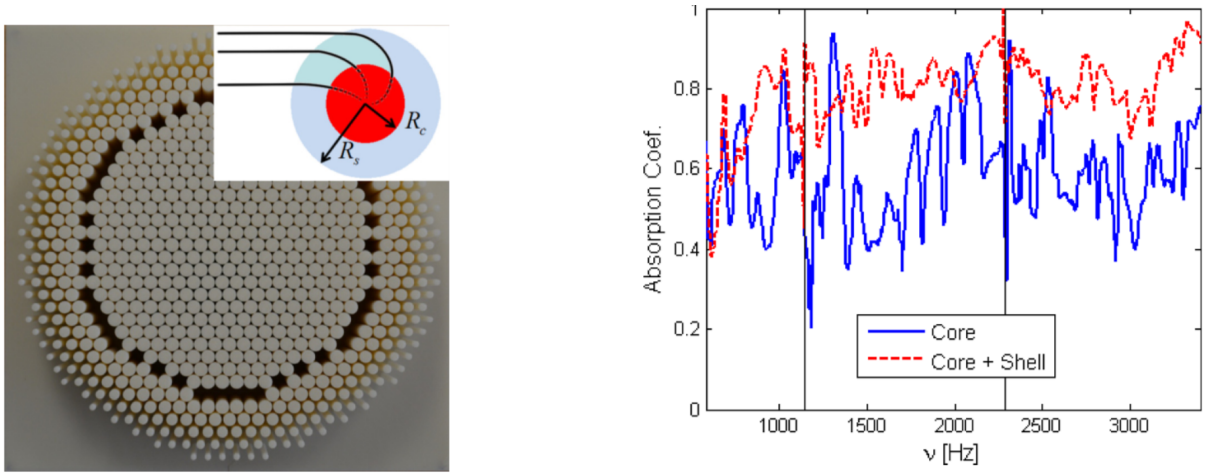

(a) **(b)**

Figure 2.14: (a) Photograph of the structure with acoustic rays trajectory. (b) Absorption coefficients due to the core of the black-hole sample (blue line) and by the complete black-hole (red line).

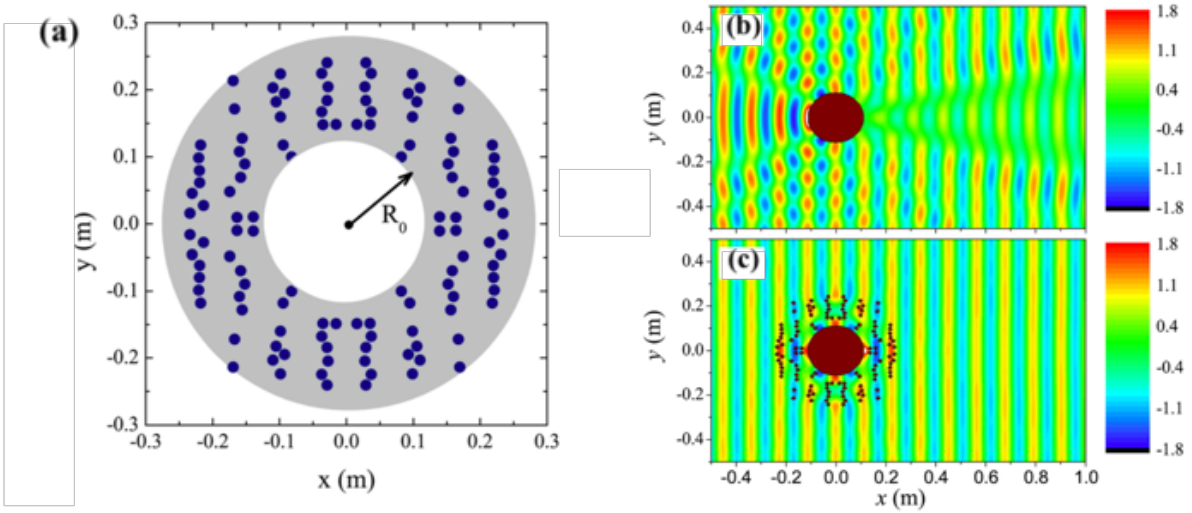

Figure 2.15: (a) The proposed distribution of the cylinders designed to cloak a rigid body displaced at the center. Total pressure maps (real part) at 3 kHz (b) for a rigid cylindric and (c) for the acoustic cloak.

In the end, the work of Garcìa-Chocano et al. is reported [25]: acoustic cloak for airborne sound by inverse design. This device makes an object invisible, in acoustic terms. The cloak, Fig. 2.15(a) consists of 120 aluminum cylinders of 15 mm diameter surrounding the cloaked object, a cylinder with a diameter of 22.5 cm. At the frequency of 3 kHz the results for a normal, with

strong scattering and shadowing, and for a cloaked cylinder, in which the cylinder inside the cloak results acoustically invisible, are respectively shown in Fig. 2.15(b) and 2.15(c). Therefore the interferences, produced by the cylinder, are completely restored by the acoustic cloak.

Mechanical AMMs

The only example presented is made by Stenger et al. [26]: experiments on elastic cloaking in thin plates. The authors design, fabricate, and characterize a cloaking structure for elastic waves in 1 mm thin structured polymer plates, consisting of 20 concentric rings of 16 different metamaterials, each being a tailored composite of polyvinyl chloride and polydimethylsiloxane. The cloak photograph is shown in Fig. 2.16(a). The cloaking results almost perfect at 200 Hz, increasing imperfections with higher frequencies. The results for different frequencies (200, 300, 400 and 450 Hz) are reported in Fig. 2.16(b) without and with cloak.

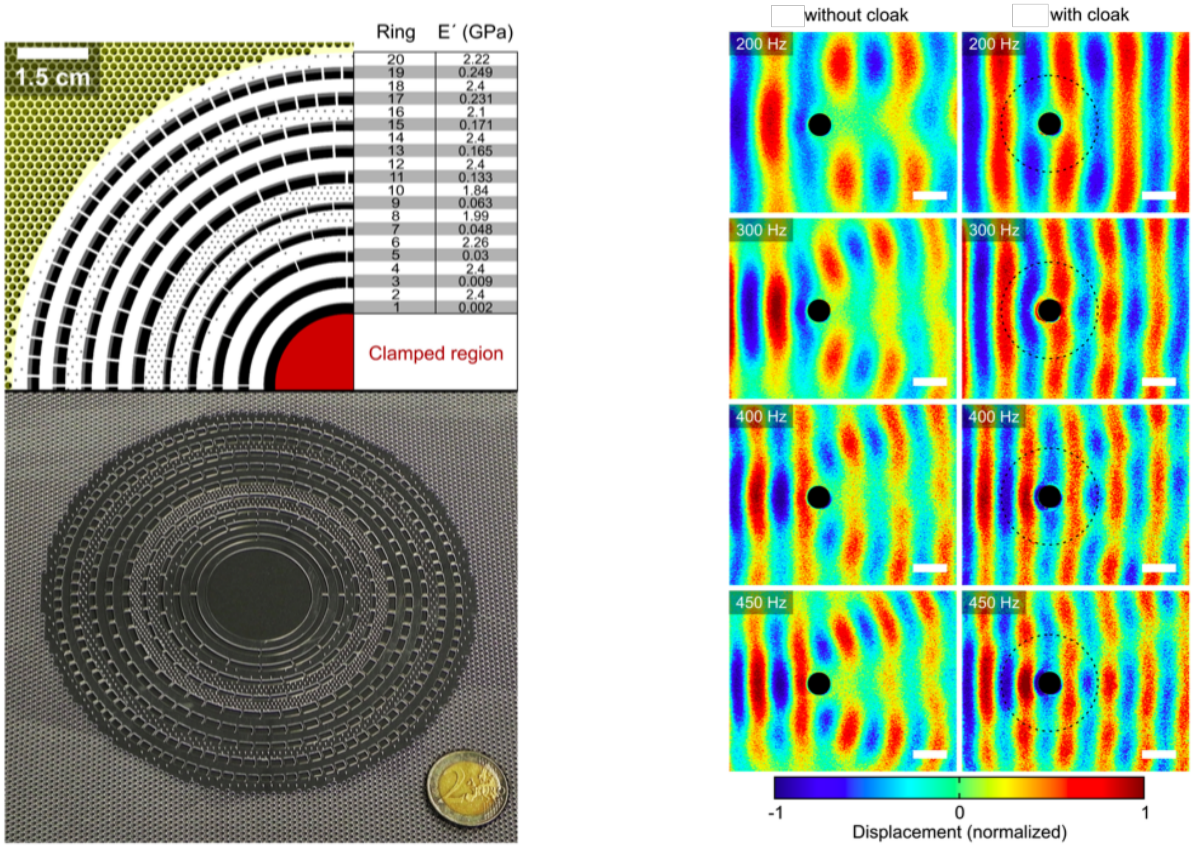

(a) **(b)**

Figure 2.16: (a) Photograph of the cloak structure. (b) Experimental results for 200, 300, 400, and 450 Hz without and with cloak.

AMMs with homogenized properties

We present the AMM used in this work and studied by D'Amico in [27]: melamine foam with aluminium cylindrical inclusions. The sample consists in melamine foam plate, pierced and with aluminium inclusions and a composite material skin. The volume fraction of the inclusions is

changed from 0.0045 to 0.03 with a step of 0.0015. The aim are to evaluate the transmission loss due to this AMM in the range of low frequencies and to obtain homogenized properties (as Young and shear modulus and Poisson's ratio) for further works through numerical simulation with MSC Actran. The AMM model is shown in Fig. 2.17. The results show an increase in sound transmission loss for 0.015 volume fraction, coherently with the mass-law, Fig. 2.18.

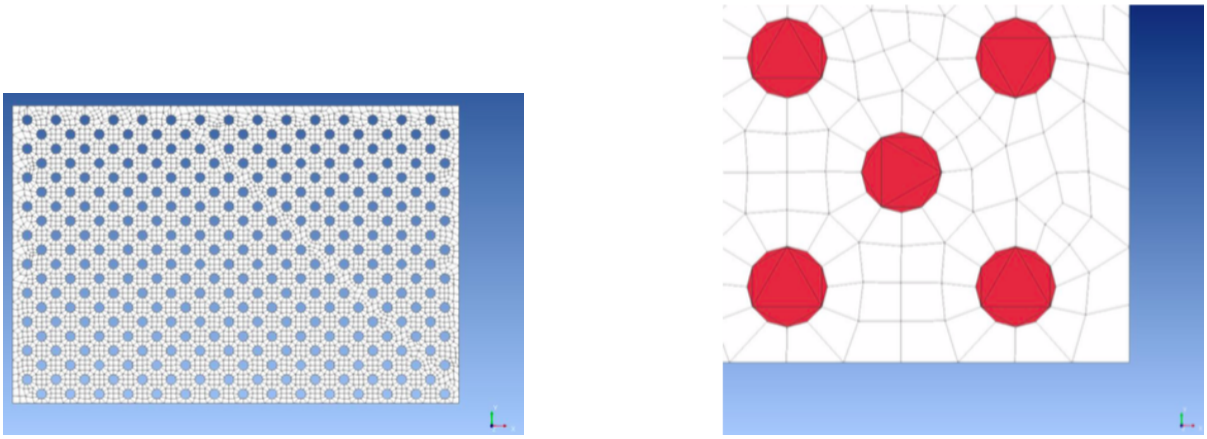

(a) **(b)**

Figure 2.17: AMM in Actran. (a) Perforated plate meshed. (b) Particular of meshed holes.

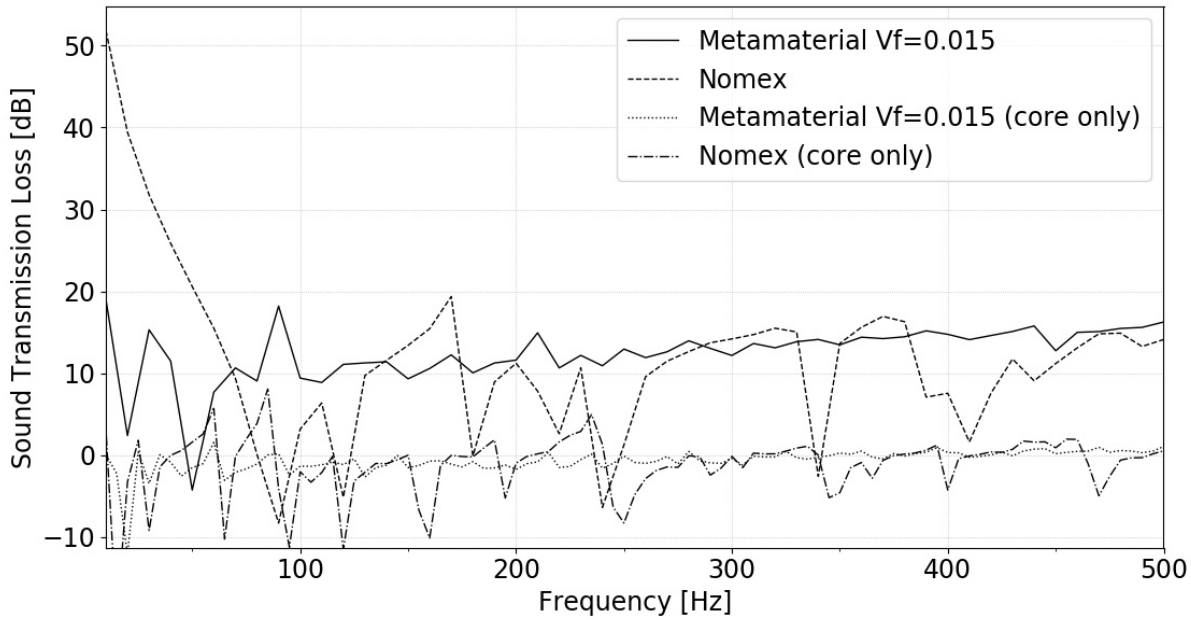

Figure 2.18: Sound transmission loss of metamaterial plate with 0.0150 inclusions volume fraction and composite material skin, compared with core only and Nomex plates.

2.3 Windowless concept

The windowless concept consists in a passengers aircraft's fuselage without windows, in which windows are replaced by monitors connected to external cameras (model of false windows with

monitor in Fig 2.19). The windowless concept has been studied in literature through three different configurations:

- windowless cockpit as described in [28, 29];
- windowless fuselage used on blended wing body aircraft in [30, 31];;
- windowless fuselage in traditional passengers aircrafts, [32, 33, 34].

The first case consists in removing the windscreens: besides the weight reduction, there is a better pressure distributions on the noise of the aircraft. The windscreens are replaced with monitors and cameras to guarantee a 360° view. On a blended wing body aircraft it is impossible, because of the particular shape of the wing-fuselage structure, to have windows and exits. Therefore solutions, to limit the passengers discomfort deriving from a windowless cabin in future commercial blended wing body aircraft, should be considered. In a traditional fuselage exploiting a windowless design, all windows, except those of emergency exits, are removed and replaced with a visual system, composed by internal monitors and external cameras.

Particularly this last configuration could be applied to a traditional short-medium aircraft. The main objective of this concept is to achieve a lighter aircraft, because removing windows lead to a reduction of weight (windows are holes in the structure and they need reinforcements). As a matter of fact a lighter aircraft consumes less fuel and produces less emissions. Another possible advantage is the reduction of noise in the passengers cabin and it will be investigated in this work. Furthermore windows represents holes in the structure also in acoustic terms, the acoustic impedance[1] of windows materials (plexiglass 3.10 MRayl and lexan 2.71 MRayl) is lower than fuselage material (for example aluminum 17.10 MRayl)[2].

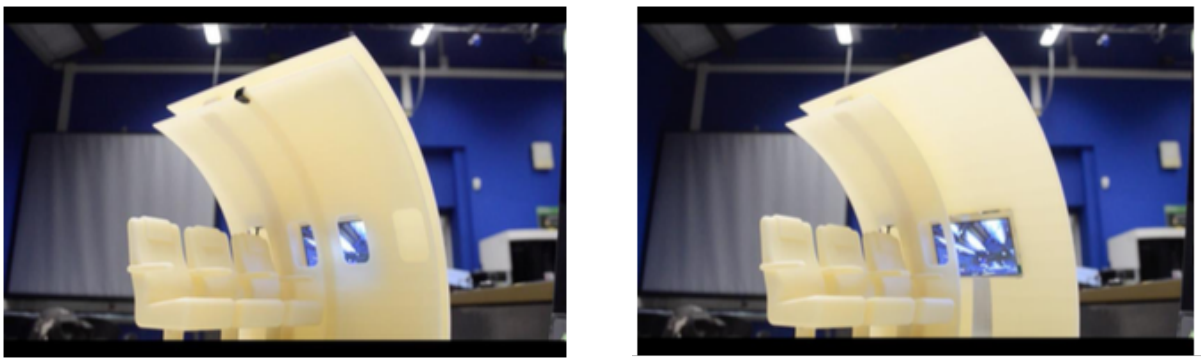

(a) **(b)**

Figure 2.19: Small scale model of false windows.

[1] Acoustic impedance of a medium is defined as $Z_0 = \rho_0 \cdot c_0$ with ρ_0 and c_0 the density and speed of sound in the unperturbed medium. The unit of measurement is Rayleigh or Rayl with 1 Rayl $= 1\ \frac{\text{kg}}{\text{s}\cdot\text{m}^2}$, [35].

[2] Impedance values are extracted form http://www.ondacorp.com/images/LaustPedersen_090405.zip on the 17th of March 2019.

2.4 The vibroacoustic problem

2.4.1 Governing equations

The following sections about the vibroacoustic problem are written referring to [36] and [37].

To resolve the vibroacoustic problem in this work the following hypothesis are assumed:

- the fluid-structure system has a linear behavior;
- small deformation for the structure (continuum body);
- the fluid, in contact with the structure, is homogeneous, inviscid and irrotational compressible;
- gravitational effects are neglected and generally body forces.

The structure in Fig. 2.20 is considered and it occupies the domain Ω_s with unit normal external n_i^s. On this structure the Dirichlet boundary conditions Γ_D^s and Neumann boundary conditions Γ_N^s are applied; these conditions lead to the displacement $\bar{s}_i$ and to the surface force f_i respectively. The fluid cavity occupies the domain Ω_f with unit normal external n_i^f and the fluid-structure interface surface is defined as Γ_{fs}. On the fluid cavity edge, the boundary condition Γ_N^f defines rigid walled bounds, on which the zero normal pressure gradient boundary condition is imposed. The density of the structure is ρ_s while the constant reference density and the constant speed of sound of the fluid are ρ_f and c_f respectively. The linearized deformation tensor is denoted by ε_{ij} and the corresponding stress tensor by σ_{ij}.

Under the previous hypothesis, the structure is described by the following system of the differential equations:

$$\begin{cases} \sigma_{ij,j} = \rho_s \ddot{s}_i & \text{in } \Omega_s \\ \sigma_{ij} n_j^s = f_i & \text{in } \Gamma_N^s \\ s_i = \bar{s}_i & \text{in } \Gamma_D^s \\ \sigma_{ij} n_j^s = p\, n_i^f & \text{in } \Gamma_{fs}\ . \end{cases} \tag{2.2}$$

In this system the last equation expresses the coupling between the structure and fluid field. The zero Neumann boundary condition is implied on the structure free surface.

The acoustic field inside the fluid cavity, in absence of acoustic sources, is described by the wave equation and boundary conditions, obtained by the linearization of the Euler equations system:

$$\begin{cases} p_{,ii} = \frac{1}{c_f^2} \ddot{p} & \text{in } \Omega_f \\ p_{,i} n_i^f = -\rho_f \ddot{s}_i n_i^f & \text{in } \Gamma_{fs} \\ p_{,i} n_i^f = 0 & \text{in } \Gamma_D^f \end{cases} \tag{2.3}$$

where the fluid-structure coupling term in the second equation relates the normal pressure gradient with the motion of the structure. This system of equations could also be written using the velocity field v_i instead of the pressure. The velocity field v_i satisfies the irrotationality conditions, so the equations could be expressed in terms of scalar potential ϕ.

The stress tensor σ_{ij} could be expressed as linearly proportional to the linearized strain tensor ε_{ij}:

$$\sigma_{ij} = c_{ijkl} \varepsilon_{kl} \tag{2.4}$$

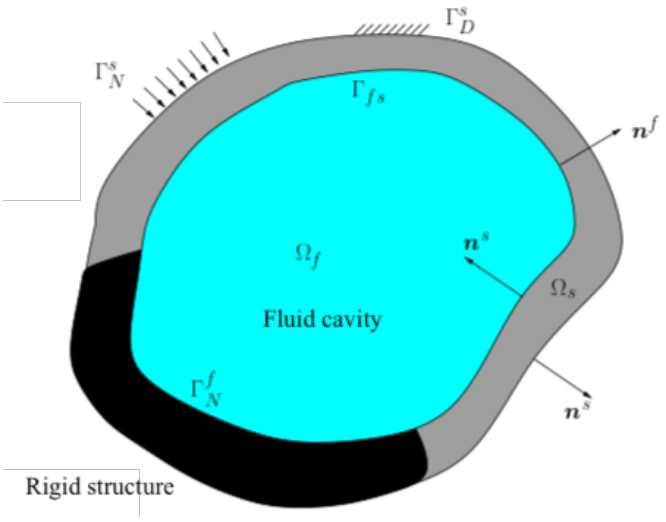

Figure 2.20: Coupled system domain.

where c_{ijkl} denotes elastic material constants. Moreover there is the following differential relation between the linearized strain tensor ε_{kl} and the displacement s_k:

$$\varepsilon_{ij} = \frac{1}{2}\left(s_{k,l} + s_{l,k}\right) \ . \tag{2.5}$$

Finally the tensor σ_{ij} is a function of the derivatives of the field variable, the displacement s_i. The elastic tensor c_{ijkl} is defined as:

$$c_{ijkl} = a_{ijkl} - b_{ijkl}\dot{s}_i \tag{2.6}$$

where the tensor a_{ijkl} is the elastic coefficients of the structure and the tensor b_{ijkl} is the damping coefficients of the structure. Therefore the costitutive equation become:

$$\sigma_{ij} = \left(a_{ijkl} - b_{ijkl}\dot{s}_i\right)\varepsilon_{kl} \ . \tag{2.7}$$

2.4.2 Variational formulation

The previous *strong* formulation is expressed in terms of structural displacement s_i and fluid pressure p. In order to obtain the variational formulation associated with the local equations 2.2 and 2.3, the test function method is applied. The *weak* formulation, for the two systems, introduces arbitrary weighting functions, which represents the principal field variables that describe the evolution of the system. This *weak* formulation is equivalent to the Principle of Virtual Displacement (PVD) applied on the same system.

Starting from the structural system 2.2, we integrate over Ω_s and multiply the dynamic equilibrium of the system by arbitrary time-indipendent test-function (or virtual displacement) δ_{si}, then we integrate by parts and apply Green's formula. Finally we obtain:

$$\int_{\Omega_s} \delta\varepsilon_{ij}\sigma_{ij}dV + \int_{\Omega_s} \delta s_i \rho_s \ddot{s}_i dV = \int_{\partial\Omega_s} \delta s_i \sigma_{ij} n_j^s ds \tag{2.8}$$

where

$$\delta\varepsilon_{ij} = \frac{1}{2}\left(\delta s_{k,l} + \delta s_{l,k}\right) \tag{2.9}$$

We decompose the surface integral, on the second term of the equation, over the boundaries Γ_N^s and Γ_{fs} and we obtain:

$$\int_{\Omega_s} \delta\varepsilon_{ij}\sigma_{ij}dV + \int_{\Omega_s} \delta s_i \rho_s \ddot{s}_i dV = \int_{\Gamma_N^s} \delta s_i f_i ds + \int_{\Gamma_{fs}} \delta s_i p\, n_i ds \tag{2.10}$$

where $n_i = n_i^f$. The equation represents the PVD for mechanical variables, including the acoustic coupling term. Moreover this *weak* formulation satisfies the *natural* boundary condition (Neumann type). The virtual displacement δs_i must be chosen according to the *essential* condition (Dirichlet type).

The acoustic system 2.3, multiplying the wave equation by δp, integrating by parts, applying Green's formula and using the Neumann boundary condition on the fluid-structure interface surface, could be written as:

$$\int_{\Omega_f} \delta p_{,i} p_{,i} dV + \int_{\Omega_f} \frac{1}{c_f^2}\delta p \ddot{p} dV = -\int_{\Gamma_{fs}} \delta p\, \rho_f \ddot{s}_i n_i ds\ . \tag{2.11}$$

This equation satisfies the zero normal pressure gradient condition along the rigid wall.

In the equations 2.10 and 2.11 the terms on the right represent the fluid-structure coupling. In order to obtain the final variational formulation of the previous equations, we take in account the constitutive structural relation 2.7:

$$\begin{cases} \displaystyle\int_{\Omega_s} \delta\varepsilon_{ij} a_{ijkl}\varepsilon_{kl} dV - \int_{\Omega_s} \delta\varepsilon_{ij} b_{ijkl}\dot{s}_i\varepsilon_{kl} dV = -\int_{\Omega_s} \delta s_i \rho_s \ddot{s}_i dV + \int_{\Gamma_N^s} \delta s_i f_i ds + \int_{\Gamma_{fs}} \delta s_i p\, n_i ds \\ \displaystyle\int_{\Omega_f} \delta p_{,i} p_{,i} dV + \int_{\Omega_f} \frac{1}{c_f^2}\delta p\, \ddot{p} dV = -\int_{\Gamma_{fs}} \delta p\, \rho_f \ddot{s}_i n_i ds\ . \end{cases} \tag{2.12}$$

where s_i and p are the field variables.

2.4.3 Numerical approximation

The primary variables s_i and p must be approximate to obtain a numerical solution of the system 2.12. Therefore the vectorial unknowns of the discretized problem, denoted $\boldsymbol{U}$ and $\boldsymbol{P}$, are introduced:

$$\begin{aligned} s_i &= \boldsymbol{N}_i^s \boldsymbol{U} \\ p &= \boldsymbol{N^p P} \end{aligned} \tag{2.13}$$

where $\boldsymbol{N}_i^s$ and $\boldsymbol{N}_p$ are generic row matrices functions of the space coordinates x_i, which interpolate the continuous unknown variables. In a finite elements discretization, $\boldsymbol{U}$ and $\boldsymbol{P}$ are the nodal displacements and pressure respectively. These two unknowns are only function of time t. Substituting the equations 2.13 in the system 2.12, leads to the following submatrices:

$$\int_{\Omega_s} \delta\varepsilon_{ij} a_{ijkl}\varepsilon_{kl} dV = \delta\boldsymbol{U}^T \boldsymbol{K}_{ss} \boldsymbol{U} \tag{2.14}$$

$$\int_{\Omega_s} \delta\varepsilon_{ij} b_{ijkl} \dot{s}_i \varepsilon_{kl} dV = \delta \boldsymbol{U}^T D_{ss} \dot{\boldsymbol{U}} \tag{2.15}$$

$$\int_{\Omega_s} \delta s_i \rho_s \ddot{s}_i dV = \delta \boldsymbol{U}^T \boldsymbol{M}_{ss} \ddot{\boldsymbol{U}} \tag{2.16}$$

$$\int_{\Gamma_N^s} \delta s_i f_i ds = \delta \boldsymbol{U}^T \boldsymbol{F}_s \tag{2.17}$$

$$\int_{\Gamma_{fs}} \delta s_i p \, n_i ds = \delta \boldsymbol{U}^T \boldsymbol{S}_{sp} \boldsymbol{P} \tag{2.18}$$

$$\int_{\Omega_f} \delta p_{,i} p_{,i} dV = \delta \boldsymbol{P}^T \boldsymbol{H} \boldsymbol{P} \tag{2.19}$$

$$\frac{1}{c_f^2} \int_{\Omega_f} \delta p \ddot{p} dV = \delta \boldsymbol{P}^T \boldsymbol{Q} \ddot{\boldsymbol{P}} \tag{2.20}$$

$$\rho_f \int_{\Gamma_{fs}} \delta p \ddot{s}_i n_i ds = \delta \boldsymbol{U}^T \rho_f \boldsymbol{S}_{sp}^T \ddot{\boldsymbol{P}} \tag{2.21}$$

in which $\boldsymbol{M}_{ss}$, $\boldsymbol{K}_{ss}$ and $\boldsymbol{D}_{ss}$ are the mass, stiffness and the damping matrices of the structure; $\boldsymbol{Q}$ and $\boldsymbol{H}$ are the mass and stiffness matrices of the fluid; $\boldsymbol{S}_{sp}$ is the fluid structure coupling matrix; $\boldsymbol{F}_s$ is the applied mechanical force vector. Finally the system 2.12 could be written in matrix form as:

$$\begin{bmatrix} \boldsymbol{M}_{ss} & 0 \\ -\rho_f \boldsymbol{S}_{sp}^T & \boldsymbol{Q} \end{bmatrix} \cdot \begin{Bmatrix} \ddot{\boldsymbol{U}} \\ \ddot{\boldsymbol{P}} \end{Bmatrix} + \begin{bmatrix} \boldsymbol{D}_{ss} & 0 \\ 0 & 0 \end{bmatrix} \cdot \begin{Bmatrix} \dot{\boldsymbol{U}} \\ \dot{\boldsymbol{P}} \end{Bmatrix} + \begin{bmatrix} \boldsymbol{K}_{ss} & \boldsymbol{S}_{sp} \\ 0 & \boldsymbol{H} \end{bmatrix} \cdot \begin{Bmatrix} \boldsymbol{U} \\ \boldsymbol{P} \end{Bmatrix} = \begin{Bmatrix} \boldsymbol{F}_s \\ 0 \end{Bmatrix} \tag{2.22}$$

on which the initial conditions and the *essential* boundary conditions must be defined. The equation 2.22 is the classical discrete form of the fluid structure interaction problem, also known in literature as (u, p) formulation. The second term of the equation represents the damping, under the previous hypothesis there is not damping due to fluid. If the fluid were viscous, there would be a damping term depending on viscosity.

2.4.4 Frequency domain

The frequency f could be written as a function of pulsation ω, as $f = 2\pi\omega$. The Fourier transform is introduced for the displacements s_i:

$$s_i(x_i, \omega) = \int_{-\infty}^{\infty} s_i(x_i, t) \, e^{-i\omega t} dt \tag{2.23}$$

and for pressure p:

$$p(x_i, \omega) = \int_{-\infty}^{\infty} p(x_i, t) \, e^{-i\omega t} dt \tag{2.24}$$

and substituting these equations in the first equation of the structural system 2.2, after some manipulations, we obtain:

$$-\omega^2 \rho_s s_i - \sigma_{ij,i} = 0 \quad in \ \Omega_s \tag{2.25}$$

and for the wave equation 2.3 we obtain the Helmholtz equation:

$$p_{,ii} = -\frac{\omega^2}{c_f^2} p \tag{2.26}$$

where s_i and p are now function of space x_i and pulsation ω and so frequency f.

The symmetric stress sensor could expressed as:

$$\sigma_{ij}(\omega) = \left[a_{ijkl}(\omega) + i\omega b_{ijkl}(\omega) s_i\right] \varepsilon_{kl} \ . \tag{2.27}$$

where

$$\lim_{|\omega| \to +\infty} a_{ijkl}(\omega) = a_{ijkl}(+\infty) \tag{2.28}$$

$$\lim_{|\omega| \to +\infty} \omega \, b_{ijkl}(\omega) = 0 \tag{2.29}$$

so

$$\sigma_{ij}(+\infty) = a_{ijkl}(+\infty) \varepsilon_{kl}(+\infty) \tag{2.30}$$

with $a_{ijkl}(+\infty)$ the initial elasticity tensor, so, for high frequencies, the structure behavior changes from viscolelstic to elastic. The elasticity coefficients are defined by the initial elasticity tensor $a_{ijkl}(+\infty)$. This tensor differs from the equilibrium modulus tensor $a_{ijkl}(0)$, that is defined at $\omega = 0$:

$$\sigma_{ij}(0) = a_{ijkl}(0) \, \varepsilon_{kl}(0) \tag{2.31}$$

for a static deformation process. The tensor $a_{ijkl}(\omega)$ and $b_{ijkl}(\omega)$ are even functions, symmetric and positive-definiteness.

Boundary conditions are the same of systems 2.2 and 2.3, but now they depend on ω.

Finally, using the boundary conditions, applying the variational formulation and defining the complex vectors $\boldsymbol{U}(\omega)$ and $\boldsymbol{P}(\omega)$ of nodal values of $s_i(\omega)$ and $p(\omega)$ respectively, we obtain the complex matrix equation of the computational model:

$$\begin{bmatrix} -\omega^2 \boldsymbol{M}_{ss} + i\,\omega \boldsymbol{D}_{ss} + \boldsymbol{K}_{ss} & \boldsymbol{S}_{sp} \\ -\rho_f \omega^2 \boldsymbol{S}_{sp}^T & -\omega^2 \boldsymbol{Q} + \boldsymbol{H} \end{bmatrix} \cdot \begin{Bmatrix} \boldsymbol{U} \\ \boldsymbol{P} \end{Bmatrix} = \begin{Bmatrix} \boldsymbol{F}_s \\ 0 \end{Bmatrix} \tag{2.32}$$

where the unknown vectors $\boldsymbol{U}$ and $\boldsymbol{P}$, and the structural, acoustic, coupling matrices and the force vector, depend on frequency ω (or f).

Chapter 3

MSC Actran

3.1 Actran's modules

Actran (acoustic transmission) is finite elements-based software developed by the Free Field Technologies, MSC Software Company, for acoustic, vibroacoustic and aeroacoustic analysis. Actran provides a rich library of material models, a complete elements library and high performance solvers [38]. The used version is Actran 17.1.

Actran is composed by the following modules:

- Actran Acoustics, it is the basic module and it is a prerequisite fo advanced modules;
- Actran VibroAcoustics, it is used to study interaction between fluid and structure;
- Actran AeroAcoustic, it is used to predict the noise generated by complex flows, as turbulence flows;
- Actran SNGR, it predicts noise generated by turbulent flow by steady CFD solution;
- Actran TM, it is used to study noise generation in turbomachinery;
- Actran for Trimmed Body, it serves to combining Actran and MSC Nastran for advanced vibroacoustic analysis;
- Actran DGM, it is used to solve the linearized Euler equations using discontinuous finite elements in complex physical condition;
- Actran VI, it is the graphical user interface specifically designed for pre-processing and post-processing for all Actran modules.

In the following section 3.2 a general description of Actran's major elements and how they work is reported (for the specific component description see chapter 4). Furthermore we refer to vibroacoustic analysis in Actran VI interface. References are taken from Actran 17.1 user's guide [39, 40], Actran VI user's guide [41] and from Actran tutorials and presentations where specifically reported.

3.2 Actran VI

3.2.1 Main sections

Actran VI could be used for pre-processing (creation of models and definition of their features) and for post-processing (visualization and comparison of results)[1].

This module is composed by five main sections:

- data tree panel, it contains the major information about the model and the analysis. The data tree panel is divided in five or more sections: topologies tree, material tree, table tree, analysis tree, visual tree and other optional trees, that could be activated. In Fig. 3.1 on the left there is the data tree panel, and on the right of the figure three viewports (the model and two visualizations of the results) are displayed. The data tree panel is described in the following section 3.2.2;
- render window, that allows to visualize model and results;
- toolbox, that allows to import, create, modify meshes and get information about, to import and visualize results and to launch Actran analysis (functions to create a mesh are described in section 3.2.3) ;
- selection tool, that allows to select and filter elements;
- menu, it is divided in file, view, add, utilities, window, wizards and help.

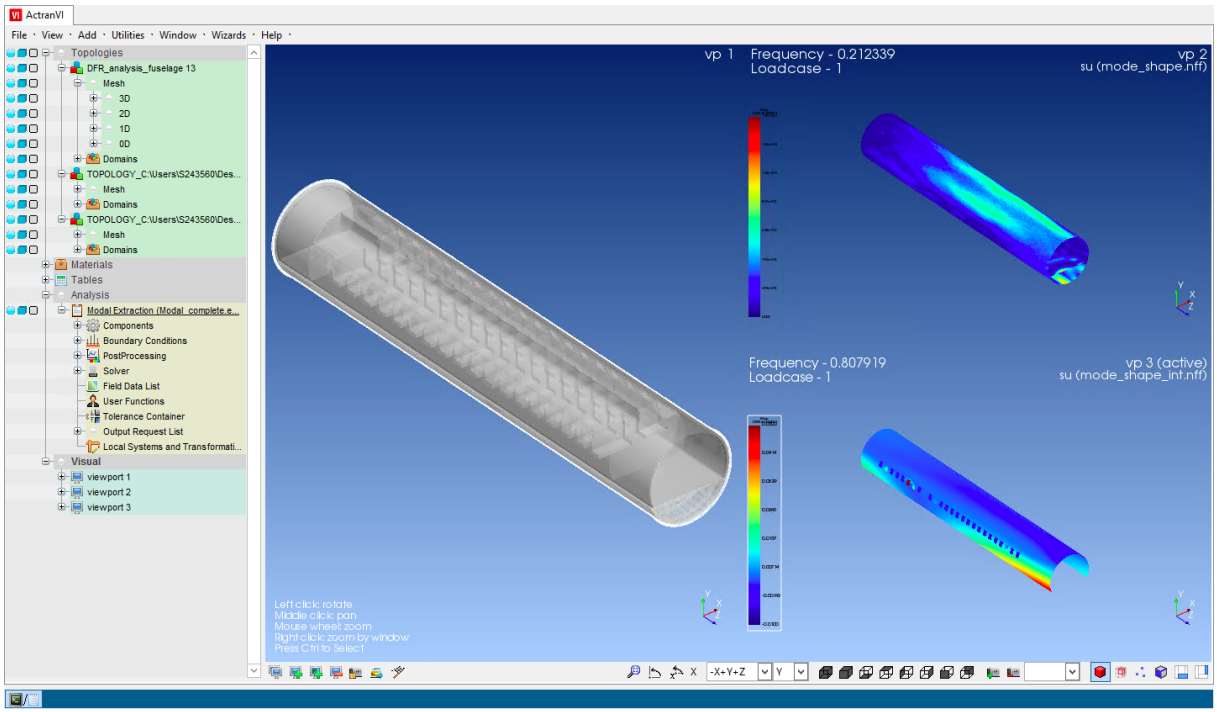

Figure 3.1: The data tree panel and the render window.

[1] https://www.mscsoftware.com/en-uk/product/actran-vi extracted on the 17th of March 2019.

3.2.2 Data tree panel

Topologies tree

The topologies tree contains all topologies created and imported in Actran VI. It gives information about the finite elements meshes and about the domains. Inside of each topology, in mesh node, there are PIDs, each PID is grouped by dimension (0D, 1D, 2D or 3D), interpolation order (linear or quadratic) and PID number (alphabetical order). Domains contain one ore more PIDs.

Materials tree

The materials tree allow to create (or import) different types of valid materials in Actran. The material, associated to a component, defines the physical properties of that component. To correctly create a material it is necessary to define its properties, that change according to the type of chosen material. The possible types of material and their compatibility with various components are shown in Tab. 3.1.

Table 3.1: Component vs. material compatibility matrix.

Keyword	Var.	FLUID	PERFECT_GAS	WATER	SHEET	ISOTROPIC_SOLID	TRANSV_ISO_SOLID	ORTHOTROPIC_SOLID	COMPOSITE_SOLID	POROUS	ANISOTROPIC_POROUS	BEAM_INERTIA	SPRING	STRINGER	PERFORATION	ANISOTROPIC_PIEZO	ORTHOROMBIC_PIEZO	TETRAGONAL_PIEZO
ACOUSTIC	p or Φ	✓	✓	✓														
VISCOTHERMAL	p or Φ	✓																
MEMBRANE	u_n				✓													
SOLID	u					✓	✓	✓										
SHELL	u					✓	✓	✓	✓									
DSHELL	u,θ					✓	✓	✓	✓									
RIGID_PERFORATED_SHELL	p														✓			
PERFORATED_SHELL	p,u,θ														✓			
POROUS_UP	p or Φ,u									✓	✓							
PIEZO_UE	u, E															✓	✓	✓
RIGID_POROUS	p or Φ									✓	✓							
LUMPED_POROUS	p or Φ									✓								
DELANY_BAZLEY_POROUS	p or Φ									✓								
MIKI_POROUS	p or Φ									✓								
BEAM	u,θ											✓						
DISCRETE	u												✓					
STIFFENER	u													✓				
INFINITE_DOMAIN	p or Φ	✓	✓	✓														
MODAL_BASIS	p or Φ	✓	✓	✓														
RAYLEIGH_SURFACE	u_n	✓																
EMPTY	-																	

Tables tree

The tables tree allows to create or import tables to define frequency or time dependent quantities.

Analysis tree

The analysis tree contains all parameters for Actran analysis. The following analysis are available in Actran:

- direct frequency response, this analysis computes the response of an acoustic system to specific excitation in physical coordinates. The following system of equations must be solved for various pulsations $\omega = 2\pi f$ (f is the frequency)

$$\left(\boldsymbol{K} + i\omega\boldsymbol{C} - \omega^2\boldsymbol{M}\right) \cdot \boldsymbol{x}(\omega) = \boldsymbol{F}(\omega) \tag{3.1}$$

  in which $x(\omega)$ is an unknown vector. The solvers for this analysis are `SPARSE`, `CG_ILU`, `MUMPS`, `PARDISO`, `KRYLOV` (with `SPARSE`, `MUMPS` and `PARDISO` as internal solvers) and `STAGGERED_SOLVER`;

- time response, it allows to calculate the transient response of an acoustic or a vibroacoustic system to a specific temporal excitation. The following system of ordinary differential equations in $\boldsymbol{x}(t)$ is solved for a given time range

$$\boldsymbol{K} \cdot \ddot{\boldsymbol{x}}(\boldsymbol{t}) + \boldsymbol{C} \cdot \dot{\boldsymbol{x}}(\boldsymbol{t}) + \boldsymbol{M} \cdot \boldsymbol{x}(t) = \boldsymbol{F}(t)\ ; \tag{3.2}$$

- modal frequency response, this analysis computes the response of an acoustic system to specific excitation in modal coordinates. The following system is solved for various pulsations $\omega = 2\pi f$

$$\begin{pmatrix} \mathcal{Z}_{\mathcal{SS}} & \mathcal{Z}_{\mathcal{SF}} \\ \mathcal{Z}_{\mathcal{SF}}^T & \mathcal{Z}_{\mathcal{FF}} \end{pmatrix} \cdot \begin{pmatrix} \alpha_{\mathcal{S}}(\omega) \\ \alpha_{\mathcal{F}}(\omega) \end{pmatrix} = \begin{pmatrix} \boldsymbol{\Phi}_{\boldsymbol{S}}^T \cdot \mathcal{F}_{\mathcal{S}}(\omega) \\ \boldsymbol{\Phi}_{\boldsymbol{S}}^T \cdot \frac{\mathcal{F}_{\mathcal{S}}(\omega)}{\omega^2} \end{pmatrix} \tag{3.3}$$

  with

$$\mathcal{Z}_{\mathcal{SS}} = \boldsymbol{\Phi}_{\boldsymbol{S}}^T \cdot \left(\boldsymbol{K}_{\boldsymbol{S}} - \omega^2\boldsymbol{M}_{\boldsymbol{S}}\right) \cdot \boldsymbol{\Phi}_{\boldsymbol{S}} = \left(\delta_{ij}\left(\omega_{\mathcal{S},j}^2 - \omega^2\right)\right) \tag{3.4}$$

$$\mathcal{Z}_{\mathcal{FF}} = \frac{1}{\omega^2}\boldsymbol{\Phi}_{\boldsymbol{F}}^T \cdot \left(\boldsymbol{K}_{\boldsymbol{F}} - \omega^2\boldsymbol{M}_{\boldsymbol{S}}\right) \cdot \boldsymbol{\Phi}_{\boldsymbol{F}} = \frac{1}{\omega^2}\left(\delta_{ij}\left(\omega_{\mathcal{F},j}^2 - \omega^2\right)\right) \tag{3.5}$$

$$\mathcal{Z}_{\mathcal{SF}} = \boldsymbol{\Phi}_{\boldsymbol{S}}^T \cdot \boldsymbol{C}_{\boldsymbol{SF}} \cdot \boldsymbol{\Phi}_{\boldsymbol{F}} \tag{3.6}$$

  where the unknown vector, for every pulsation, is $\begin{pmatrix} \alpha_{\mathcal{S}}(\omega) \\ \alpha_{\mathcal{F}}(\omega) \end{pmatrix}$. The available solvers for this analysis are `STRONG`, `WEAK`, `ITERATIVE` and `REFERENCE`;

- Green analysis, it allows to compute the radiation of a vibrating system. First Actran computes the transfer matrix of the system. Then it integrates the transfer matrix of the system multiplied by the excitation field on the radiating surface to deduce the acoustic pressure at the microphones;

- pellicular analysis, it allows to compute the radiation of a vibrating system. First Actran creates a pellicular modal basis on the radiating surface. Then it computes the transfer

matrix of the system. Finally it projects the excitation in the pellicular modal basis;

- modal extraction, through this analysis the modes of a closed acoustic cavity or of an undamped structure are calculated. Actran must solve the following equation

$$\boldsymbol{K}\boldsymbol{p} = \omega^2 \boldsymbol{M}\boldsymbol{p} \tag{3.7}$$

with $\boldsymbol{K}$ the stiffness matrix and $\boldsymbol{M}$ the mass matrix. The possible linear solver are `SPARSE`, `MUMPS` and `PARDISO`;

- compressible flow analysis, it is used to compute an irrotational and compressible flow velocity field $\boldsymbol{v}_f$. Actran solves the following equation

$$\nabla \cdot \left(\frac{\rho}{\rho_0} \boldsymbol{v}_f \right) = 0 \tag{3.8}$$

using a velocity potential ϕ

$$\boldsymbol{v}_f = \nabla \phi \, . \tag{3.9}$$

The linear solvers are `SPARSE`, `MUMPS` and `PARDISO`.

Analysis are subdivided in eight parts: components, boundary conditions, loadcases, post-processing options, solvers, field data, user function and local systems and transformations.

Components characterize a domain, in terms of physical properties. Components are defined by the material, their own properties and the domains. The finite elements defined in a component modify the number of degrees of freedom of the system impedance matrix.

Boundary conditions define an excitation or a reference condition on the finite elements of one or more domains. They are characterized by numerical or logical properties.

Loadcases are a combination of boundary conditions, duct modes or acoustic sources to excite the model.

The post-processing options allow to define output requests, both in terms of visualization and parameters (related to a point, element, etc.). There are three kind of post-processing options:

- output FRF (frequency response functions), through this option is possible to define the output parameters for the `plt` file;
- output map, through this option is possible to define the output parameters for map results. An output map displays the computed quantities for a specific frequency through colour maps;
- field map, through this option is possible to define output parameters for field map results. A field map refers to an output colour maps on a post-processing mesh that is different from the Actran finite elements mesh.

The algebraic solver must be selected depending on the analysis. In chapter 4 the selected solver will be described.

Field are used to describe the variation of a quantity as a function of space. Fields could be imported, created or defined through a user function.

The user functions data block contains functions used for fields or sources.

The local axes and transformation can be used to define local systems and transformations.

Visual tree

The visual tree contains all the viewports. The camera of each viewport could be synchronized or reset.

3.2.3 Meshing tools

Actran VI allows to create, modify or import meshes. The meshing toolbox is shown in Fig. 3.2 and it is divided in the following box: creation, surface, volume and transform. Furthermore for most meshing tools it is possible to have an interactive preview, that is updated every time the meshing parameters change. The workflow for Actran VI meshing tools is reported in Fig. 3.3.

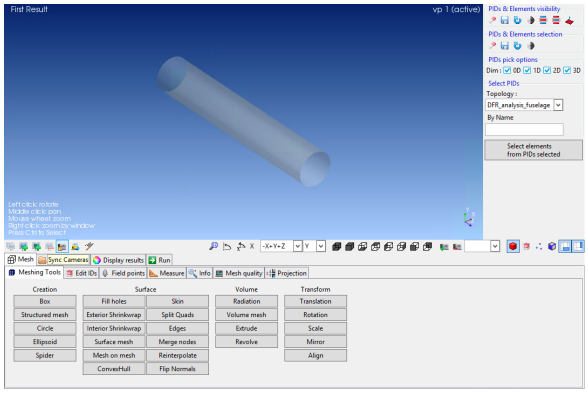

Figure 3.2: Actran VI meshing tools.

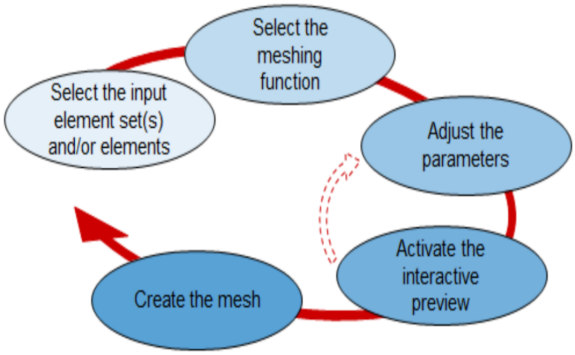

Figure 3.3: Typical workflow for Actran VI meshing tools.

The creation tools allow to create simple mesh as: box surface element set, containing quadrangles or triangles elements (box function); structured mesh (3D, 2D, 1D and 0D) defined by corner position, rotation angle and size parameters (structured mesh function); circle 1D or disk 2D (also arc and disk's sector) defined by centre position, rotation angle and element size parameter (circle function); ellipsoid or parts of its with triangles and/or quadrangles elements built starting from centre position, rotation angle and dimensions parameters, it is also possible to define baffle parameters (ellipsoid function). Furthermore in the field points toolbox the functions to create 0D elements are contained: cartesian, polar, costume, file (imported from an external file) and ISO3744. The 0D elements could also be created by selecting nodes on the render window or through the node ID.

The second box includes functions to create surfaces, starting from 1D, 2D or 3D element sets. The fill holes function allows to fill holes in a 2D (closed) or 3D mesh under a defined size and in different modes (fast, boundaries or costume). The exterior skinwrap function creates a 2D element set that wraps the input element sets; the size of shrink elements and the distance between the shrinkwrap surface and the input mesh must be defined. The interior skinwrap function is the opposite of the previous function, in fact it creates 2D element sets that wraps the interior of input 2D and 3D element sets; the size of shrink elements and the distance between

the shrinkwrap surface and the input mesh must be defined. The surface mesh function builds a 2D element set based on a set of edges of 1D elements or, if 2D elements are selected, the skin of this surface, the algorithm to create this mesh must be selected (fast, fitted or planar); moreover if there are more edges it is possible to activate the group by edge loop option. The mesh on mesh function re-meshes a 2D element set with new elements, that could be of a different size and type from the previous; the edges, that must be maintained, can be chosen within how the function re-meshes the free edge (hard or soft) and the inner interfaces (hard, soft or merge). The convexhull function envelopes with 2D elements the input element sets; baffle planes could be defined. The skin function creates the skin of an input element sets (3D, 2D or 1D). The split quad function splits all the quadrangle elements of an input mesh in triangle elements, the two mesh will have the same interpolation order. The edges function connects the edges of input mesh with bar elements, the connection mode must be chosen (direct, costume edge size or auto edge size); it is also possible to connect nodes by ID number. The merge nodes function makes the equivalence nodes of input PID domains if the distance between nodes is lower than the chosen distance parameter. The reinterpolate function modifies the interpolation of input element sets from linear to quadratic or viceversa. Finally the flip normal function reverses or regularizes the normals of 2D PIDs.

The volume tools allow to create from an input element sets 3D or 2D mesh. The volume mesh function creates a 3D mesh, with defined elements size, from one or more 2D meshes; hexahedral elements could be used. The extrude function builds a new 2D element sets from 1D input element sets and a new 3D element sets from 2D input element sets; the extrusion direction follows the chosen normal vectors, that could be computed using different methods (vertex normal, user defined normal, from centre). The revolve function creates a mesh revolving the input element set; the revolve total angle (angle parameter), the rotation axis (rotation axis origin and vector parameters) and the number of layer (steps parameter) must be defined. The radiation function is a combination of the four previous functions, it is used to automatically generate meshes for acoustic radiation problems.

The last box contains the transformation tools as: the translate function defined by vector and scale factor parameters; the rotation function around the coordinate X, Y and Z axis or around a user-defined axis (defined by the origin and rotation axis parameters) by a given angle; the scale function with a scale factor and a origin parameter; the mirror function that creates symmetrical mesh to a symmetry plane defined by three points; the align function that projects all nodes of the input element sets on a plane defined by three points.

An example is reported in Fig. 3.4: the meshing functions used to create the coupling surface of the pressure field around the fuselage from imported points (see section 4). The first step is to create a 0D element set from external nodes, Fig. 3.4(a). Then a circle is created from this 0D elements using twice (for closing the circle) the edges function, Fig. 3.4(b). In the third step the circle was extruded on the field length with a number of layer corresponding to the number of nodes in Z direction, the 2D mesh and a circle on the other edge of the fuselage are created, Fig. 3.4(c). Finally the merge nodes function is applied to eliminate duplicated nodes, Fig. 3.4(d).

3.2.4 Elements size criterion

In order to have a good level of accuracy with no flow condition, from 7 to 10 elements per wavelength for linear interpolation, and from 3 to 6 for quadratic element interpolation, are

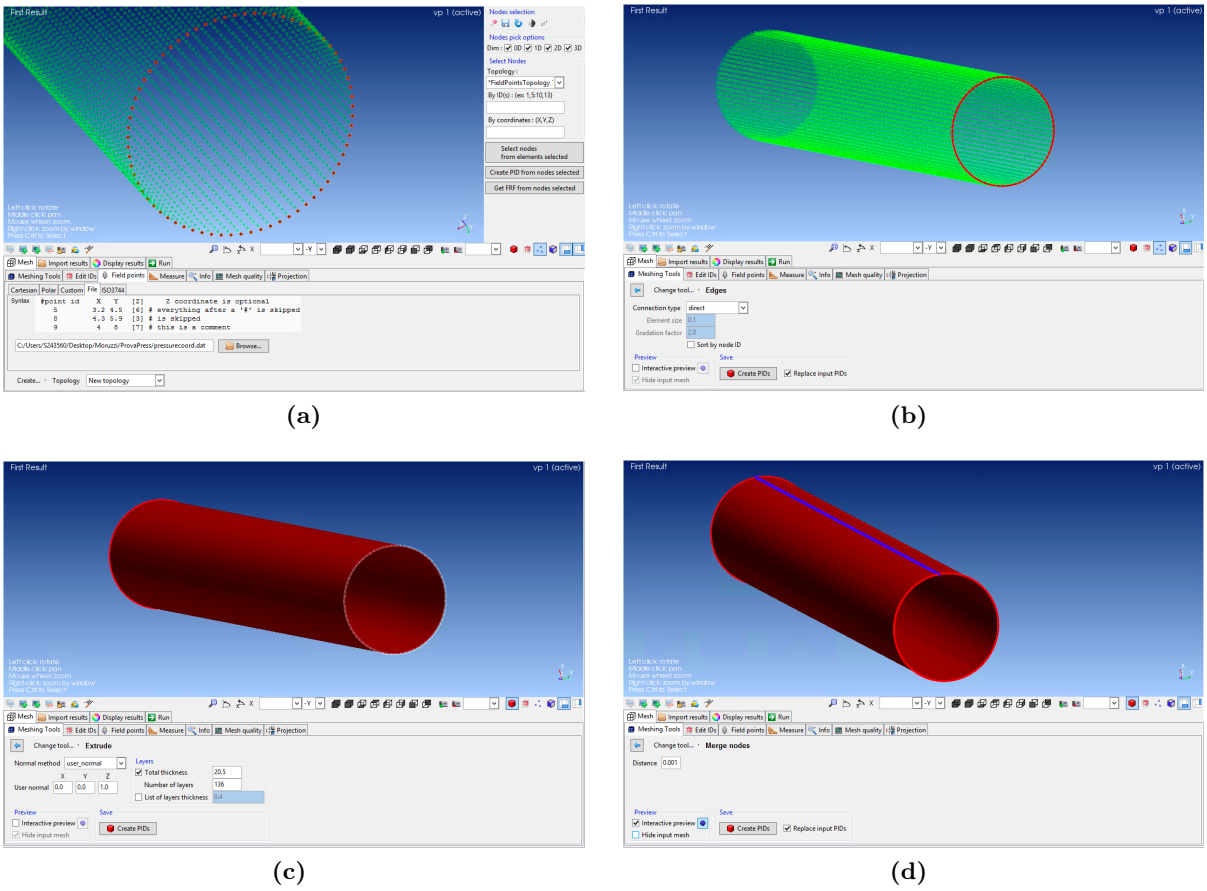

Figure 3.4: (a) The imported nodes (green) and the 0D element set (red) (b) The created circle (red) from 0D element set. (c) The extruded surface, the new circle (red) and the input mesh (green). (d) The finished new mesh, the two circles and the surface (red), and the duplicate points (blue).

needed. The chosen criterion, number of elements per wavelength, is k. The smallest wavelength in our problem is λ_{min} and depends on the material and maximum frequency in the analysis. It is possible to calculate the maximum element size h to capture the λ_{min}:

$$h = \frac{\lambda_{min}}{k} \, . \tag{3.10}$$

In this model we chose 7 linear elements and 3 quadratic elements per wavelength criterion, so $k_{lin} = 7$ and $k_{quad} = 3$.

The minimum wavelength for each type of material is calculated as follows:

- for a fluid[2] the wavelength can be write as

$$\lambda = \frac{c}{f} \tag{3.11}$$

in which the frequency f is a chosen parameter and the sound speed c depends on the fluid;

[2]Free field radiation of a monopole, Actran Student Edition tutorial, October 31, 2017

- for an isotropic solid material[3] the bending wavelength is defined as

$$\lambda_{bend} = \frac{c_{bend}}{f} \tag{3.12}$$

in which the frequency f is a chosen parameter and the bending sound speed c_{bend} depends on the material and the component characteristics (Young modulus E, Poisson ratio ν, thickness t and density ρ) and, defining the pulsation as $\omega = 2\pi f$, we obtain

$$c_{bend} = \sqrt{\omega \cdot t \sqrt{\frac{E}{12 \cdot \rho \cdot (1-\nu^2)}}} = \sqrt{\pi \cdot t \cdot f \cdot \sqrt{\frac{E}{3 \cdot \rho \cdot (1-\nu^2)}}}\ ; \tag{3.13}$$

- for an orthotropic material the minimum wavelength over the three directions of shear waves is calculated using equation 3.12, where the sound speed is:

$$c = \sqrt{\frac{G_{ij}}{2 \cdot \rho}} \tag{3.14}$$

in which G_{ij} is the shear modulus over one in the three directions and ρ the density of the material. The element size will be the minimum h over the three directions.

The wavelength (or bending wavelength), the element size and shear wavelength could be calculated by Actran VI internal tool.

3.2.5 Interfaces and coupling surfaces

To assemble two different components for an acoustic analysis there are two ways:

- compatible mesh, the two components share the same nodes, Fig. 3.5;
- incompatible mesh, the two components overlap, but they do not share the same nodes[4], Fig. 3.6.

In the second case an interface between the two components must be created within two coupling surfaces for the two components. The first coupling surface will be projected on the second coupling surface. To obtain the best projection the first coupling surface must have the smallest elements, while the second the largest elements and the ratio of the two surfaces elements sizes must be 1:3 or lower. In Actran it is possible to define a tolerance between the two surfaces. This tolerance is composed by a gap and plane tolerance. The gap tolerance defines the extrusion of the second surface in the normal direction. The plane tolerance defines a new extrusion in all directions, to capture nodes not in the normal direction.

An error borns with semi-incompatible meshes (Fig. 3.7), when some nodes are shared and other not. To overcome this problem we applied the solution in [27], a small gap, lower than gap tolerance, is inserted between the two surfaces.

An interface must be created between a solid component and a fluid component (a plate and a cavity) where often the mesh for the fluid is looser than that of the plate, or between two surfaces

[3] Extraction of plate modes, Actran Student Edition tutorial, November 3, 2017
[4] Forced response of coupled plate and cavity, Actran Student Edition tutorial, November 7, 2017

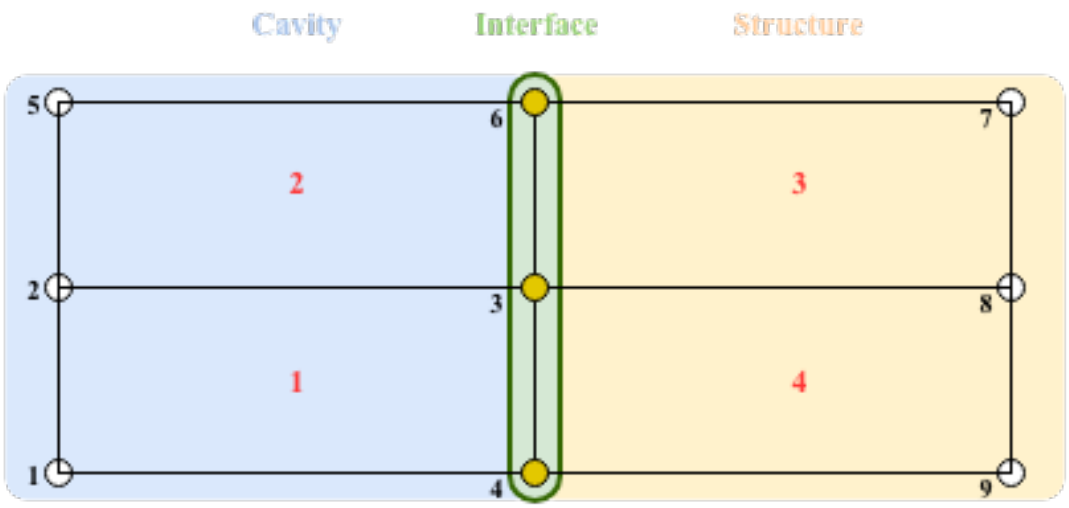

Figure 3.5: A compatible mesh: nodes 6, 3 and 4 belong to both components: cavity and structure.

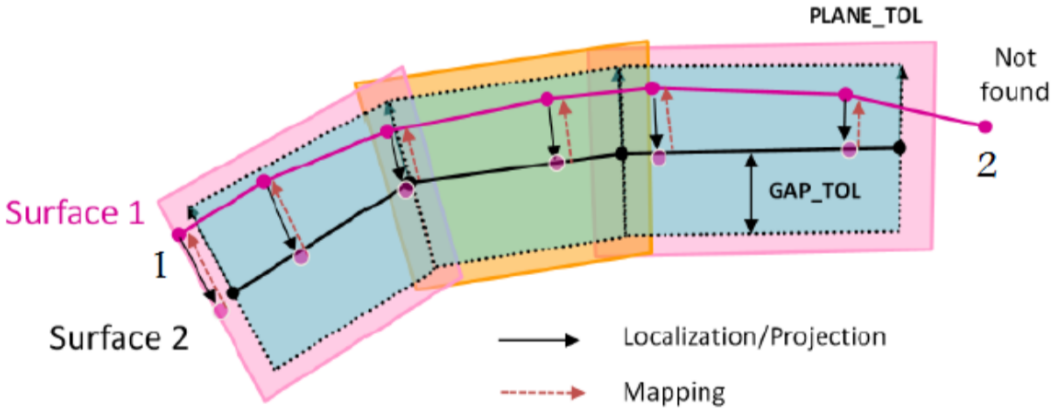

Figure 3.6: An incompatible mesh with gap and plane tolerance.

that are not geometrically identical to transfer a boundary condition as a pressure load or an admittance condition.

Actran includes a projection tool which gives information about the quality of incompatible meshes projections with different tolerances. The percentage of included nodes projected and a quality map could be visualized. As example, in Fig. 3.8 the projection between the fuselage and the air cloak, that are defined on different nodes, is shown.

3.2.6 PLTViewer

The PLTViewer is the dedicated post-processing utility to visualize Actran's frequency response functions (FRF). It contains various operators (such as dB, dBA, TL indicator, NR indicator, etc.) which allows to compute, plot, compare and export a wide range of quantities.

3.2.7 WATERFALLViewer

The WATERFALLViewer is the graphical tool of Actran VI to display in waterfall diagram results for several loadcases. Inside WATERFALLViewer the modal assurance criterion (MAC) could be calculated to compare modal extractions, validate the models and optimize the designs.

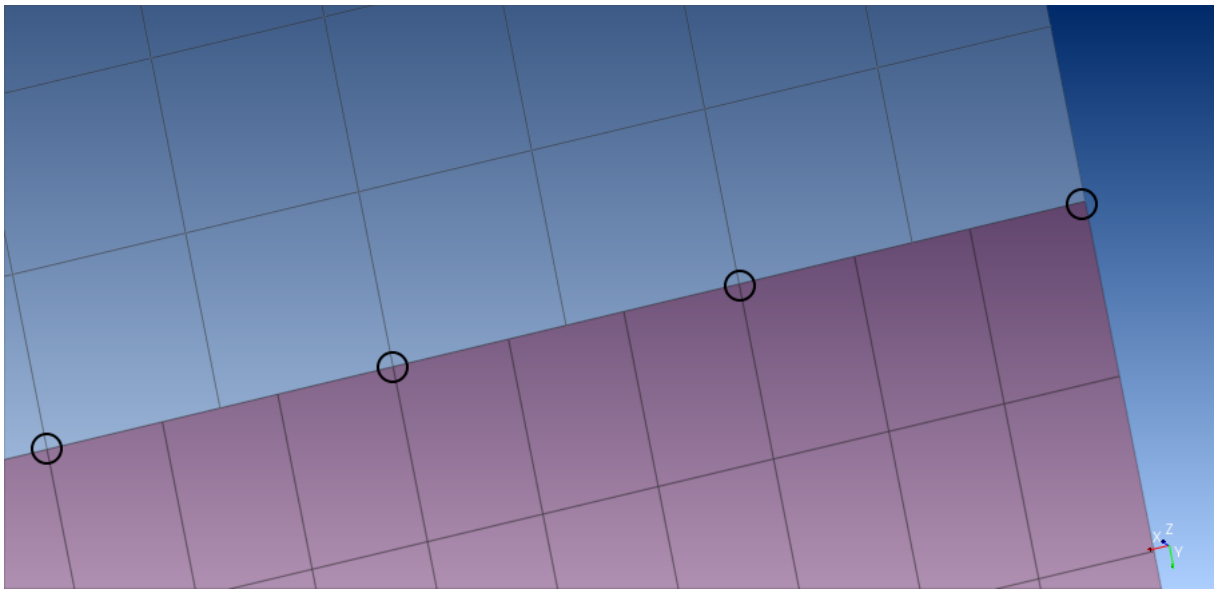

Figure 3.7: Semi-incompatible meshes with shared nodes (black circles).

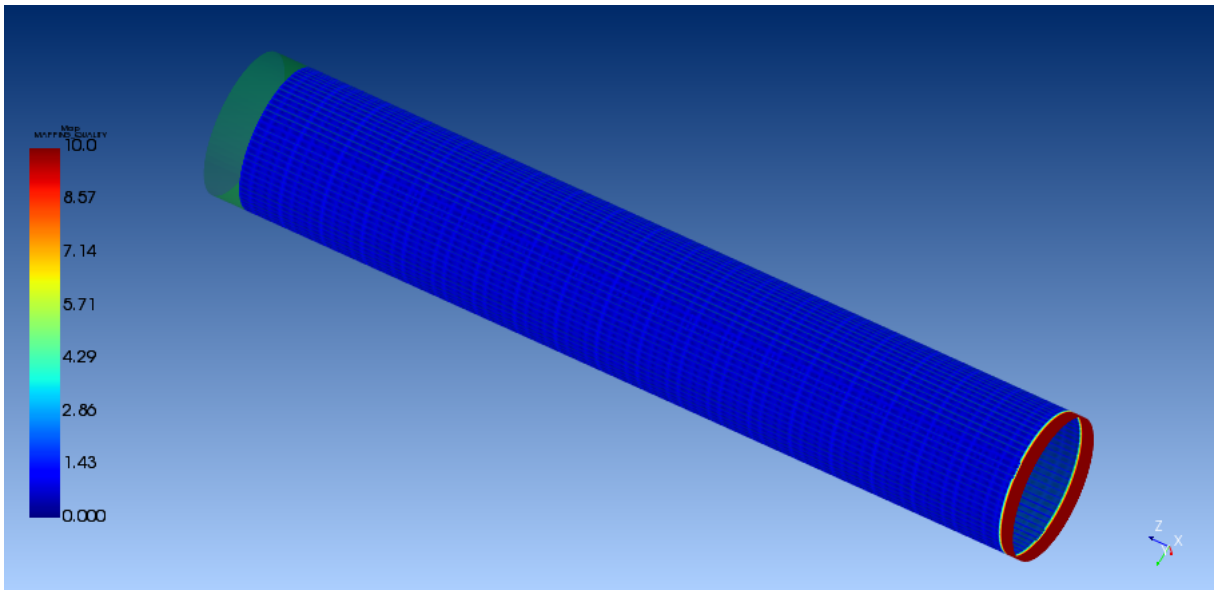

Figure 3.8: Projection between the fuselage and the pressure field, the first mesh results well projected on the second for the major part of the fuselage (blue) and not projected on edges (red), that because the pressure field is larger than the fuselage.

Chapter 4

Aircraft model

4.1 Introduction to the model

The aircraft model, using FEM (finite elements method), is a baseline fuselage of 20 m length, used to demonstrate the effectiveness of the acoustic solutions at low frequencies. The purpose is to create a system that reproduces the dynamic behavior of the real structure in terms of mechanical impedance and coupling between the fuselage airframe and the fluid contained within it. The FEM model is composed by 0D, 1D, 2D and 3D elements and a convergence analysis was already performed and demonstrated by D'Amico. This model does not include overheads and pressure loads. In the new model two overheads above seats are added to better describe

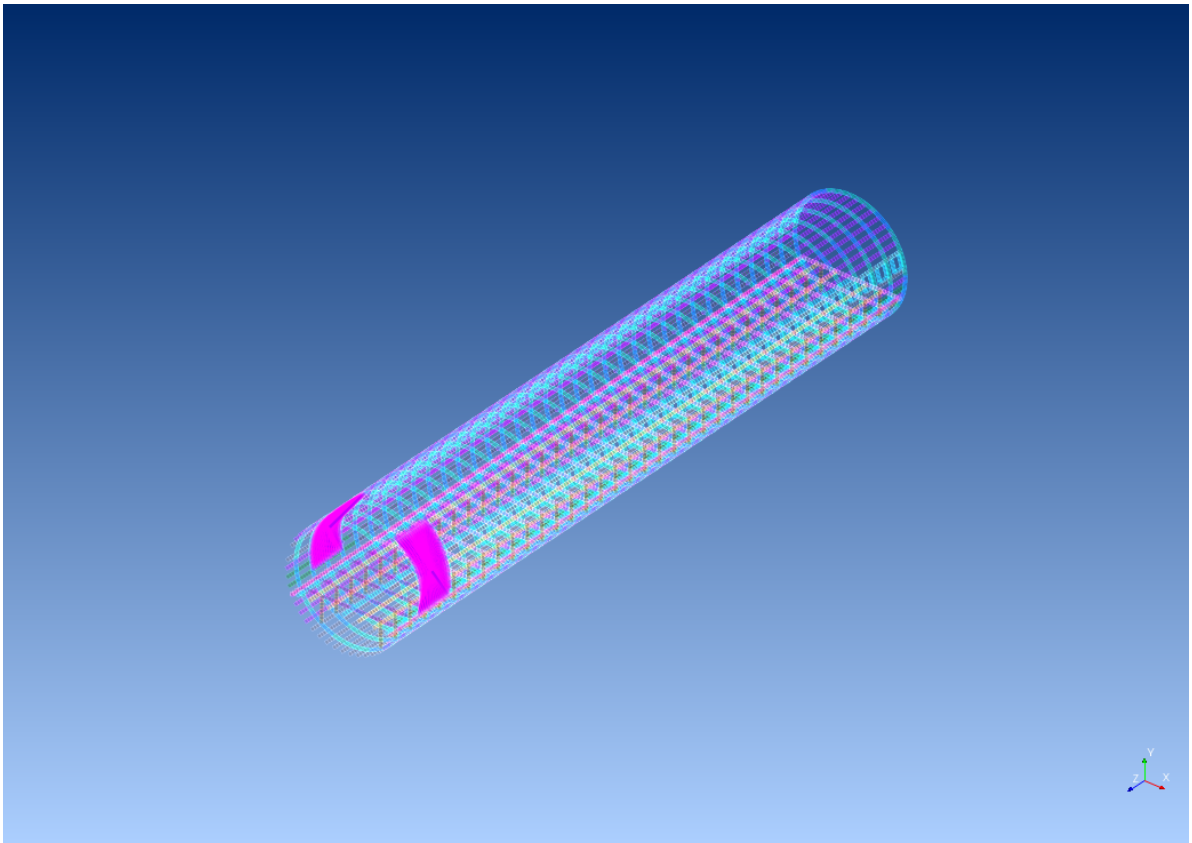

Figure 4.1: Model of the skeleton: 0D and 1D elements.

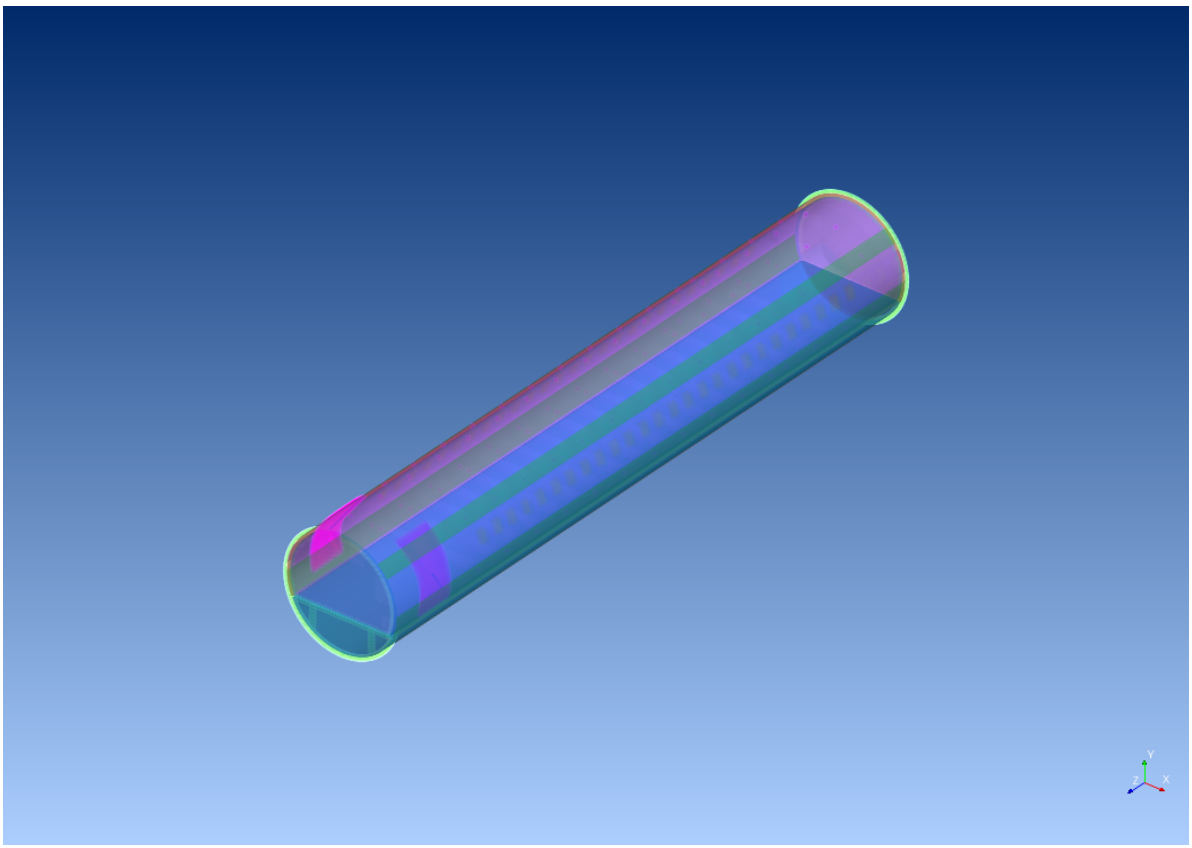

Figure 4.2: Model of the skin and cavities: 2D and 3D elements.

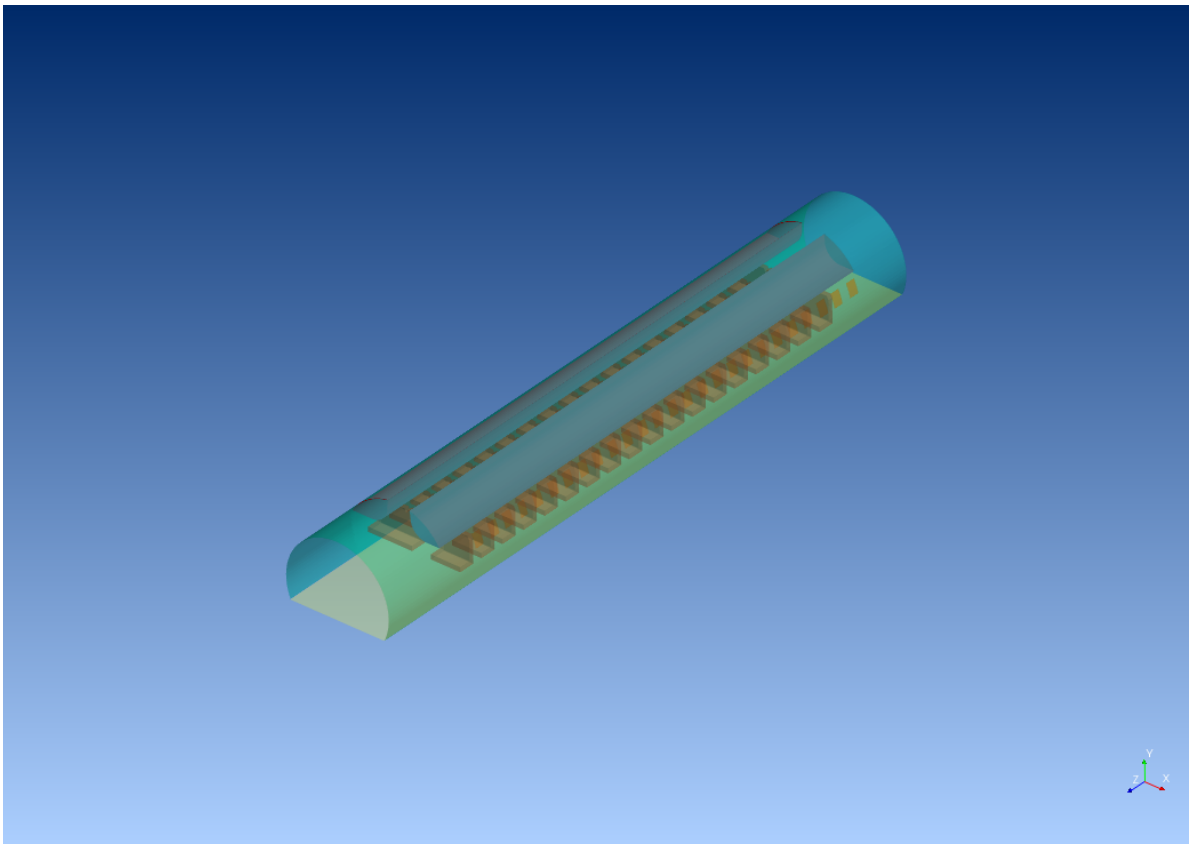

Figure 4.3: Passengers cabin with trim panel, overheads, floor and seats.

the cabin design and the external pressure loads are imposed as boundary condition (see section 4.2 and 4.7.4). Moreover some other arrangements has been performed, as changing or updating meshes, components as interfaces and coupling surfaces or adding output requests.

The skeleton of the model is shown in Fig. 4.1, the skin and cavities of the model in Fig. 4.2 and the passenger cabin in Fig. 4.3.

4.2 Loads

The loads calculated by CIRA (*Centro Italiano di Ricerca Serospaziale*) represent the pressure field generated at Blade Passage Frequency (BPF) by two 8-blades propellers rotating clockwise with 20 degrees relative phase angle (Fig. 4.4) in the first three harmonics, that occur at 100 Hz, 200 Hz and 300 Hz according to the number of blades and propeller rotational per minute (RPM) at cruise velocity (provided by LNDVEL), as described in [42] . The aerodynamic pressure has been calculated using Blade Element Momentum Theory (BEMT) and then, from the aerodynamic pressure, the acoustic pressure distribution over the fuselage external skin has been computed through a FW-H (Ffowcs Williams and Hawkings) approach. The pressure field is calculated on mesh of 9792 nodes that represent the aircraft fuselage.

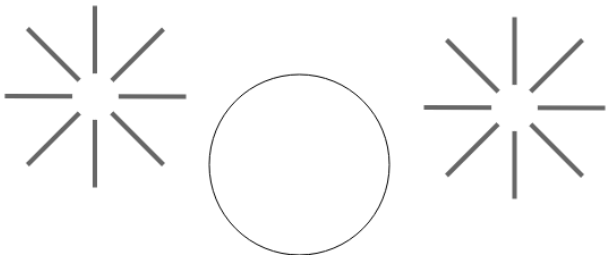

Figure 4.4: 8-blades propellers configuration.

The pressure is a complex value in Pascal, function of spacial coordinates x, y and z (and of frequency f), in the rows below the first lines (from 1 to 9792) and the last of the `.dat` first file (100 Hz), from CIRA, are reported (after the last line there would be the connectivity matrix):

```
TITLE=OPTYDB MESH
Variables=
" x ", " y ", " z ", "real_p_[Pa]", "imag_p_[Pa]",
ZONE T="QUAD, COLOR Microphone surface", N=9792, E=9585, F=FEPOINT,
ET=QUADRILATERAL
0.60000000E+01 0.17250000E+01 0.00000000E+00 0.47075582E+00 -0.45896155E+00
0.60000000E+01 0.17181100E+01 0.15245999E+00 0.40628935E+00 -0.52031671E+00
0.60000000E+01 0.16980100E+01 0.30371100E+00 0.33806335E+00 -0.56471466E+00
.
.
.
0.26500000E+02 0.17181100E+01 -0.15245999E+00 0.14802786E-01 0.11755782E-01
0.26500000E+02 0.17250000E+01  0.30160999E-06 0.14559705E-01 0.13343448E-01
```

The loads are reported in Fig. 4.5 for 100 Hz, Fig. 4.6 for 200 Hz and Fig. 4.7 for 300 Hz both the real and imaginary part in Pascal.

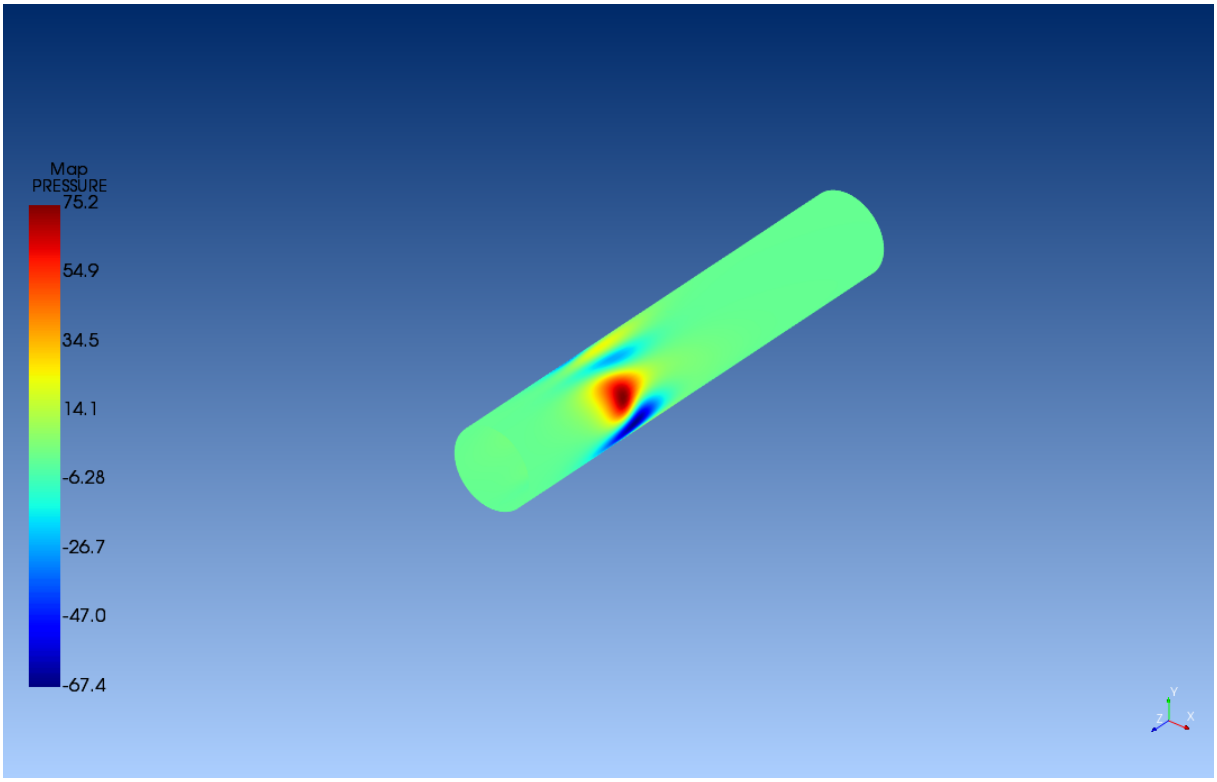

(a)

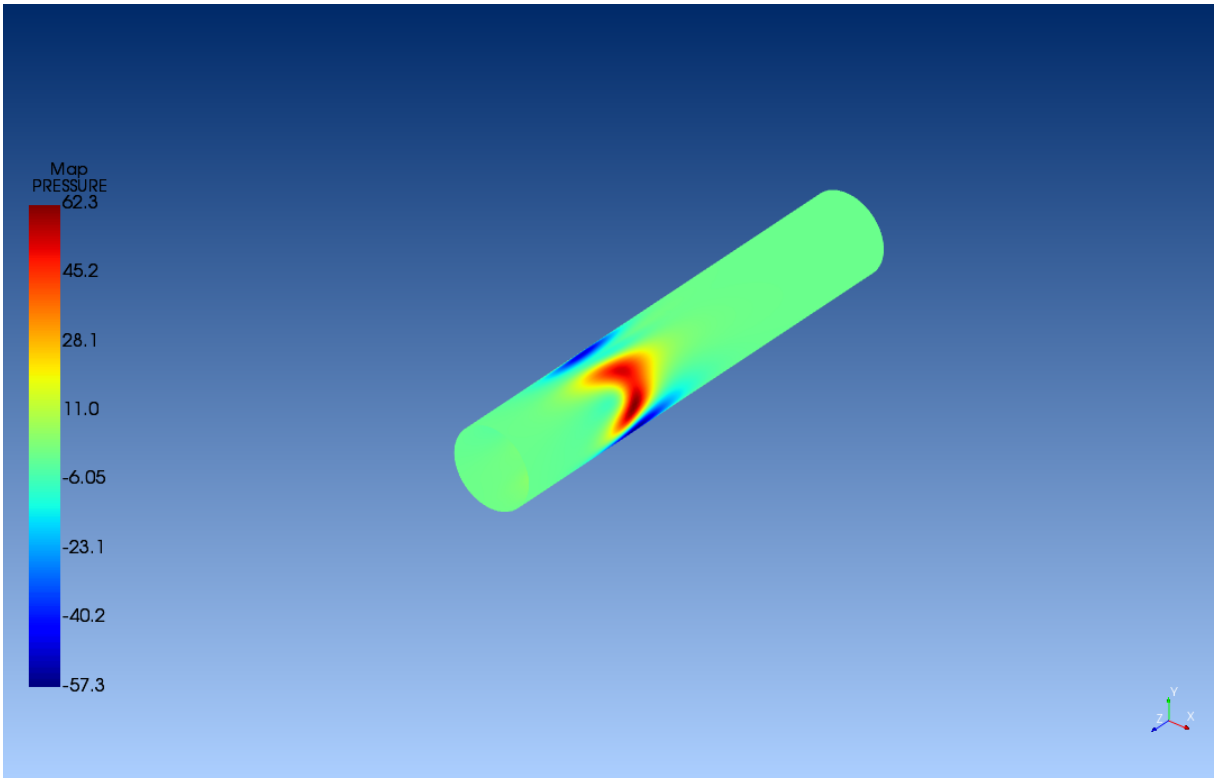

(b)

Figure 4.5: Pressure loads [Pa] for the first tonal frequency 100 Hz. (a) Real part. (b) Imaginary part.

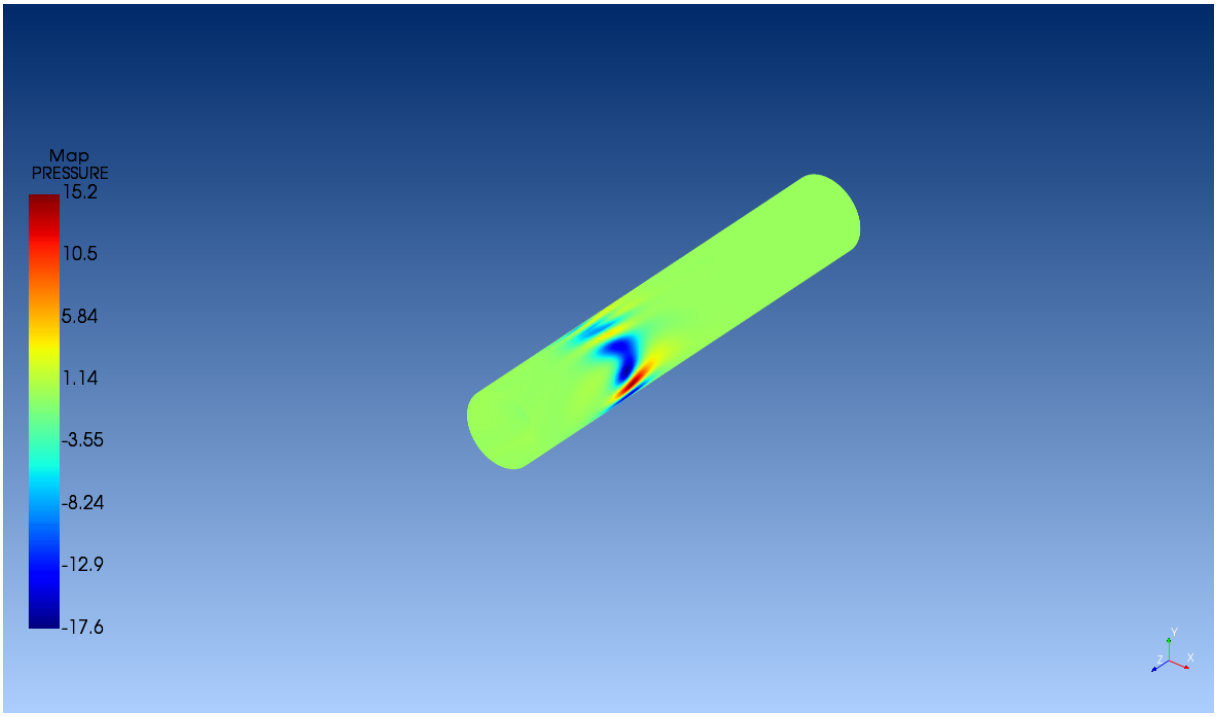

(a)

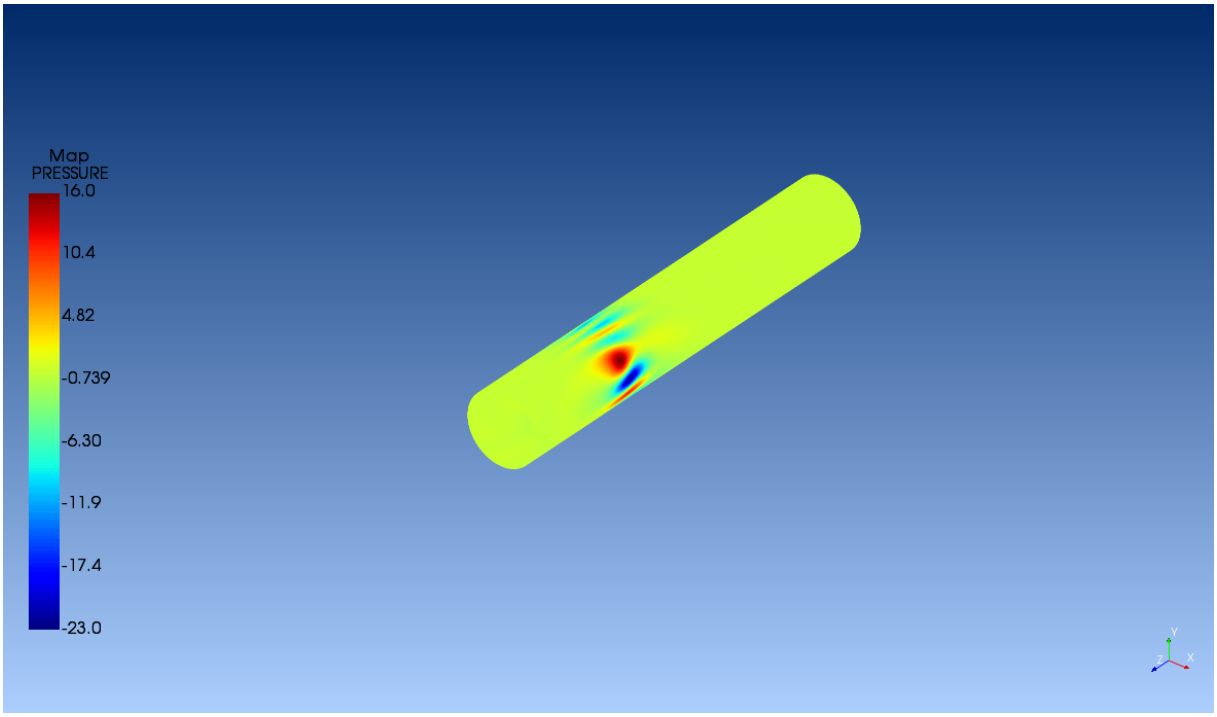

(b)

Figure 4.6: Pressure loads [Pa] for the second tonal frequency 200 Hz. (a) Real part. (b) Imaginary part.

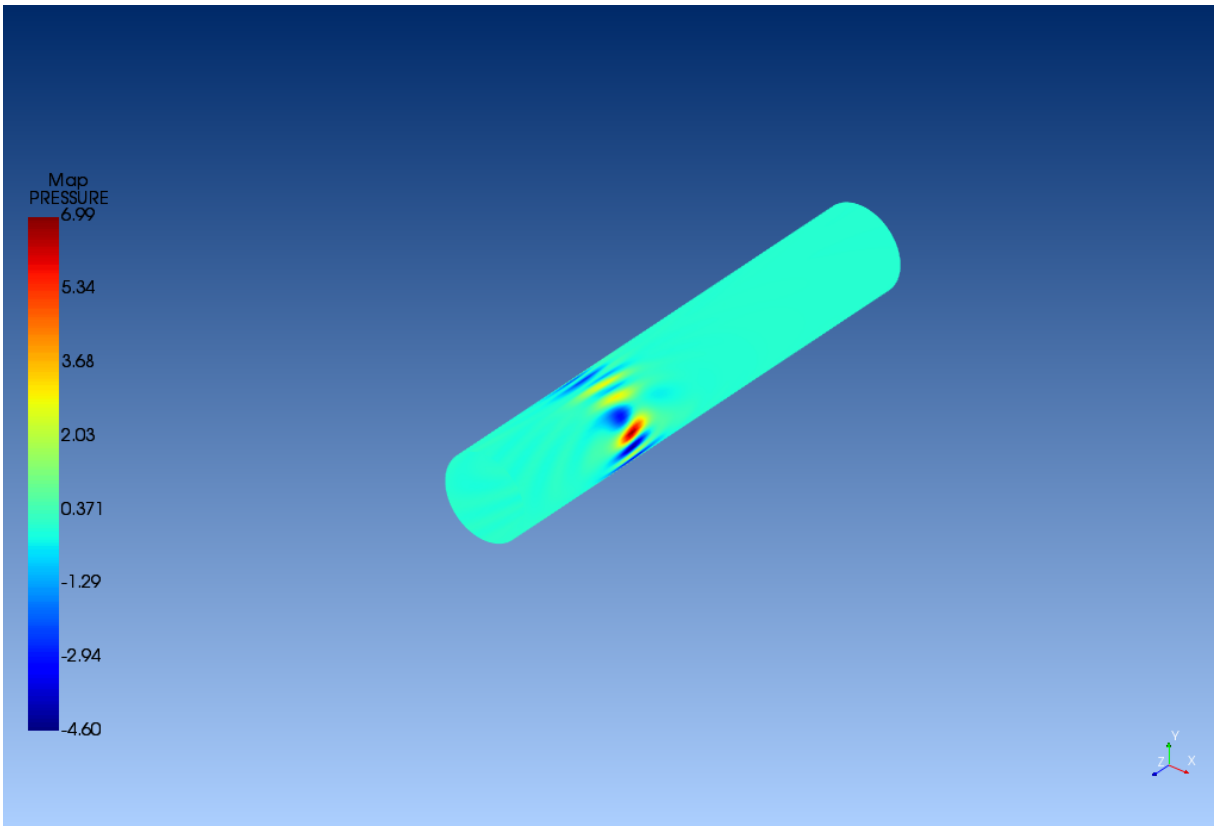

(a)

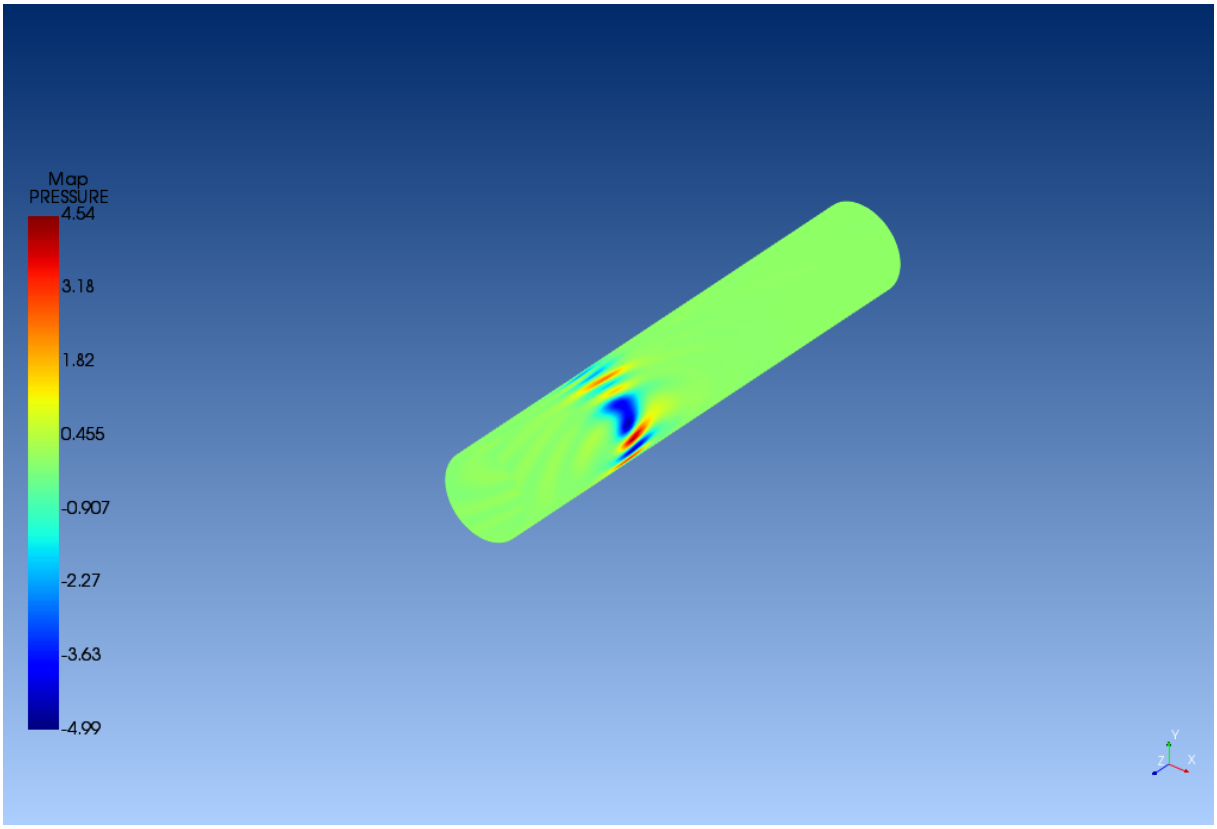

(b)

Figure 4.7: Pressure loads [Pa] for the third tonal frequency 300 Hz. (a) Real part. (b) Imaginary part.

4.3 Acoustic solutions

The plain aircraft does not exploit any acoustic solution to reduce cabin noise. The trim panel is made with an orthotropic material (Nomex) surrounded by two plates of fiberglass and epoxy foam and there are windows. This is the reference model on which the other model are related to compare results.

Nomex is an orthotropic material with only structural purpose, its characteristics are reported in Tab. 4.1. The fiberglass plates characteristics are reported in Tab. 4.2. The trim panel core (Nomex) has a thickness of 0.006 m, while the plates have a thickness of 0.00048 m each, with a single layer thickness of 0.00024 m and an orientation of the fibers equal to 0° and 90°. Density of Nomex is equal to 48 kg/m^3 and the plates density is equal to 1950 kg/m^3.

Table 4.1: Characteristics of the composite material Nomex in SI.

Young Modulus Along Direction 1*	100000
Young Modulus Along Direction 2*	100000
Young Modulus Along Direction 3*	90000000
Poisson Ratio in plane (1,2)*	0.99
Poisson Ratio in plane (1,3)*	0.0002
Poisson Ratio in plane (2,3)*	0.0002
Shear Modulus in plane (1,2)*	100000
Shear Modulus in plane (1,3)*	15000000
Shear Modulus in plane (2,3)*	31000000

Table 4.2: Fiberglass with epoxy foam characteristics in SI.

Young Modulus Along Direction 1*	20000000000
Young Modulus Along Direction 2*	20000000000
Young Modulus Along Direction 3*	3600000000
Poisson Ratio in plane (1,2)*	0.13
Poisson Ratio in plane (1,3)*	0.27
Poisson Ratio in plane (2,3)*	0.27
Shear Modulus in plane (1,2)*	4000000000
Shear Modulus in plane (1,3)*	4300000000
Shear Modulus in plane (2,3)*	4300000000

Two acoustic solutions are applied: metamaterial for the trim panel and fuselage exploiting a windowless configuration.

The chosen metamaterial is a melamine foam with cylindrical inclusions of aluminium with volume fraction of 0.015, its frequency dependance characteristics are reported in Tab. 4.3 and calculated by D'Amico in [27]. The advantages of using melamine (formaldehyde-melamine-sodium bi-sulfite copolymer) are high sound absorption capacity, low weight, good thermal insulation properties and flexibility at very low temperature and moreover this material is fireproof. Aluminium is used because of its proven efficiency in aeronautics. The transmission loss of the metamaterial is compared with that of the Nomex in Fig. 4.8 by D'Amico. The total density of this metamaterial is very similar to the density of Nomex: 48.38 kg/m^3 for the metamaterial

instead of 48.00 kg/m^3 for the Nomex. The two fiberglass plates and the thickness of the core are not changed.

The second acoustic solution is to have the fuselage and the trim panel without windows as already described in section 2.3. The windows are made of tempered glass and plexiglass (Tab. 4.4) and they have a thickness of 0.003 m for each layer. The transmission loss calculated on 2D model plate of fuselage composite material near the windows (and with the windows removed and their holes "filled") and windows materials, is shown in Fig. 4.9. The air between the two materials of the windows is neglected, although it would be have a positive effect on the sound reduction.

Table 4.3: Homogenized characteristics of the metamaterial composed by a melamine foam with cylindrical inclusions of aluminium with volume fraction of 0.015.

Frequency [Hz]	**100**		**200**		**300**	
	Im	Re	Im	Re	Im	Re
E_x [Pa]	1.541E+06	5,182E+03	1.549E+06	6.344E+03	1.555E+06	7.115E+03
E_y [Pa]	2.883E+05	2.467E+03	2.899E+05	3.020E+03	2.910E+05	3.387E+03
E_z [Pa]	1.014E+09	2.040E+03	1.014E+09	2.497E+03	1.014E+09	2.801E+03
ν_{xy}	2.194E-01	8.574E-03	2.194E-01	8.574E-03	2.194E-01	8.574E-03
ν_{xz}	-4.973E-01	1.000E-07	-4.973E-01	1.000E-07	-4.973E-01	1.000E-07
ν_{yz}	4.274E-01	1.000E-07	4.274E-01	1.000E-07	4.274E-01	1.000E-07
G_{xy} [Pa]	1.064E+05	1.174E+03	1.069E+05	1.437E+03	1.073E+05	1.612E+03
G_{xz} [Pa]	1.306E+05	1.464E+03	1.313E+05	1.792E+03	1.318E+05	2.010E+03
G_{yz} [Pa]	1.098E+05	1.231E+03	1.104E+05	1.507E+03	1.108E+05	1.690E+03

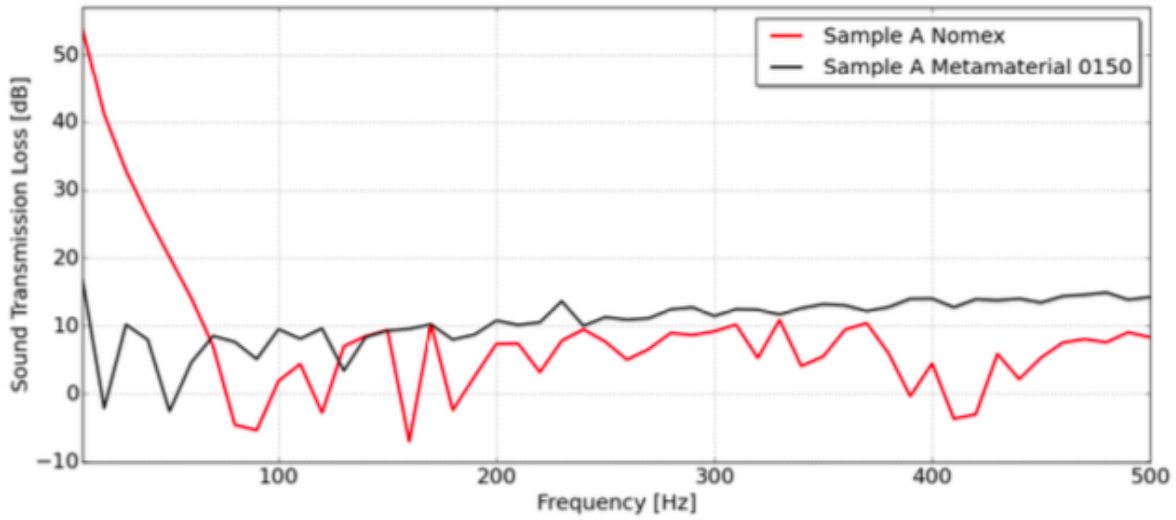

Figure 4.8: Nomex (red) and metamaterial (black) transmission losses [dB] compared.

Table 4.4: Windows isotropic materials (tempered glass and plexiglass) characteristics.

	Tempered glass	**Plexiglass**
E [Pa]	4.00E+10	2.79E+09
ν	0.22	0.37
ρ [kg/m^3]	2200	1180

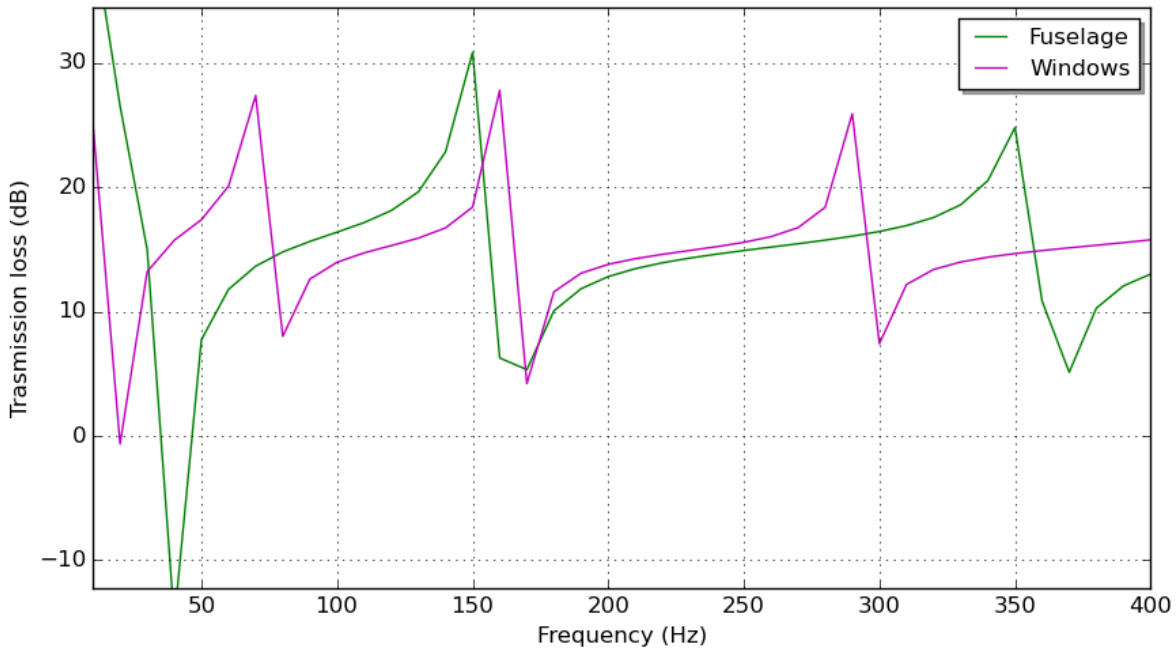

(a)

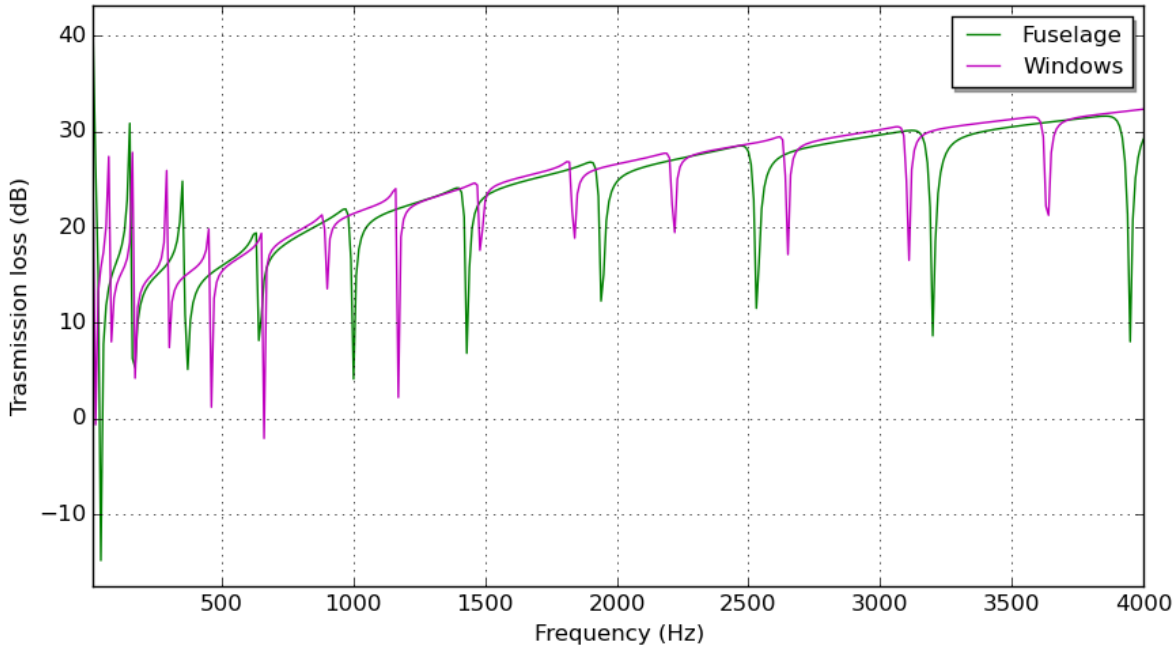

(b)

Figure 4.9: Transmission loss [dB] due to the fuselage skin near the windows (green) and due to the windows (purple). (a) From 10 to 400 Hz. (b) From 10 t0 4000 Hz.

4.4 Geometry

The model represents an aircraft with length of 19.88 m, external diameter of 3.45 m and passengers cabin height of 2.26 m. The model's dimensions are reported in Fig. 4.10(a) and Fig. 4.10(b). The windows sizes are reported in Fig. 4.12 and the seats sizes in Fig. 4.11.

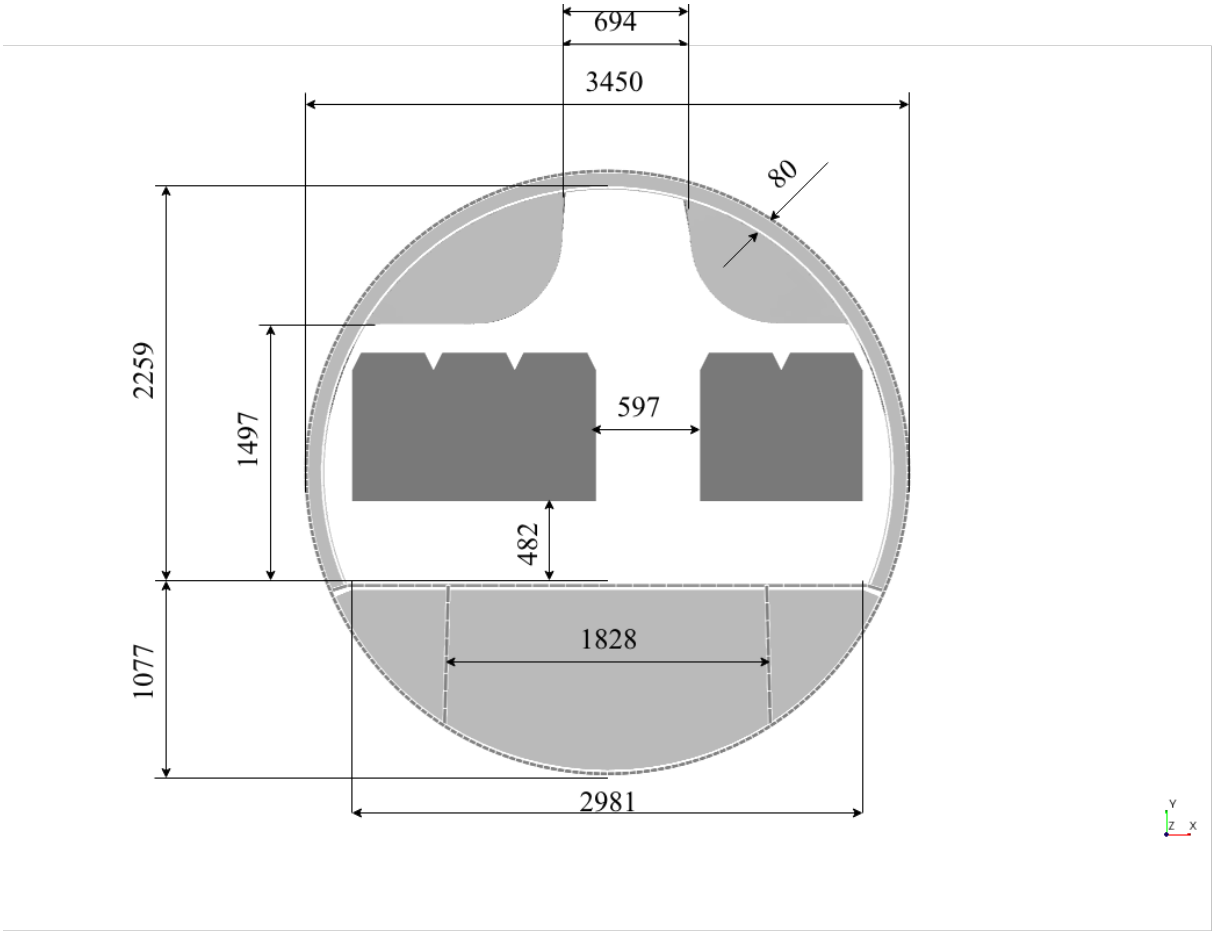

(a)

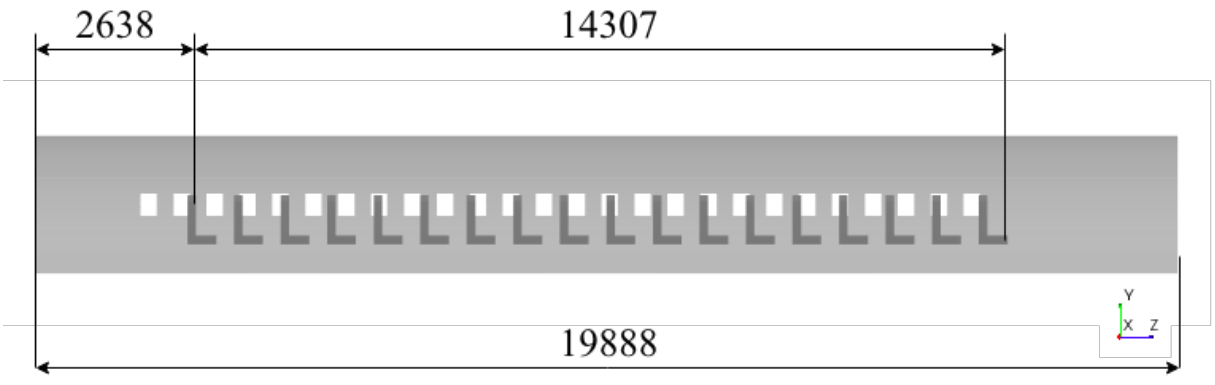

(b)

Figure 4.10: Dimensions of the model in mm. (a) Front view (b) Lateral view.

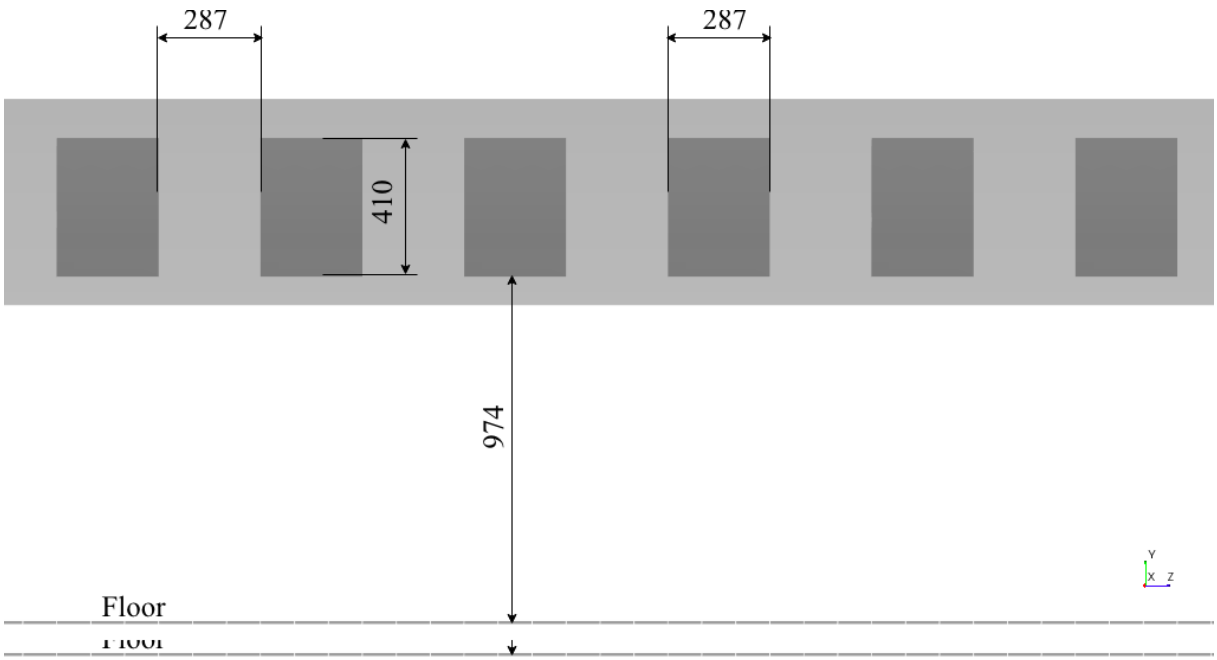

Figure 4.11: Windows sizes in mm.

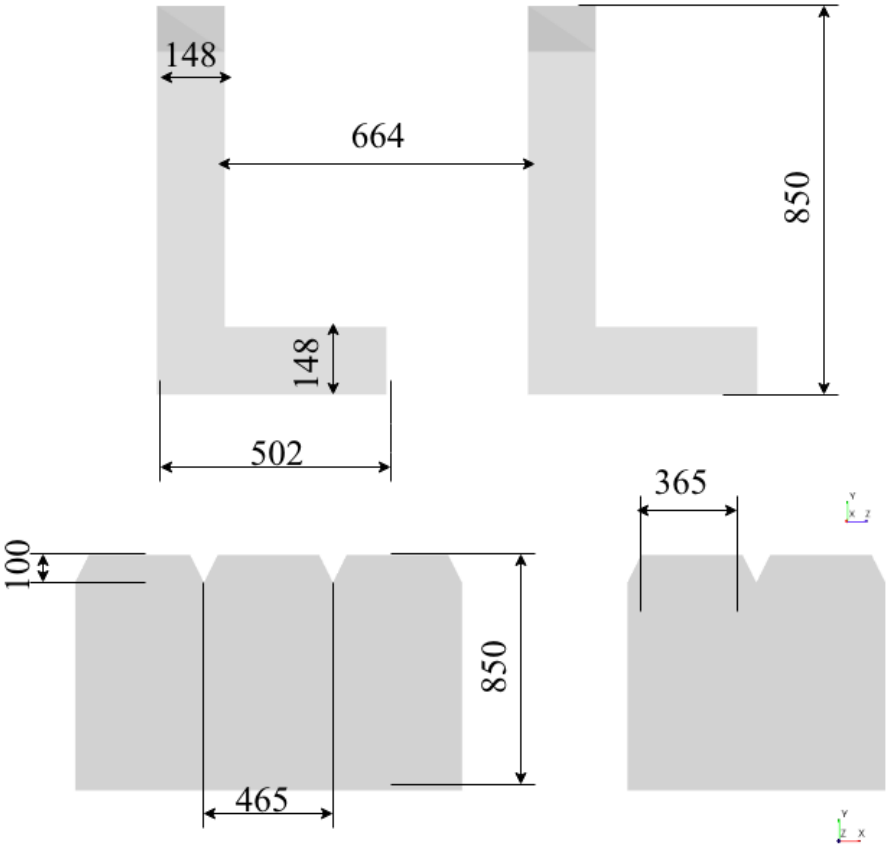

Figure 4.12: Seats sizes in mm.

4.5 Mesh quality

Mesh is composed by 0D, 1D, 2D and 3D elements, with linear interpolation, except the trim panel, that has elements with a quadratic interpolation. Linear interpolation has less computational cost, but needs a wavelength criterion of at least 7, while quadratic of 3 (see section 3.2.4). Possible elements types are shown in Fig. 4.13[1]. For 2D elements there are two types of elements: triangular (tria) and quadrangular (quad), both used. For 3D elements, hexahedral (hexa) type is used, at the expense of tetrahedron (tetra).

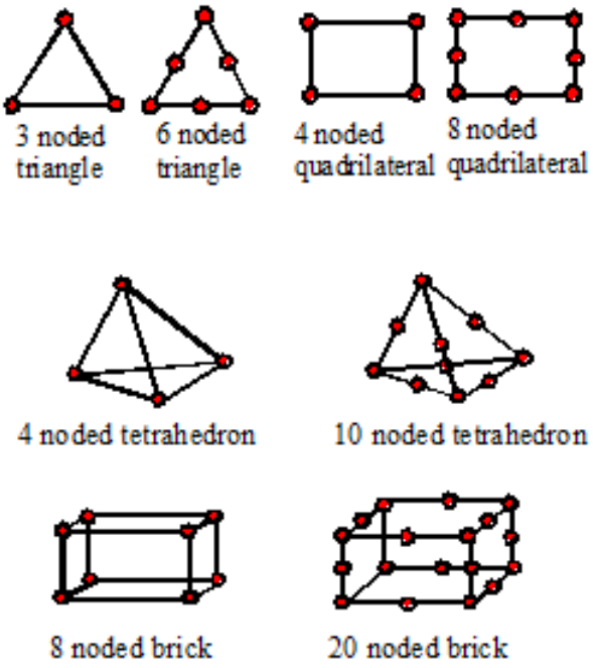

Figure 4.13: Possible element types with linear and quadratic interpolation, form top left angle: tria, quad, tetra, hexa.

The size of the elements has to follow three principles:

- wavelength criterion;
- computational cost and time;
- best modeling of the real aircraft components, particularly close to angles or junctions.

Furthermore elements must have Jacobian determinant ratio more possible near to 1, so they do not have to be too irregular. Only 3520 elements (0.27%) have Jacobian determinant ratio lower than 0.7.

The total number of elements is equal to 1291973 (created in the analysis 1481150), the degrees of freedom of the problem to 2246063 and the topological dimension to 3. Elements types and dimensions are reported in Tab. 4.5 and Fig. 4.14. The elements distribution through the different components is reported in Tab. 4.6 and Fig. 4.15. It is possible to see that the greater part of the elements, 68.17%, are used to model the 3D components (air cavities, trim panel, air cloak).

Table 4.5: Distribution of elements based on their dimension.

Element dimension	Linear	Quadratic	Unused (linear)	Total	%
3D	832287	48472	0	880759	68,17
2D	384841	0	996	385837	29,86
1D	24327	0	0	24327	1,88
0D	908	0	142	1050	0,08
Total	1242363	48472	1138	1291973	100,00

Table 4.6: Distribution of elements based on their component.

	N. of elements	%	Element size [m]			Type	Dimension
			size 1	size 2	size 3		
Air cavities	822702	63,68	0,14	0,14	0,14	Hexa	3D
Trim panel	48472	3,75	0,05	0,05	0,006	Quad	3D
Seats	13428	1,04	0,1394	0,1394	-	Tria	2D
Overheads	37340	2,89	0,033	0,04	-	Quad	2D
Shell fuselage	58856	4,56	0,041	0,095	-	Quad	2D
Skeleton	24327	1,88	0,041 & 0,096 & 0.1	-	-	-	1D
Air cloak	9585	0,74	0,152	0,152	0,001	Hexa	3D
Floor	6448	0,50	0,096	0,096	-	Quad	2D
Edge	908	0,07	-	-	-	-	0D
Trim panel shells	99416	7,69	0,05	0,05	-	Quad	2D
Field	4500	0,35	0,098	0,098	-	Quad	2D
Coupling surfaces	164853	12,76	Same of the 3D meshes at which they refer			Tria/Quad	2D
Unused meshes	1138	0,09	NA			NA	NA
Total	1291973	100,00	-				

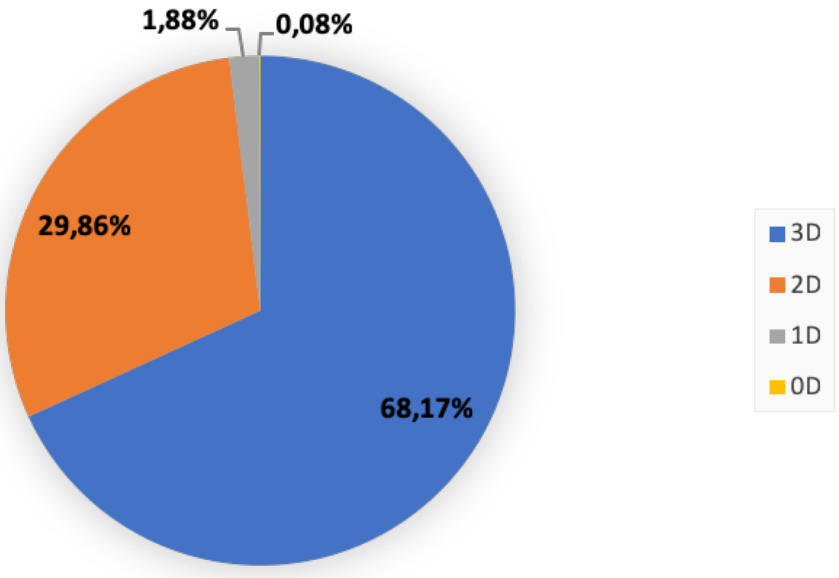

Figure 4.14: Distribution of elements based on their dimension.

The mesh quality is calculated in Tab 4.7 and the results shown in Fig. 4.16. All meshes are above their criterions except the meshes of trim panel, overheads and windows, for the maximum frequency in the analysis (300 Hz). Windows have a value of 6.87, that it is still acceptable (the results for this component could have a maximum inaccuracy of 1.85%). The overheads are unchanged to maintain elements size similar to the elements size of the external shell. Finally

[1] https://www.quora.com extracted on the 9th of May 2019.

the trim panel mesh, despite it is below the 3 elements per wavelength, it does not cause a drop of accuracy.

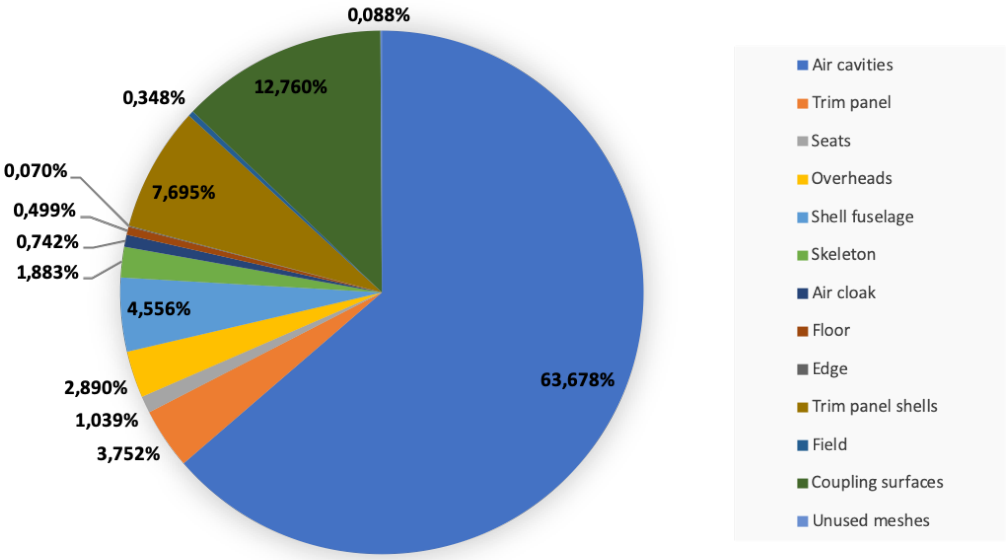

Figure 4.15: Distribution of elements based on their component.

Table 4.7: Elements per wavelength for each components at 300 Hz.

Component	Criterion k	Minimum k	Type of material
Top panels	63,86	7	Orthotropic
Bottom panels	64,16	7	Orthotropic
Around wind panels	82,99	7	Orthotropic
Lateral panels 1	70,45	7	Orthotropic
Lateral panels 2	78,70	7	Orthotropic
Windows	6,87	7	Isotropic
Air cavities	8,10	7	Fluid
Overheads	2,59	7	Isotropic
Air cloak	7,46	7	Fluid
Floor	9,13	7	Isotropic
Trim panel shells	70,00	7	Composite
Trim panel: Nomex	2,15	3	Orthotropic
Trim panel: Metamat.	2,22	3	Metamaterial

Each analysis takes almost one hour per frequency to end, including the creation of the structure, the time to solve the equations and the saving of the results.

4.6 Types of materials

The aircraft's components are principally made by orthotropic and composite materials, although some elements by isotropic materials. Air cavities are defined using finite fluide (air). In Actran, to define beam components, beam inertia materials are used.

The fuselage shell and the trim panel core are made of orthotropic materials. The trim panel core could be made of Nomex or metamaterial (melamine foam with cylindric inclusions in

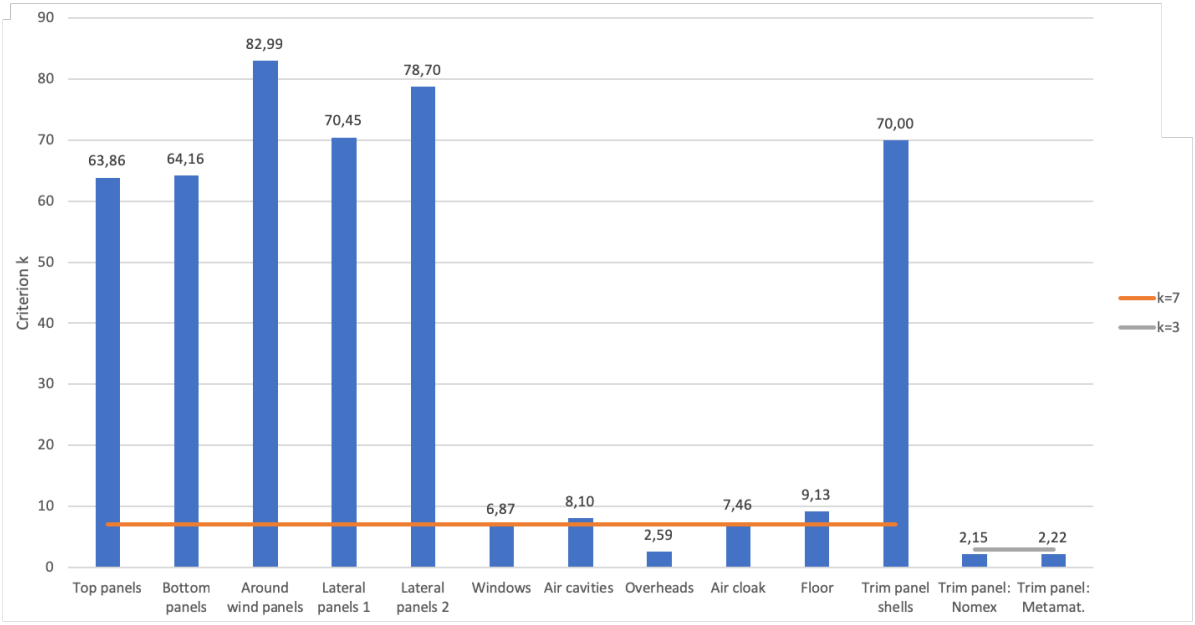

Figure 4.16: Elements per wavelength for each component at 300 Hz.

aluminium). An orthotropic material is defined by the Young modulus E_i in the direction i, the Poisson's ratio ν_{ij} that corresponds to a contraction in direction j when an extension is applied in direction i, the shear modulus in direction j for which the shear load relies on the plane whose normal is in direction i and the solid density ρ_S. The directions are referred to the local coordinates system.

The trim panel shell are made of a composite material: two fiberglass epoxy layers. The single layer is defined as an orthotropic material. The composite material is built defining the layers and their thicknesses and orientations. Furthermore the two materials of the windows are modeled as a single composite material.

Windows layers, overheads and floor are made of an isotropic material, defined by the Young modulus E, the Poisson's ratio ν and solid density ρ_S. The overheads are made of PVC (polyvinyl chloride).

Finite fluid, in particular air, is used to define the cavities and the air cloak around the fuselage. The sound speed c and fluid density ρ must be specified.

Beam inertia materials allow to specify equivalent stiffeners mechanical properties using inertia indicators. Elongation modulus E_T, shear modulus G and solid density ρ_S must be specified. Furthermore the cross section area A, the cross section inertias (I_{XX}, I_{YY} and I_{XY}), the shear factors e_{SX} and e_{SY} and the torsional inertia I_Z are defined. This type of materials is used to models beam components, as stringers, spars and bridge supports.

4.7 Actran analysis

4.7.1 Parameters

The analysis is a direct frequency response for the three tonal frequencies of the pressure loads: 100 Hz, 200 Hz and 300 Hz. At each frequency the relating load is applied. The analysis are made

Table 4.8: Analysis overview.

Frequency [Hz]	Trim panel material	Windows
100	Nomex	Yes
		No
	Metamaterial	Yes
		No
200	Nomex	Yes
		No
	Metamaterial	Yes
		No
300	Nomex	Yes
		No
	Metamaterial	Yes
		No

with a plain model and with more models exploiting different acoustic solutions. An overview of the analysis is shown in Tab. 4.8.

4.7.2 Components

Several components are used to build the acoustic model in Actran. To each component a material, one or more domains and some characteristics are associated. The key figures relating to components are reported below:

- finite fluid, it is the component to model a finite acoustic medium, each node carries a single degree of freedom: the acoustic pressure. It is defined by the material and the domain. The air cavities and the air cloak are modeled by this component;
- solid, this component is used to model solid parts and each node carries three degrees of freedom: the displacement components. Material, domain and power evaluation are defined. Solid is used to define the trim panel core;
- thin shell, it models transverse thin elements, defining six degrees of freedom for each node: displacement and rotation components. Material, domain, thickness and reference direction must be defined within other not mandatory parameters as power evaluation. The fuselage, the trim panel plates, the floor and the overheads are modeled as thin shell;
- beam, it is used to model equivalent stiffeners and is based on six degrees of freedom for each node: displacement and rotation components. This component is defined by material, domain and reference direction and by not mandatory parameters as power evaluation. Stringers, spars and bridge beams are modeled by this component;
- rigid body, it defines rigid body elements between one or several degrees of freedom of a given independent node to the same degree(s) of freedom of the related dependent nodes. The number of degrees of freedom could be selected from the acoustic pressure, the structural displacement and structural rotation components. The domain must be selected and the creation or suppression of the rotational degrees of freedom could be chosen. Rigid bodies are used to model the trim panel supports;

- coupling surface, it used to define interfaces between a solid component and a fluid component (weak coupling) but also between two fluid components or two solid components (strong coupling). The domain must be chosen;

- interface, it handles incompatible meshes (see section 3.2.5). For every interface the two coupling surface must be selected. A projection tolerance could be chosen. For the interfaces projections used in this model see section 4.7.3.

In Tab. 4.9[2] the components, except for coupling surfaces and interfaces, used in the analysis, are reported with their domain and eventually their material and degrees of freedom.

Table 4.9: Components used in the analysis with their characteristics.

Finite fluid					
Name	**ID**	**Domain**	**Material**		
Finite_fluid	2	All acoustic cavities	Air 11		
Air_cloak	64	External air cloak	Air 11		
Solid					
Name	**ID**	**Domain**	**Material**		
Trim_panel_core_solid	46	Trim_panel_core	Nomex_v2 51		
Thin shell					
Name	**ID**	**Domain**	**Material**	**Thickness [m]**	**Reference direction**
Windows	4	Bdf_shell4_windows	Window_mat 65	LAMINATE	[1, 0, 0]
Floor	5	Bdf_shell5_floor	Mat1_2 6	0.01016	-
Fuselage_top	17	Bdfshell17_ext_top_fuselage	Mat8_4 22	0.001056	-
Fuselage_bot	18	Bdfshell18_ext_bot_fuselage	Mat8_5 23	0.00132	-
Windows_belt	19	Bdfshell19_sorrounding_windows_panel, erased_window	Mat8_7 24	0.003168	-
Lateral_panel1	20	Bdfshell20_lateral_panels	Mat8_8 25	0.001848	-
Lateral_panel2	21	Bdfshell21_lateral_panels	Mat8_9 9	0.00264	-
Trim_panel_bottom_composite	47	Trim_panel_bottom_composite	Fiberglass_composite_2layers 61	LAMINATE	[0, 0, -1]
Trim_panel_top_composite	48	Trim_panel_top_composite	Fiberglass_composite_2layers 61	LAMINATE	[0, 0, 1]
Overhead	60	Overhead	PVC 64	0.01	-
Trim_false_windows	68	Windows_on_trim_panel2000156	False 70	0.003	-
Beam					
Name	**ID**	**Domain**	**Material**	**Reference direction**	
PBar_1	1	BdfBar1	Beam 35	[1, 0, 0]	
PBeam_6	6	BdfBeam6	Beam 41	[1, 0, 0]	
PBeam_7	7	BdfBeam7	Beam 42	[1, 0, 0]	
PBeam_8	8	BdfBeam8	Beam 43	[1, 0, 0]	
PBeam_9	9	BdfBeam9	Mat1_18 44	[1, 0, 0]	
PBeam_10	10	BdfBeam10	Beam 45	[1, 0, 0]	
PBar_26	26	BdfBar26	Beam 36	[1, 0, 0]	
PBar_27	27	BdfBar27	Beam 37	[1, 0, 0]	
PBar_28	28	BdfBar28	Beam 38	[1, 0, 0]	
PBar_30	30	BdfBar30	Beam 39	[1, 0, 0]	
PBar31	31	BdfBar31	Beam 40	[1, 0, 0]	
Rigid body					
Name	**ID**	**Domain**	**Dof**		**Force rotation dofs**
RBE2	32	BdfRigidBody1023456	Displacements in y and z, rotations in x, y and z		Activated
RBE2	33	BdfRigidBody1123456	Displacements in x, y and z, rotations in x, y and z		Activated

4.7.3 Interfaces

In this model interfaces (and coupling surfaces) are created to link a thin shell with an air cavity and eventually to link two thin shells with different meshes. The skin of the air cavity is built to define the coupling surface. Furthermore a small gap is left between the coupling surfaces to avoid error linked with quasi-incompatible meshes. The interfaces and coupling surfaces are reported in Tab. 4.10. For some interfaces a gap and a plane tolerance are set, otherwise a default plane and gap tolerance of 0.01 m is taken. Actran, to create an interface, localizes points to project, thanks to the tolerance.

[2]For a windowless configuration there are not windows both on the fuselage and on the trim panel, the windows belt panel is not pierced and the bar component, which defines the windows frames, is eliminated.

Table 4.10: Interfaces and coupling surfaces.

Interface ID	Coupling surface 1	ID	Coupling surface 2	ID	Gap tolerance	Plane tolerance	Points not localized
2	Floor	44	Bottom cavity	3	[0.002, 0.02, 0.2]	[0.002, 0.02, 0.2]	0.48 %
3	Bottom fuselage	5	Bottom cavity	4	[0.002, 0.02, 0.2]	[0.002, 0.02, 0.2]	2.49 %
5	Fuselage (with bottom panels)	14	Air gap	8	[0.002, 0.02, 0.2]	[0.002, 0.02, 0.2]	0.45 %
6	Trim panel	31	Air gap	9	[0.002, 0.02, 0.2]	[0.002, 0.02, 0.2]	0 %
9	Bottom cavity	3	Air gap	23	[0.002, 0.02, 0.2]	[0.002, 0.02, 0.2]	93.10 %
12	Overheads	42	Overhead air cavity	43	-	-	44.91 %
13	Trim panel, overheads and floor	45	Cabin air cavity	46	[0.002, 0.02, 0.2]	[0.002, 0.02, 0.2]	10.09 %
14	Fuselage	51	Air cloak	52	-	-	1.93 %

4.7.4 Boundary conditions

Boundary conditions define the model inside the differential equations 3.1. Four boundary conditions are created to describe the fuselage displacements, the pressure loads and the seats impedance.

The displacement of the fuselage is defined by a displacement boundary condition and by a rotation condition. The displacement represents a constraint because the imposed displacements are zero. Equally the allowed rotation is zero. These two boundary conditions are applied to a domain composed by 0D elements. This domain is directly linked to the fuselage and through this domain, these boundary conditions represent the constraint on the physical fuselage, Fig. 4.19(a).

The pressure loads, described in section 4.2, are applied to the fuselage through a virtual air cloak with a pressure boundary condition, Fig. 4.19(b). This virtual cloak is modeled as a fluid (3D elements) component with a thickness of 1 mm (two nodes on the thickness). On this virtual cloak the loads are applied as a one dimensional field where pressure, as a complex number, is defined on the nodes. For the internal nodes the propellers loads are applied, while for the external node a zero pressure is defined, Fig. 4.17(a). To load the field, the following command has been written directly in the analysis file (`.edat`):

```
BEGIN FIELD 1
FIELD_NDIM 1  Field dimension
DEFAULT_VALUE {0, 0}  For external nodes
9656 Total number of internal nodes
490342 { 1.45597050e-02, 1.33434480e-02} Node ID {Real parts, Imaginary parts} in Pa
.
.
.
499997 { 4.06289350e-01, -5.20316710e-01}
END FIELD 1
```

The physical and virtual fuselages are linked through an interface where the first coupling surface is the physical fuselage (bottom and top fuselage, lateral panels, windows belt, windows and removed windows) and the second it is the virtual air cloak surface. During the meshing process, particularly running the merge nodes function, 136 nodes are eliminated as duplicates (one for every circle that composes the virtual air cloak), and so, also the corresponding loads are eliminated, so 9656 nodes remain. There are two differences between the virtual and real fuselage, besides the nodes: the size and the reference system. The different sizes lead to a misalignment between the two fuselage on their longitudinal axes, Fig. 4.17(b), but no action are undertaken because this misalignment concerns less than the 10% of the fuselage length, about the 6%. The

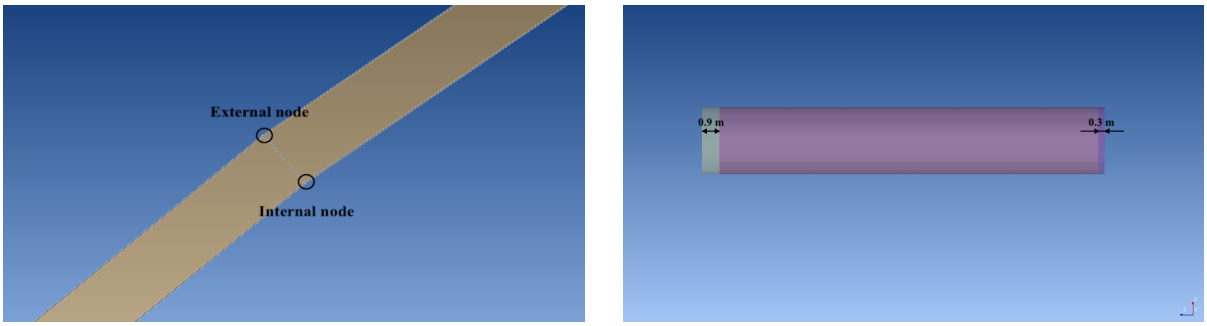

(a) (b)

Figure 4.17: (a) Internal and external nodes on which the pressure filed is applied. (b) Misalignment between the air cloak and the physical fuselage.

reference system of the loads has been changed to be coherent with the system of the physical fuselage, the two different system are shown in Fig. 4.18. The centre of the two system is the same, at the bow of the aircraft. A review of the manipulations made on the pressure loads is shown in Tab. 4.11.

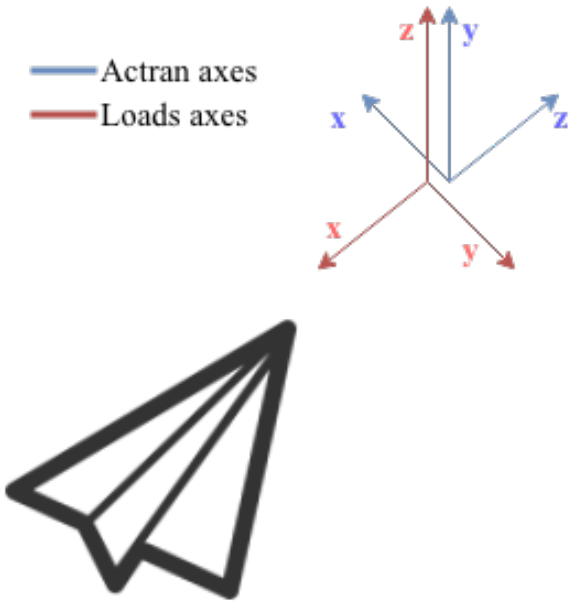

Figure 4.18: The two different reference systems: in Actran (blue) and for pressure loads (red).

Table 4.11: Review of the manipulations on the pressure loads to import them in Actran.

	"Old" loads	**"New" loads**
Number of points (nodes)	9792	9656
Reference system	x, y, z	-y, z, -x
First coordinate	-1.725E+00 3.016E-07 -2.650E+01	6.000E+00 1.725E+00 0.000E+00
Second coordinate	-1.718E+00 -1.525E-01 -2.650E+01	6.000E+00 1.725E+00 1.525E+00
Last coordinate	-1.718E+00 1.525E-01 -6.000E+00	2.650E+01 1.725E+00 3.016E-07

In the end, to define the seats impedance, in absence of a defined porous material, a normalized

impedance condition has been applied. The normalized impedance $\overline{Z_{norm}}$ is egual to:

$$\overline{Z_{norm}} = \frac{p}{\bar{v}_n \rho c} \tag{4.1}$$

in which p is the pressure, $\bar{v}_n$ normal surface velocity, ρ and c the density and the sound speed of the medium respectively. In Actran the medium (air) is defined by the density and the sound speed and the not normalized impedance as a function of the frequency in a table, Fig. 4.20. This boundary condition is applied to the seats shell (2D elements), Fig. 4.19(a). The seats volume is removed from the passengers cabin air cavity.

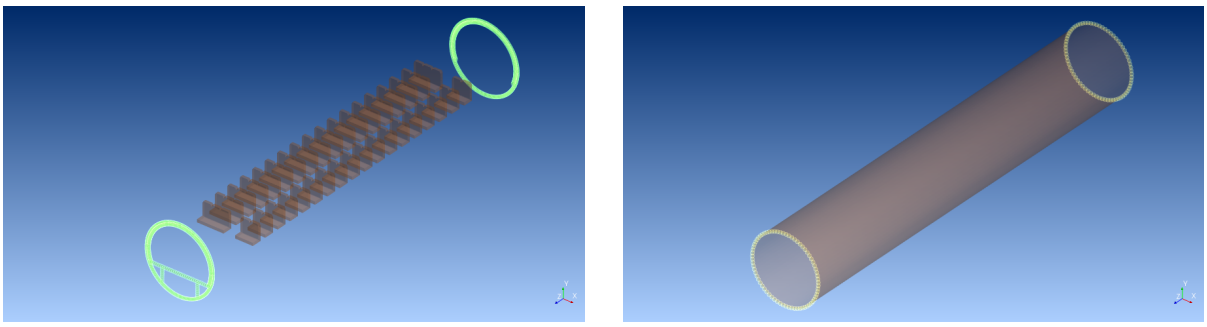

(a) **(b)**

Figure 4.19: (a) The domains on which the displacement, rotation boundary condition for physical fuselage (green) and normalized impedance boundary condition (brown) are applied. (b) The domain (brown) on which the pressure boundary condition is applied.

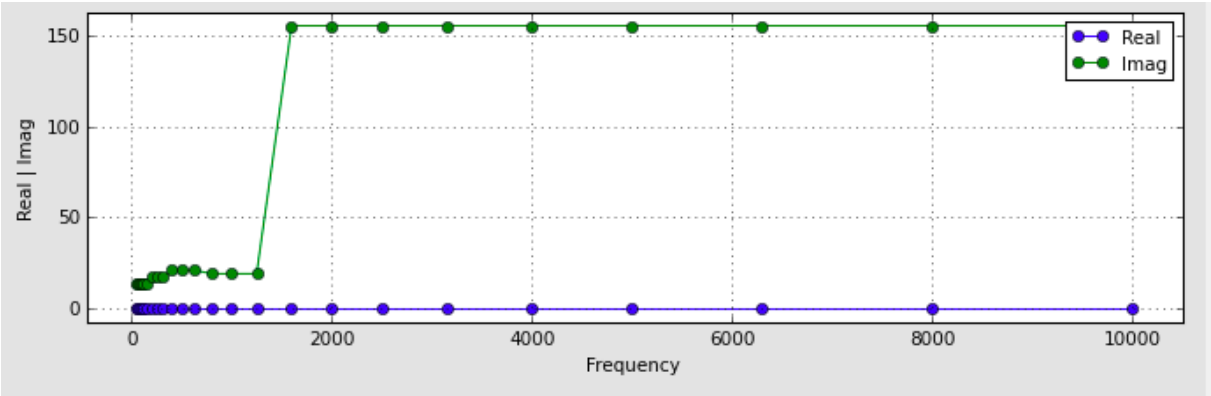

Figure 4.20: The not-normalized impedance as a function of frequency.

4.7.5 Solver

The `MUMPS` has been chosen to find the solution of direct frequency response analysis. This solver is based on LU decomposition of the following algebraic system:

$$\boldsymbol{Z}x = \boldsymbol{B} \tag{4.2}$$

and it assembles $\boldsymbol{Z}$ matrix and then it factorizes its to find the lower $\boldsymbol{L}$ and upper $\boldsymbol{U}$ matrix:

$$\boldsymbol{Z} = \boldsymbol{LU} \ . \tag{4.3}$$

This method is called sequential approach and it includes, apart from `MUMPS`, `SPARSE`, `CG_ILU` and `PARDISO` solvers. `MUMPS` could be also based on frequency and azimuthal order parallelism computation, domain parallelism computation and matrix parallelism computation. `MUMPS` (multifrontal massively parallel solver) is developed by [43] and is used with a sub-solver, `SCALAPACK`, to assemble interfaces.

This solver has been preferred to `KRYLOV` solver because this last solver works better with materials and boundary conditions that have a simple relation with the frequency. It is not the case of metamaterials or impedance boundary conditions.

4.7.6 Output requests

Sound pressure is calculated in seven sets of points (output FRF) and saved in a `plt` file. The first five sets represent the heads position of seated passenger, at a height of 1.20 m from the floor and disposed above the seats. The sixth set is composed by three points on the floor. The last set represents the heads position of standing passengers, at a height of 1.70 m from the floor and disposed along the cabin corridor. The characteristics of these sets are summarized in Tab. 4.12. Furthermore a field map at 1.20 m from the floor inside the cabin (same heights of the first

Table 4.12: Field points parameters.

Field points ID	Number of points	Position	Height from the floor [m]
1	18	Seats I	1.20
2	18	Seats II	1.20
3	18	Seats III	1.20
4	18	Seats IV	1.20
5	18	Seats V	1.20
20	3	At -10 m, -15 m and -20 m in the cabin	0.0
24	19	In the corridor from -9.58 m to -24.81 m	1.70

five sets) is created to visualize the pressure map. A second field map is created on the coupling surface between the air cloak and the fuselage to visualize the pressure loads.

The output requests inside the passengers cabin (field map and field points) are shown in Fig. 4.21.

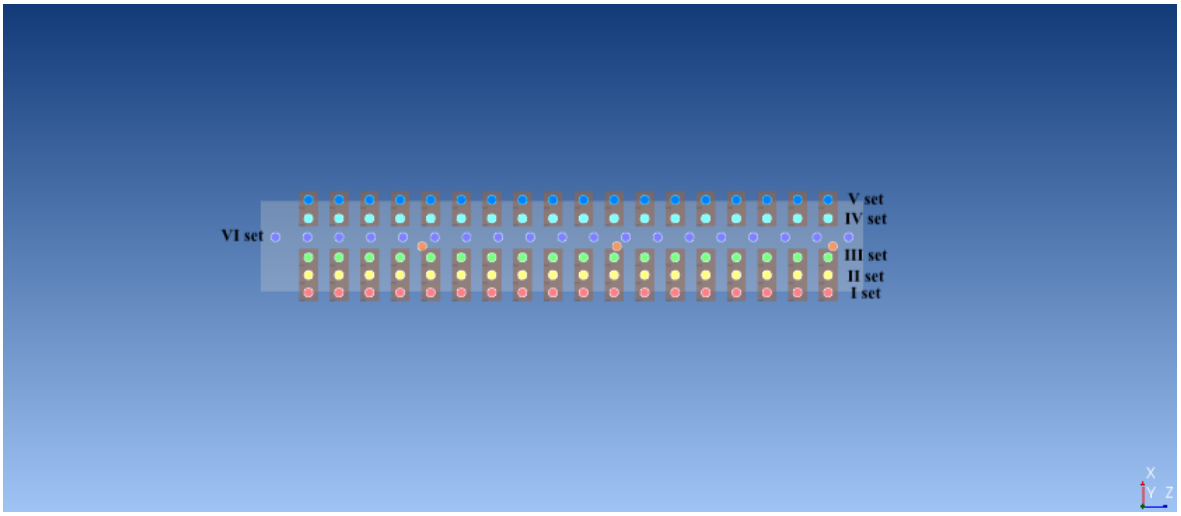

Figure 4.21: Field points sets and field map for output requests.

4.8 Modal extraction

Model extraction is run in Actran on the fuselage structure without air cavities, seats and external loads for plain model (trim panel in Nomex and there are windows). The obtained modes result very complex because of the presence of the bars between the fuselage panels and the trim panel. The first mode (displacements and rotations) for fuselage panels is reported in Fig. 4.22 and in Fig. 4.23 at frequency of 0.208 Hz.

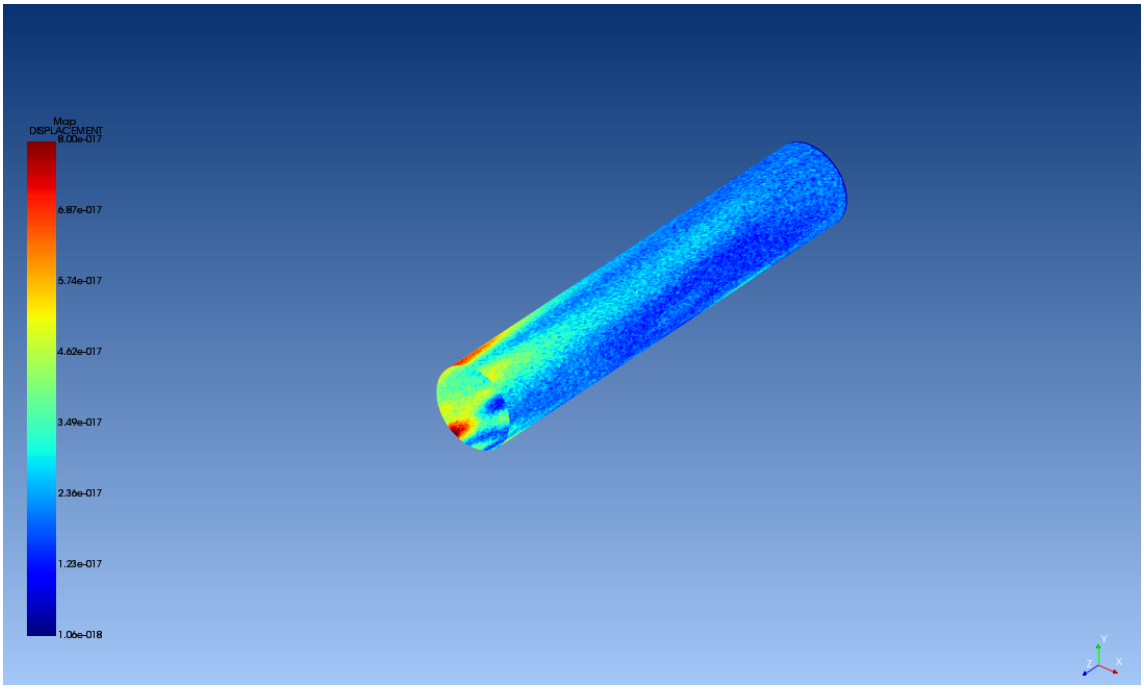

(a)

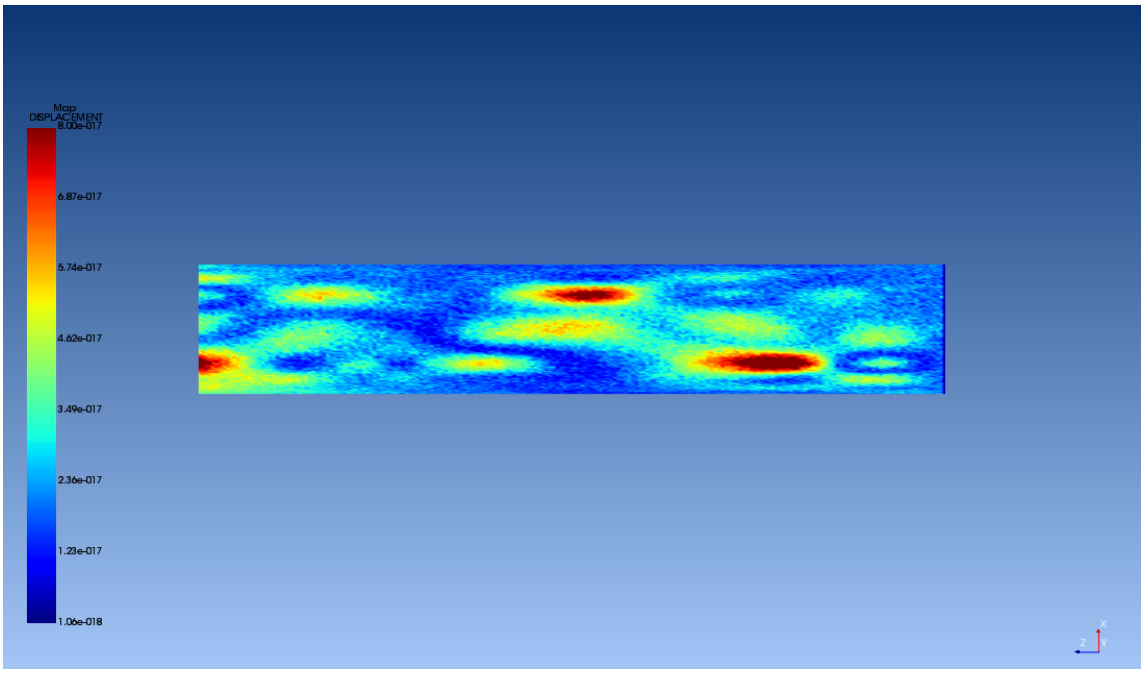

(b)

Figure 4.22: First mode displacements [m] at 0.208 Hz. (a) Perspective view. (b) View from above.

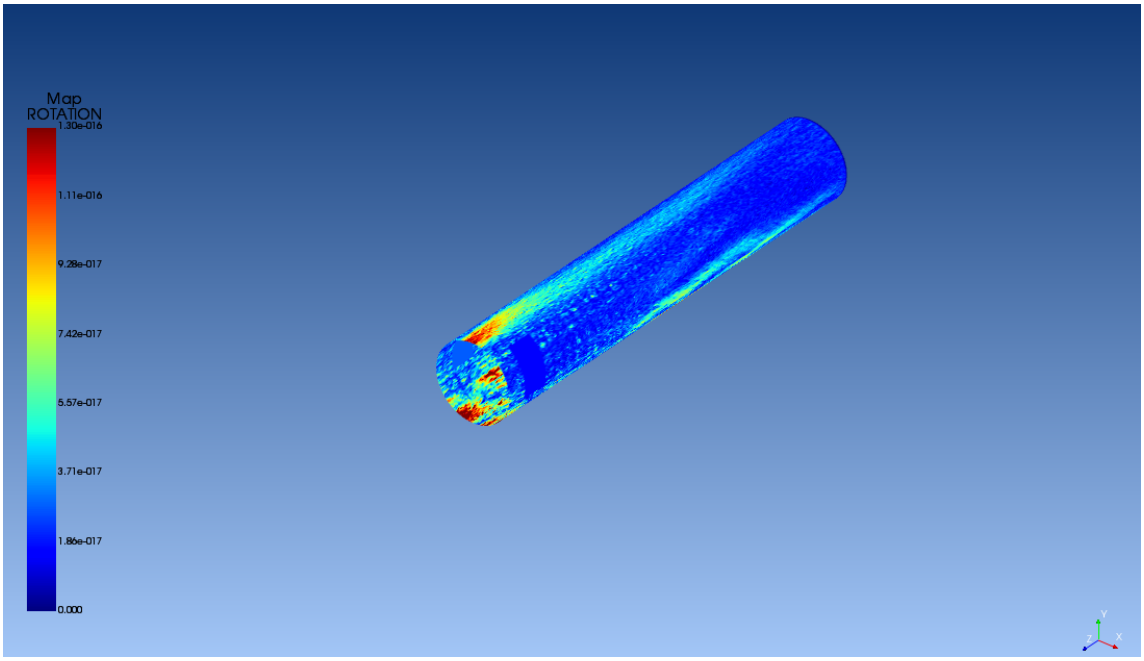

(a)

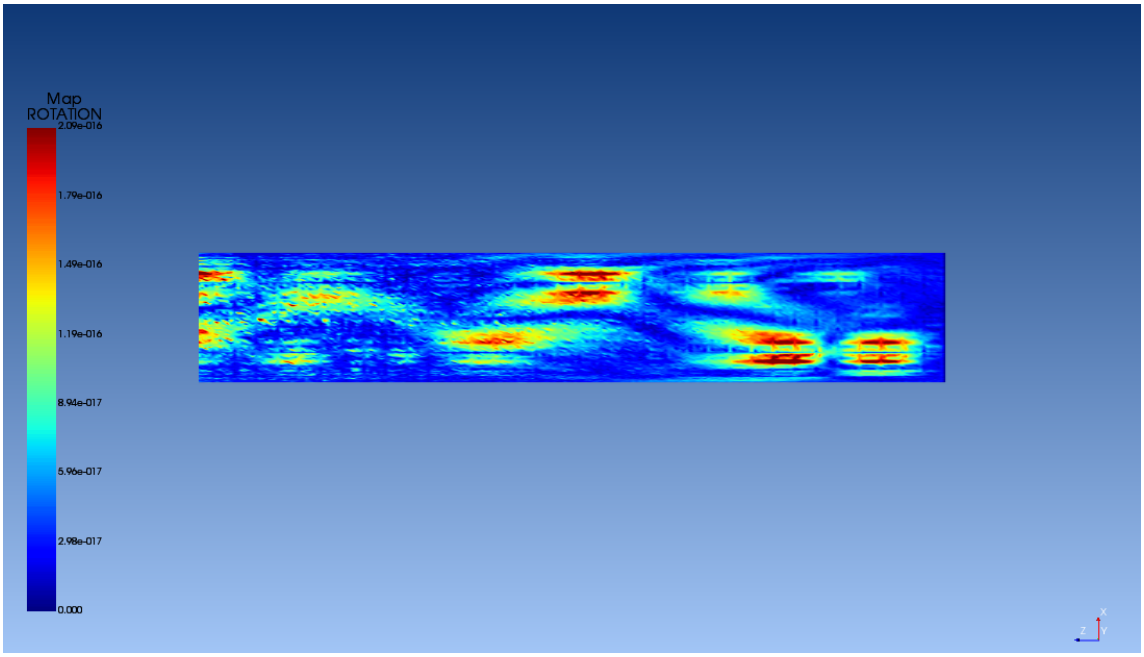

(b)

Figure 4.23: First mode rotations [°] at 0.208 Hz. (a) Perspective view. (b) View from above.

Chapter 5

Results

5.1 Overview of results

The results are calculated in terms of SPL (sound pressure level) and of OASPL (overall sound pressure level) in dBA, these parameters are been already explained in section 1.4.1. The weights of dBA for 100 Hz, 200 Hz and 300 Hz are respectively -19.1451, -10.8472 and -7.0546. The SPL is calculated as mean on the first five sets of FRF points (microphones), so as a mean of sound pressure felt by seated passengers (1.20 m from the floor). Then the OASPL is the weighted mean of SPL on frequency. The results refer to the twelve analysis made, Tab. 4.8. Pressure maps are obtained at 1.20 m from the floor. As expected, independently from the acoustic solution, the SPL decrease with frequency. Indeed the pressure loads magnitude decreases from 100 Hz to 300 Hz. Finally for higher frequencies (200 Hz and 300 Hz) it is possible to define a more noisy region near the propellers.

5.2 Trim panel in metamaterial

The OASPL on the three frequencies is equal to 87.7555 dBA for a trim panel made of Nomex, it is equal to 81.6033 dBA for a trim panel made of metamaterial. The OASPL, for a windowless aircraft, on the three frequencies is equal to 87.8538 dBA for a trim panel made of Nomex, it is equal to 81.7751 dBA for a trim panel made of metamaterial. Results (SPL in dBA) for each tonal frequency are reported in Tab. 5.1 and compared in Fig. 5.1. The trim panel made of metamaterial is acoustically more efficient than a trim panel made of composite (Nomex). In fact there is a mean reduction of 6.1522 dBA, equal to the 7.01% of total OASPL. The sound pressure it is almost halved, it passes from 0.488 Pa to 0.241 Pa. For a windowless configuration, the effect of the metamaterial is similar to a traditional aircraft. There is a reduction of the OASPL of 6.0787 dBA, equal to 6.92% (pressure decrease from 0.494 Pa to 0.245) refer to the windowless aircraft with trim panel in Nomex, while the reduction is equal to 5.9804 dBA (6.81%) referring to a traditional aircraft with trim panel in Nomex .

5.3 Windowless configuration

The removal of windows does not show a general reduction or increase of OASPL. In fact the OASPL increases for trim panel of Nomex of 0.0983 dBA, almost the 0.11%, while for trim panel made of metamaterial almost of 0.21% (0.1718 dBA). In terms of acoustic pressure in Pa, a traditional aircraft with trim panel in Nomex has a pressure of 0.488 Pa while one exploiting a windowless configuration has a pressure of 0.494 Pa (and from 0.241 to 0.245 for a trim panel made in metamaterial). Furthermore the noise reduction (or increase) due to the absence of windows strongly depends on frequency with a non-monotone behavior, this could be see in transmission loss of windows materials (tempered glass and plexiglass) and of fuselage material (Fig. 4.9), where for 100 Hz and 300 Hz fuselage is a better sound deflector than windows, while for 200 Hz there is the opposite behavior. The transmission losses of these two materials strongly depend on frequency.

Table 5.1: Results for each tonal frequency.

Frequency [Hz]	Windows	Trim panel material	Mean SPL [dBA] (in the cabin)	Field map [dBA] (1.20 m from the floor)	Pressure load [Pa]
100	Yes	Nomex	96.1002	Fig. 5.2(a)	Fig. 4.5(a) and (b)
		Metamaterial	91.1787	Fig. 5.2(b)	
	No	Nomex	95.1558	Fig. 5.3(a)	
		Metamaterial	90.6576	Fig. 5.3(b)	
200	Yes	Nomex	87.0665	Fig. 5.4(a)	Fig. 4.6(a) and (b)
		Metamaterial	80.1956	Fig. 5.4(b)	
	No	Nomex	88.5334	Fig. 5.5(a)	
		Metamaterial	81.8591	Fig. 5.5(b)	
300	Yes	Nomex	80.7887	Fig. 5.6(a)	Fig. 4.7(a) and (b)
		Metamaterial	74.8432	Fig. 5.6(b)	
	No	Nomex	79.1924	Fig. 5.7(a)	
		Metamaterial	72.7245	Fig. 5.7(b)	

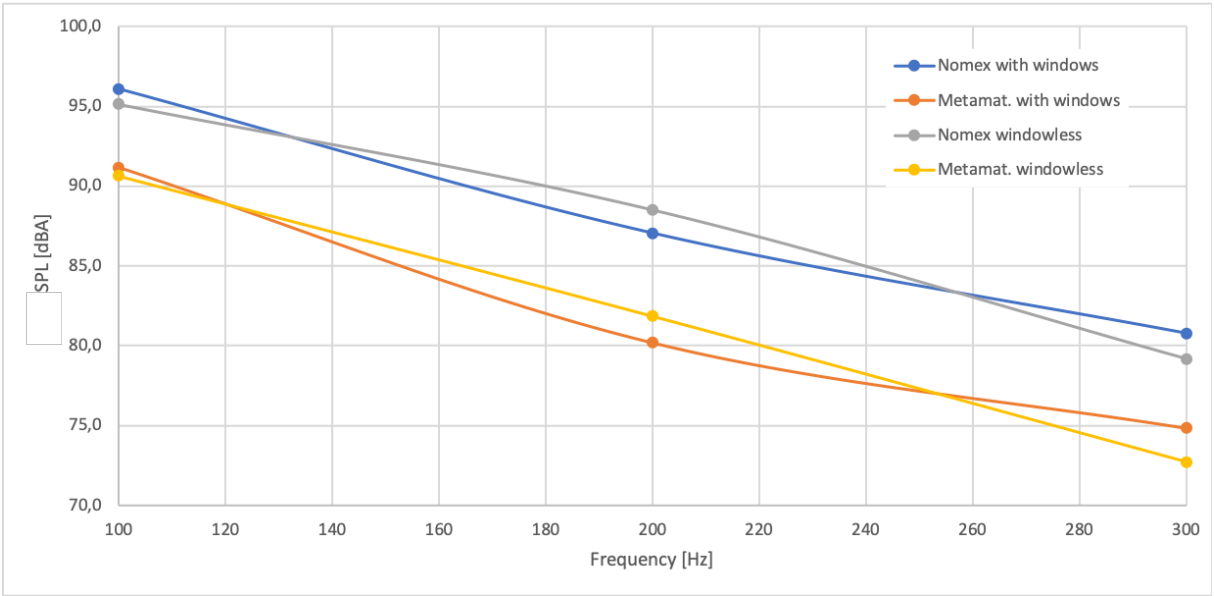

Figure 5.1: The results, in terms of SPL [dBA] for each tonal frequency [Hz], are compared.

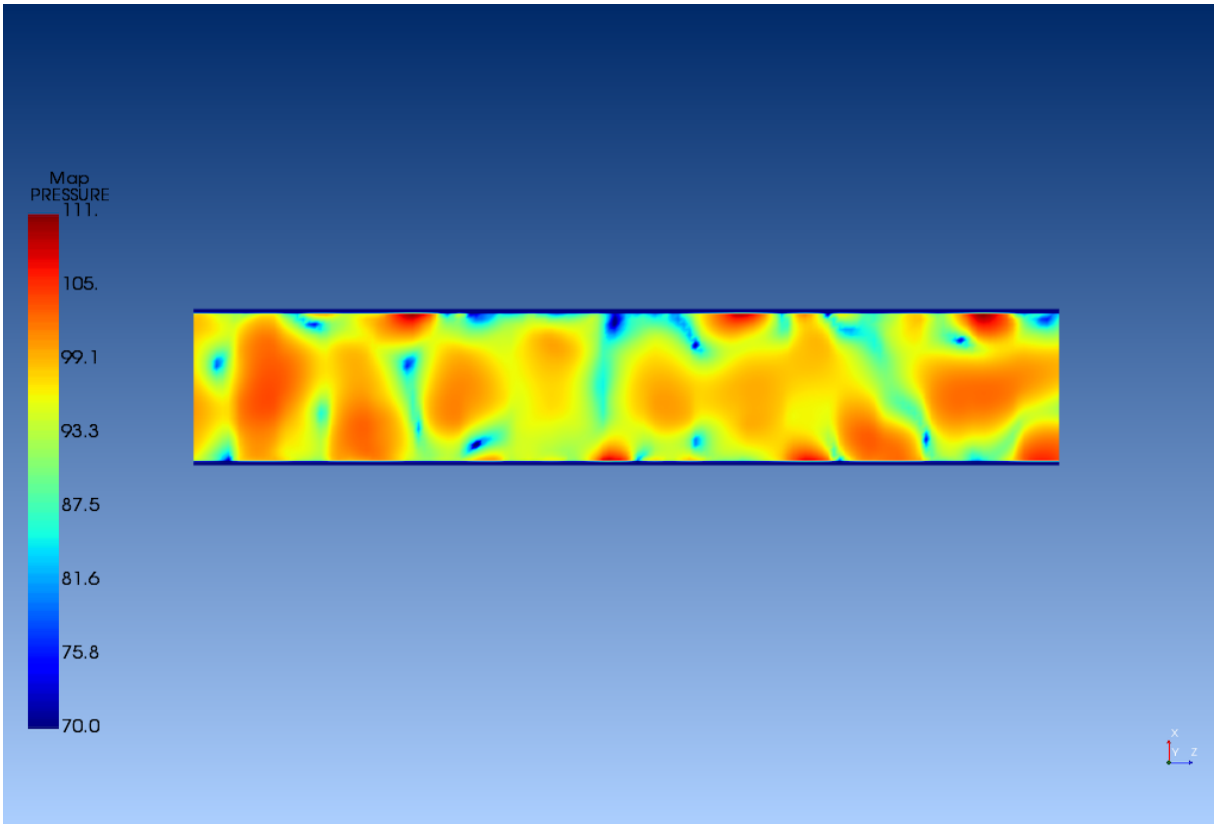

(a)

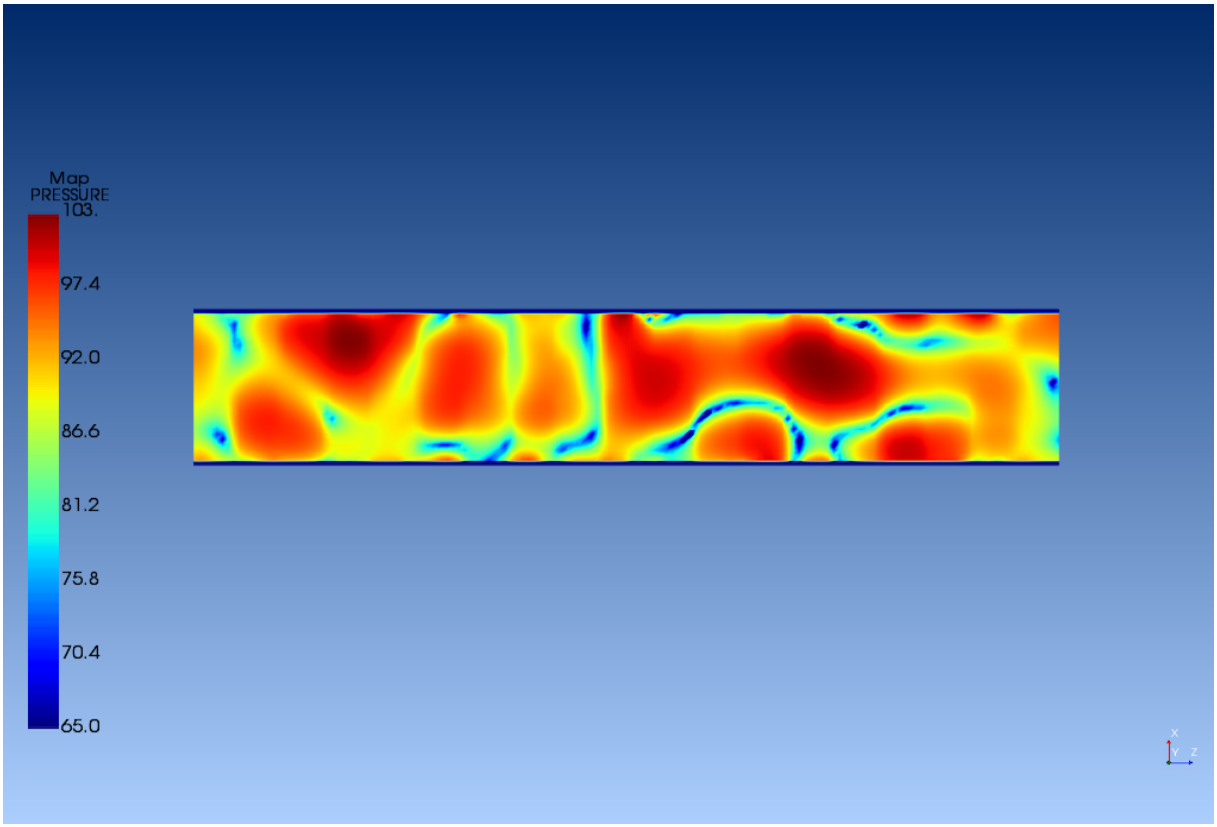

(b)

Figure 5.2: SPL maps at 100 Hz in dBA for a configuration with windows. (a) Nomex. (b) Metamaterial.

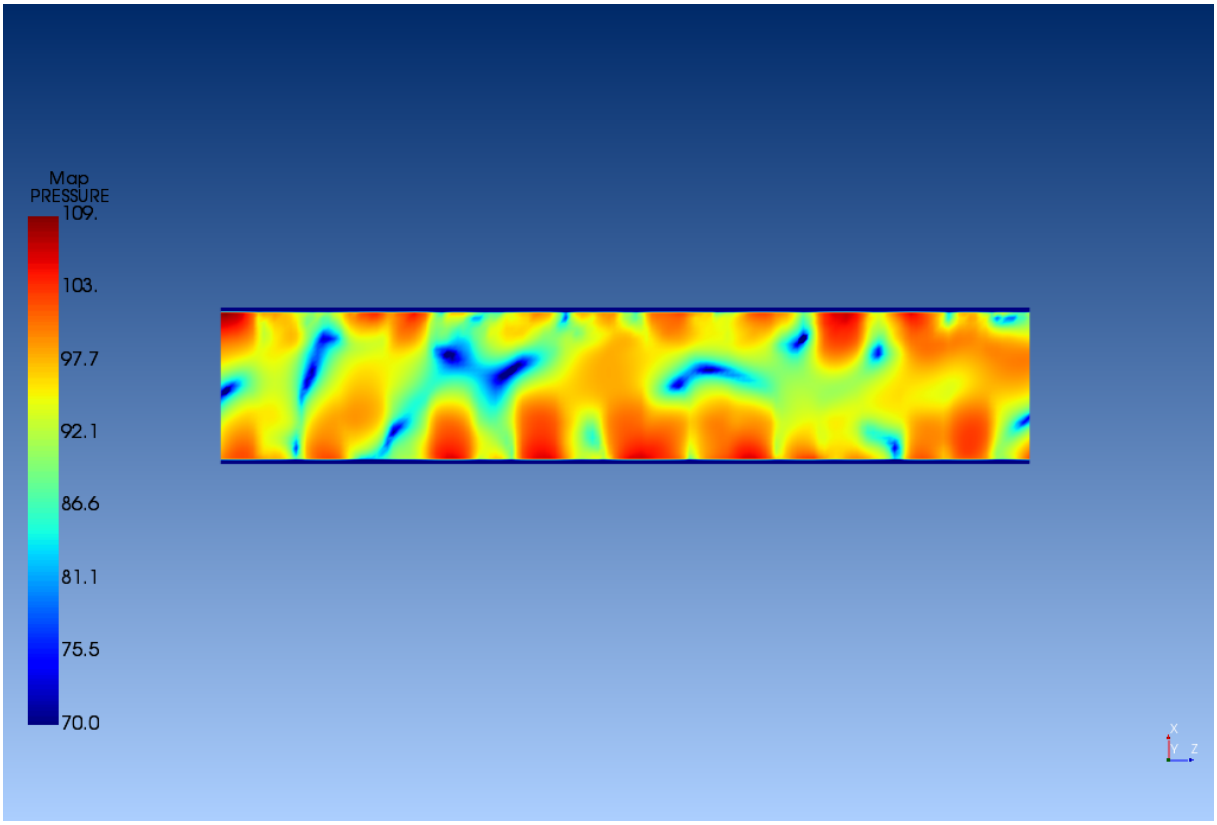

(a)

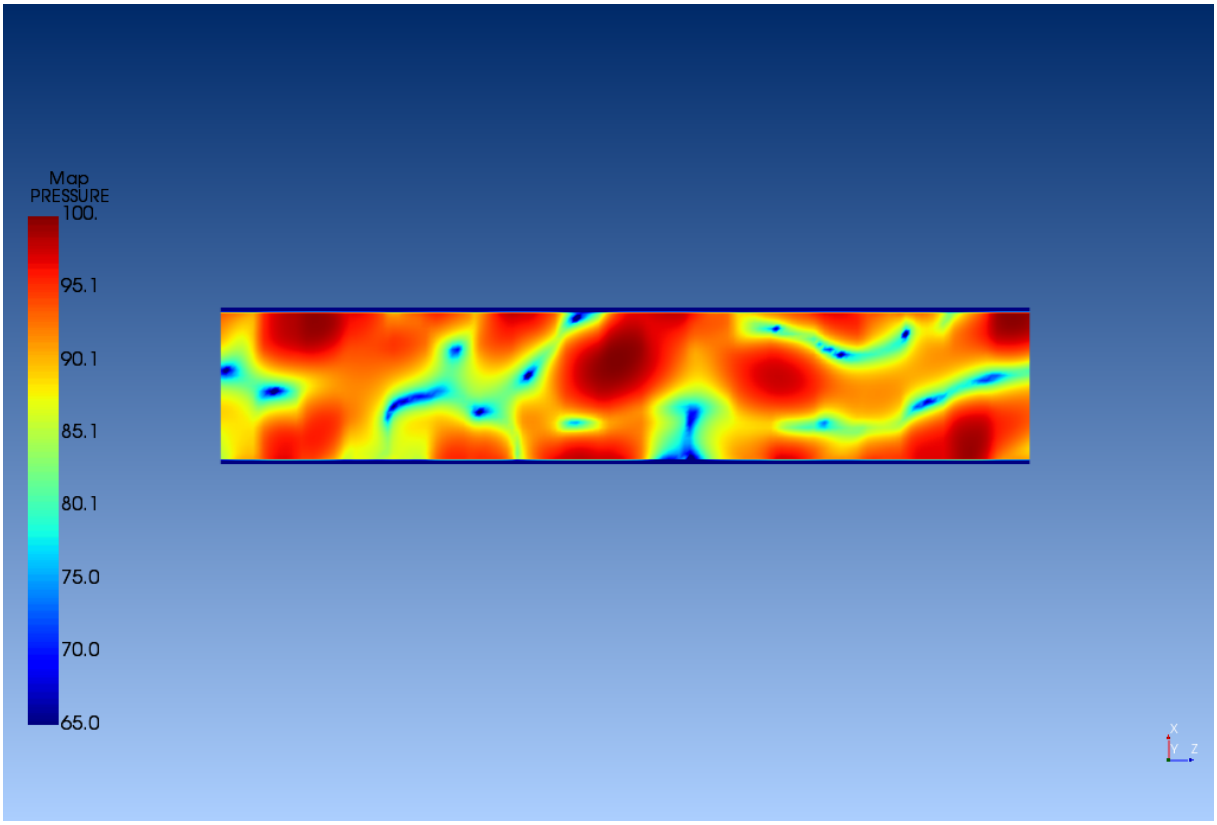

(b)

Figure 5.3: SPL maps at 100 Hz in dBA for a windowless configuration. (a) Nomex. (b) Metamaterial.

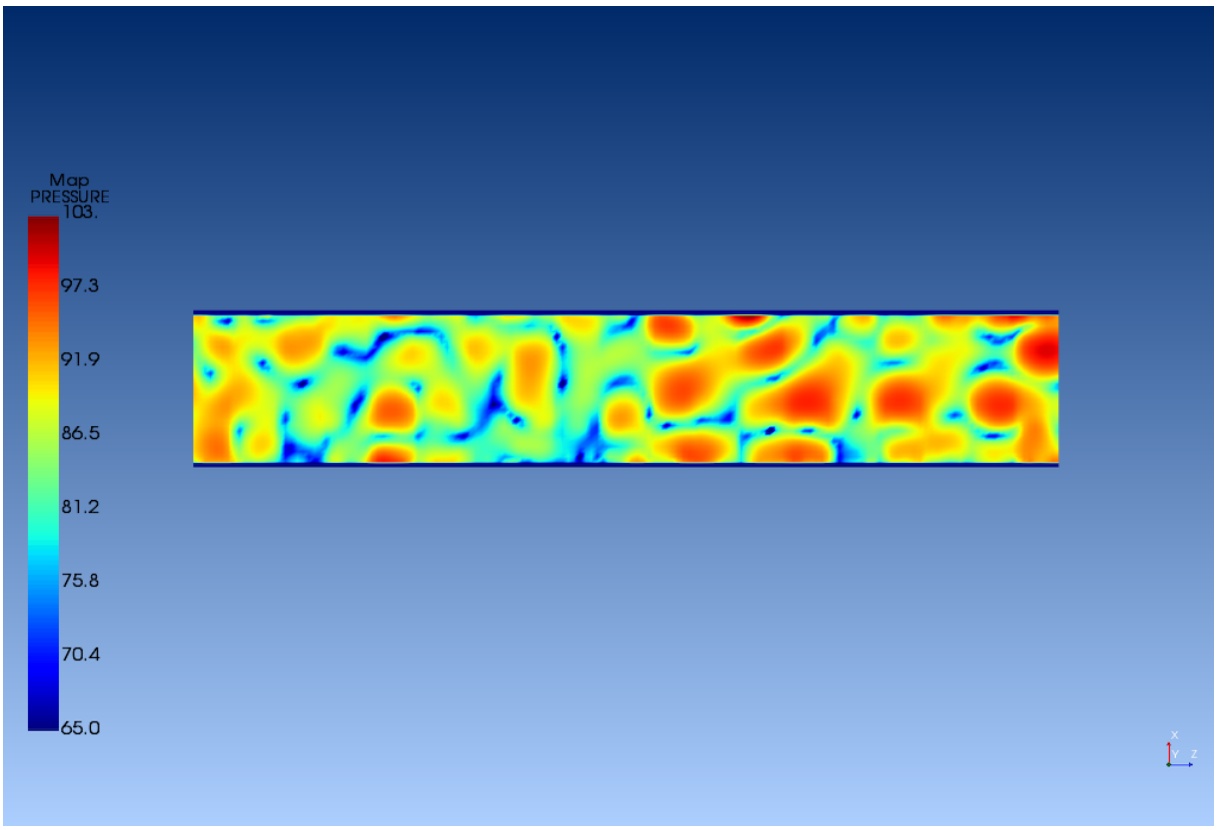

(a)

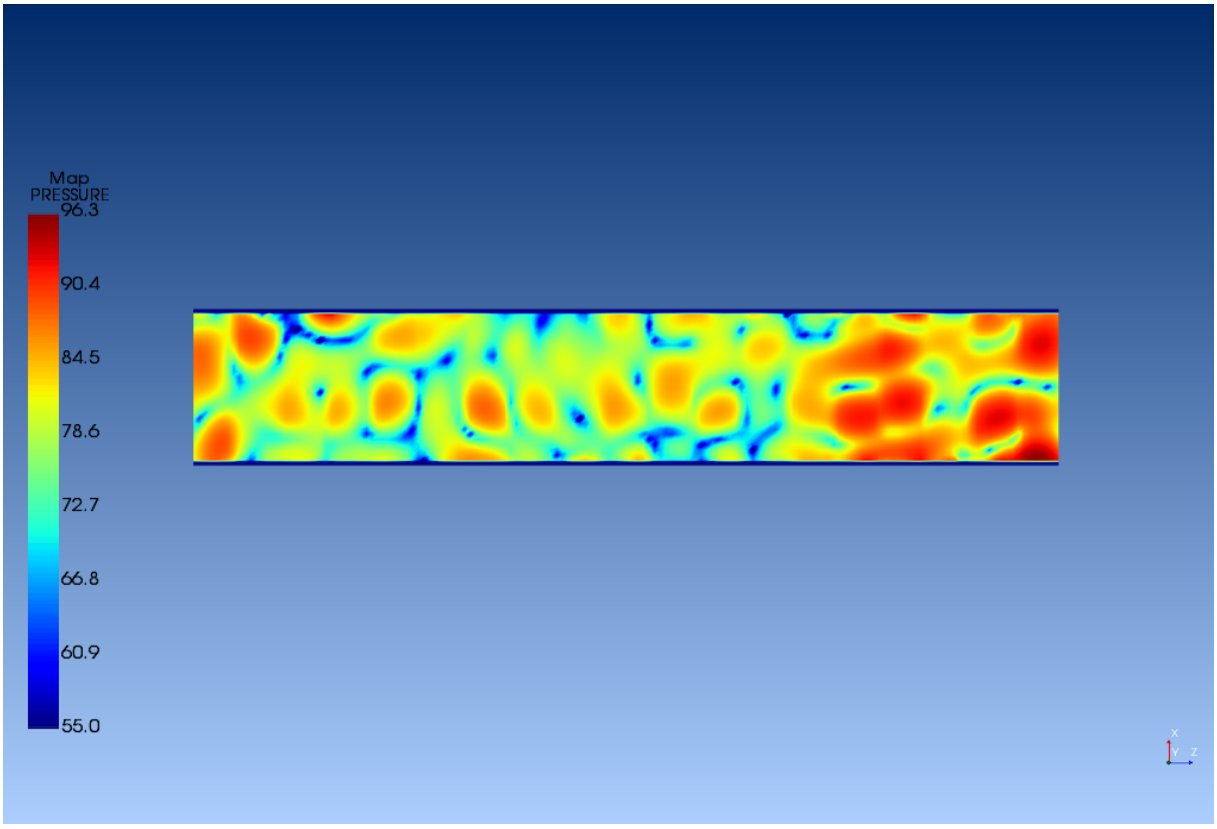

(b)

Figure 5.4: SPL maps at 200 Hz in dBA for a configuration with windows. (a) Nomex. (b) Metamaterial.

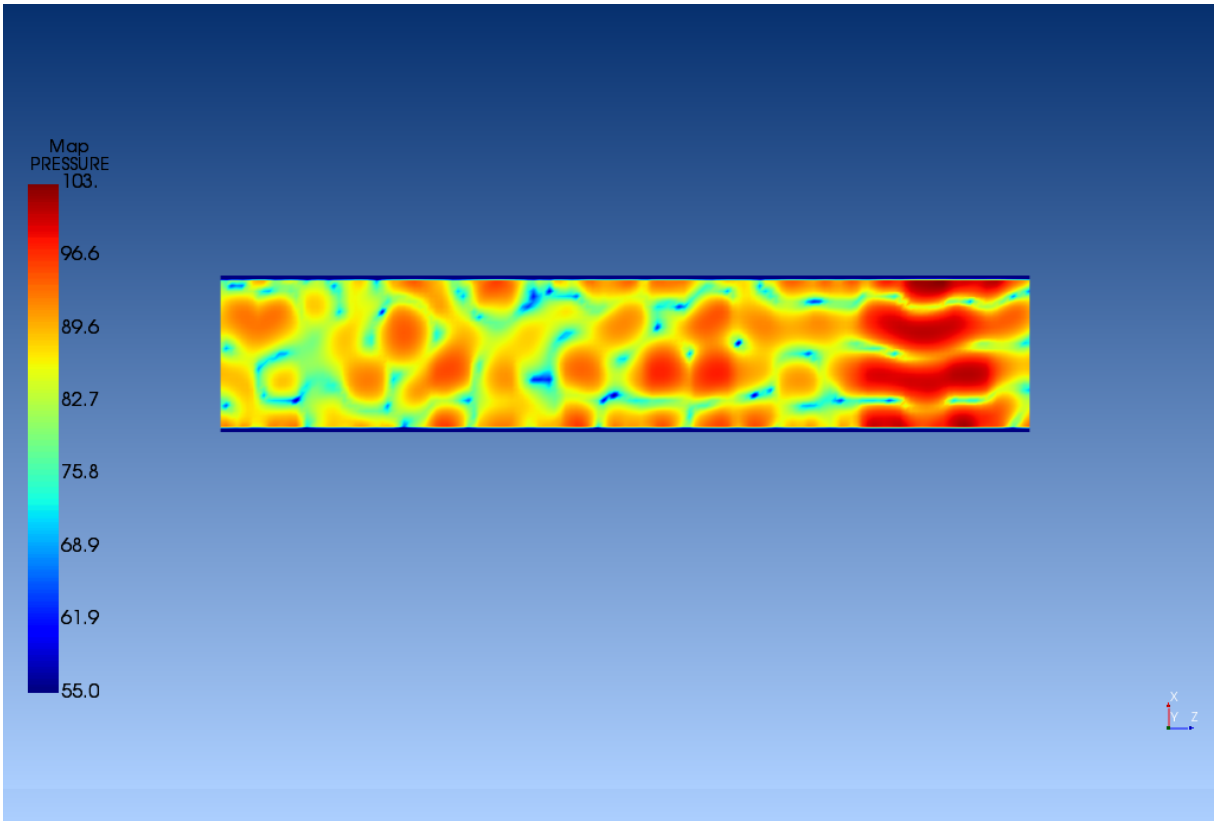

(a)

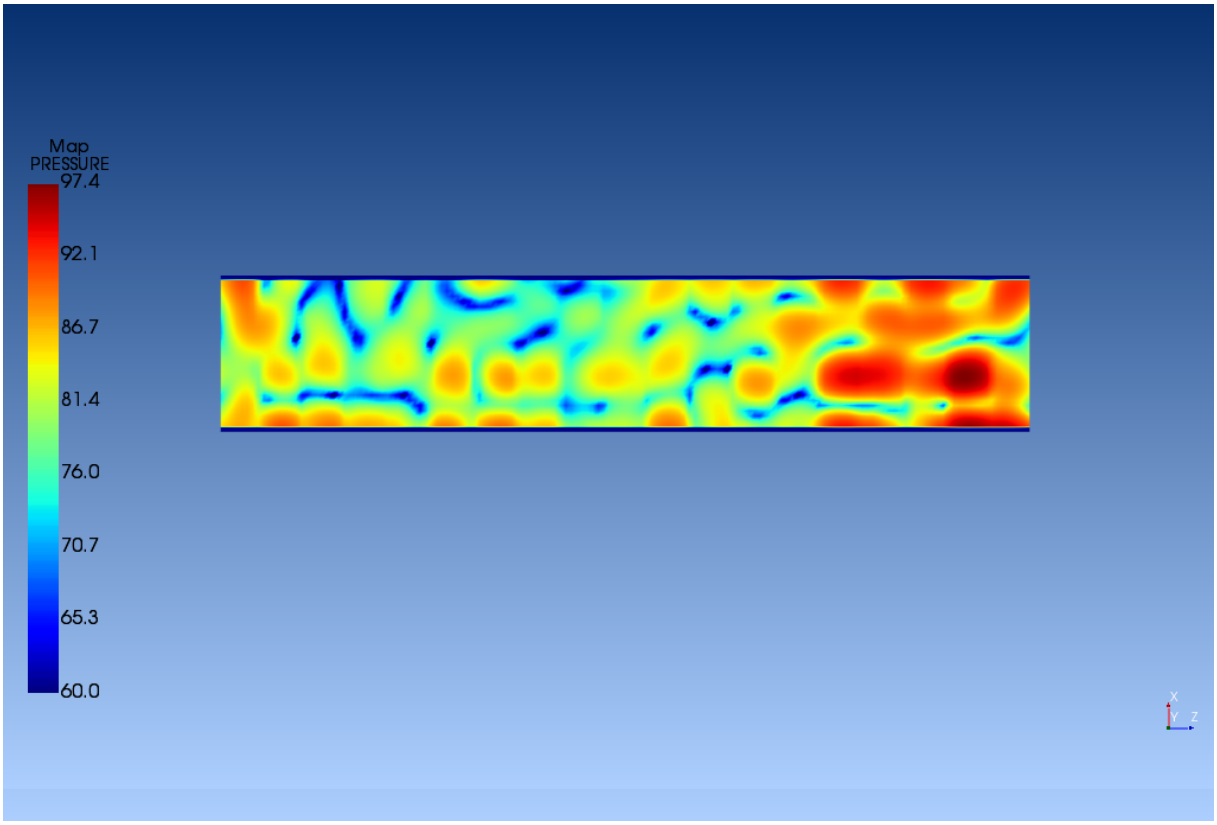

(b)

Figure 5.5: SPL maps at 200 Hz in dBA for a windowless configuration. (a) Nomex. (b) Metamaterial.

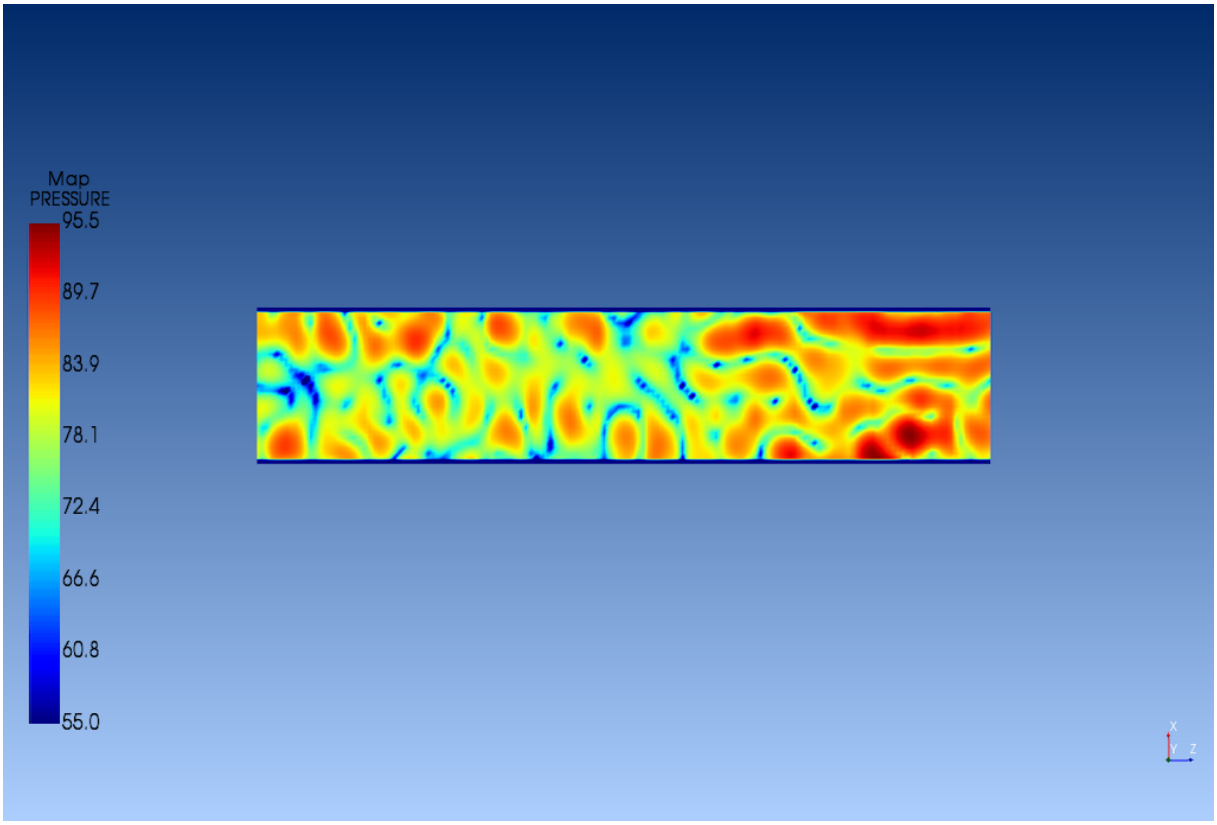

(a)

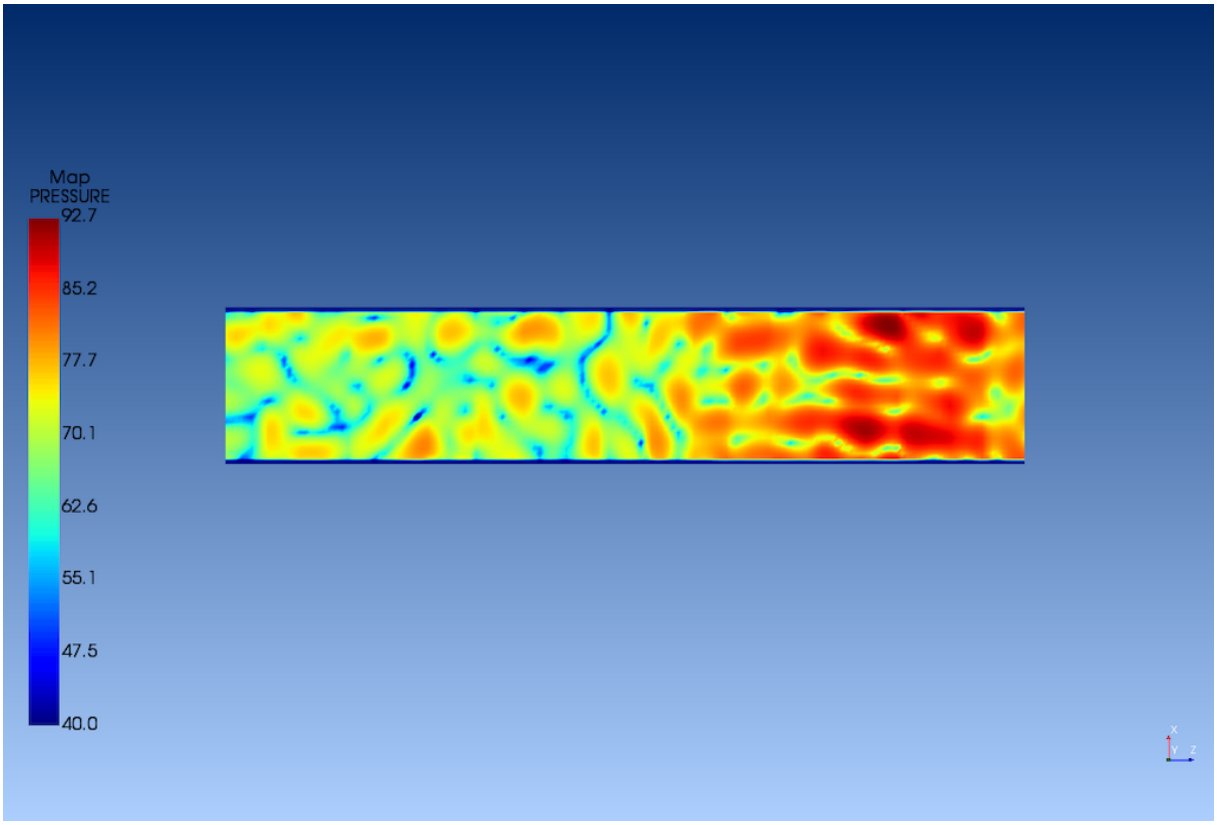

(b)

Figure 5.6: SPL maps at 300 Hz in dBA for a configuration with windows. (a) Nomex. (b) Metamaterial.

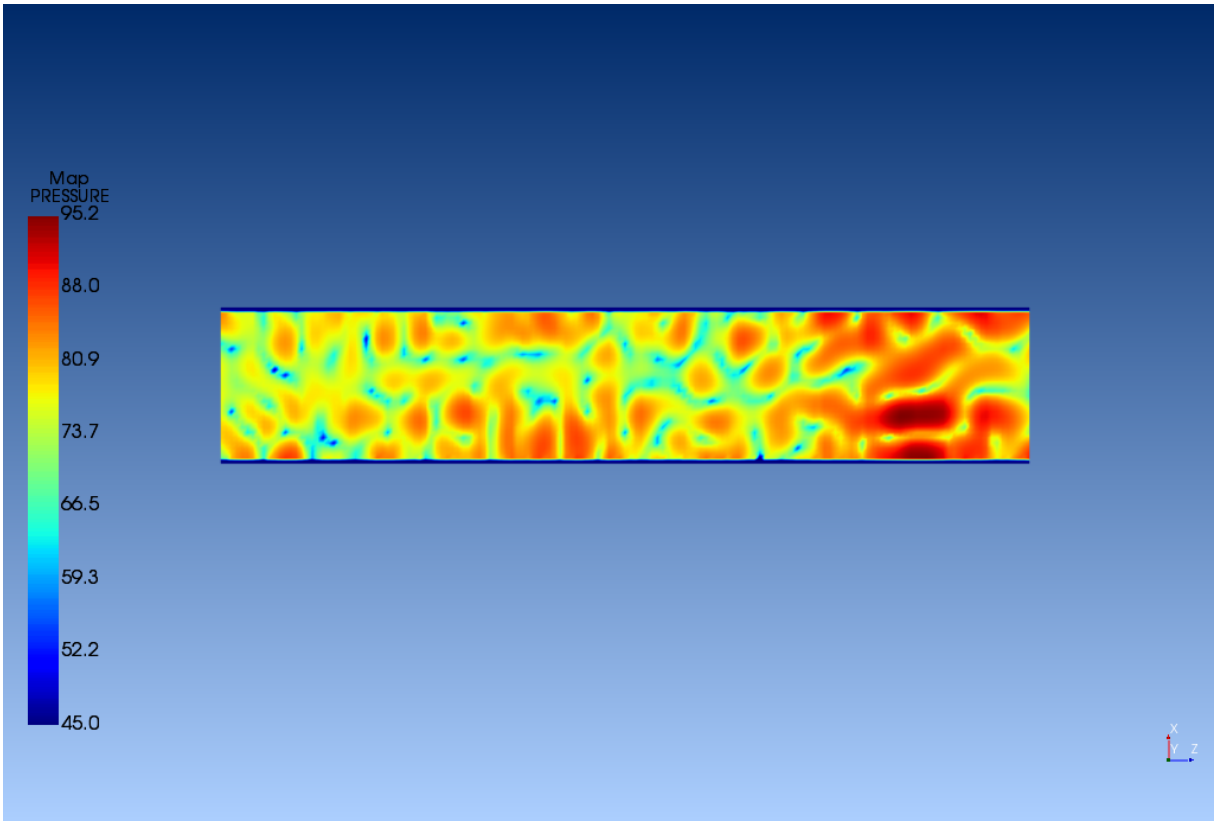

(a)

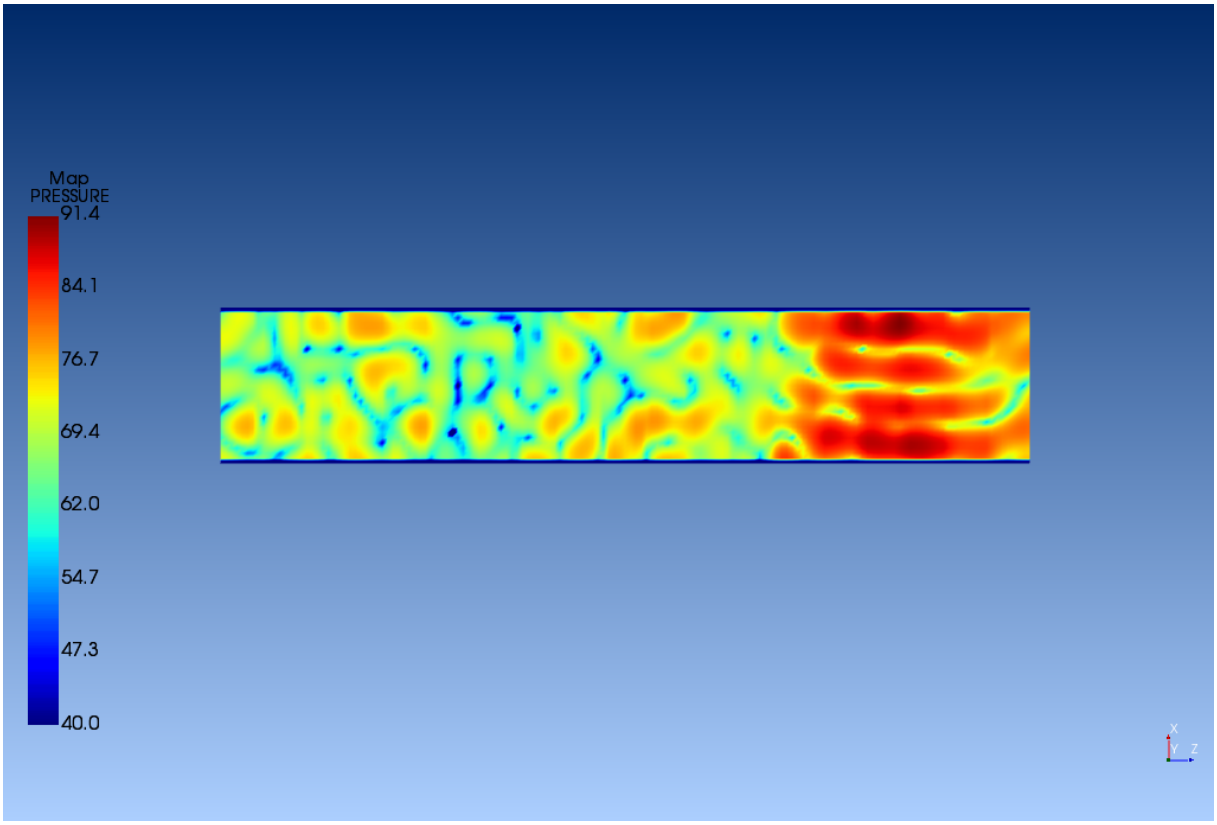

(b)

Figure 5.7: SPL maps at 300 Hz in dBA for a windowless configuration. (a) Nomex. (b) Metamaterial.

Conclusions

The use of metamaterials, to shield the external noise produced by the propeller, leads to a significant reduction of cabin noise, with a consequential increase of passengers comfort. The windowless configuration, from acoustic point of view, does not exploit advantages like it does in terms of fuel consumption and emissions reduction.

These analysis are made under the following starting hypothesis and simplifications:

- vibroacoustic assumptions as explained in section 2.4 about the behavior of the fluid and of the structure;
- approximations linked to the finite elements method and with Actran's solver;
- acoustic pressure loads are produced only by propellers, we do not include other acoustic sources, outside or inside the aircraft;
- the computational model has some simplifications, the air gap between the two layers of the windows is not considered; the carpet and the seats are not modeled as porous materials because their materials are not already defined; bulkheads, toilets and galleys are note included.

The performed analysis underlined as the reduction of noise strongly depends on the trim panel material, so this way to proceed could lead to better results. Furthermore the frequency has an important role, in fact while the sound pressure, at low frequency, tends to increase with frequency, the reduction of pressure loads inverts the previous trend and leads to reduction of sound pressure. Moreover the sound pressure level distribution in the cabin seems to assume a more coherent structure with the increase of frequency; in fact at 200 Hz and 300 Hz the loudness region is near the propellers plane, while at 100 Hz the distribution is more chaotic. Finally, using composite material for fuselage panels, it leads to worse acoustic insulation than using traditional aluminum panels. It results that the windows have a similar insulation capability as the fuselage panel, undermining the possible acoustic advantages of a windowless configuration. With an aluminum fuselage there will be a reduction of sound pressure level due to the removal of windows. However, since a windowless configuration is designed to operate at least in the next decade, the use of composite material on the fuselage results more correct and realistic.

This work lays the foundation to further studies, particularly the FEM model could be used to optimize the metamaterials, changing, for example, the volume fraction (the inclusions size and shape), the host or the inclusions material, the panel thickness and laminate layers. Furthermore different configurations could be studied, using other active or passive acoustic solutions. It is also important to make a structural research on the trim panel with metamaterial to satisfy safety and legislative requirements. Analysis at high frequencies must be performed to evaluate

the metamaterials efficiency out of their nominal design range. In the end, the model could be enriched, introducing, for example:

- air gap in the windows;
- porous materials for seats and carpet;
- stowage and luggages;
- loads for more frequencies and for different acoustic sources;
- elements with smaller size or better interpolation to allow analysis at higher frequencies.

For the windowless configuration an analysis on a wider and tiller range could better determine if the sound pressure level decreases or not due to the removal of windows.

Beyond these technological and economical considerations, the proposed concepts could provide a contribution to the global strategies of reducing noise in the cabin and increasing passengers comfort through the use of innovative materials and configurations.

Bibliography

[1] Bassett, Preston R. & Zand, Stephan J. Noise Reduction in Cabin Airplanes, Brooklyn, New York.

[2] Wilby, John F. (1996) Aircraft interior noise. Journal of Sound and Vibration 190, 545-564.

[3] Bullmore, A. J. & Nelson, Philip A. & Elliott, Stephen J. (1990) Theoretical studies of the active control of propeller-induced cabin noise. Journal of Sound and Vibration 140,191-217.

[4] Tichy, Jiri. (1991) Current and future issues of active noise control. Journal of Acoustical Society of Japan (E) 12(6), 255 62.

[5] Tubbs, Randy L. (1999). HETA 99-0060-2766 Continental Express Airlines Newark, New Jersey.

[6] https://europa.eu/european-union/about-eu/agencies/clean-sky2_en extracted on the 14th of March 2019.

[7] https://www.cleansky.eu/regional-aircraft extracted on the 14th of March 2019.

[8] CAbin Systems design Toward passengers welLbEing, CASTLE proposal in Clean Sky 2 joint undertaking.

[9] Cinefra, Maria & Petrone, Giuseppe. (2019). SEA analysis in the cabin of a regional turboprop with metamaterial lining panels. AIAA Scitech Forum. 10.2514/6.2019-1806.

[10] Bertsch, Lothar & Simons, Dick & Snellen, Mirjam. (2015). Aircraft Noise: The major sources, modeling capabilities, and reduction possibilities.

[11] Sir Lighthill, Michael J. (1952). On Sound Generated Aerodynamically. I. General Theory. Proceedings of The Royal Society A: Mathematical, Physical and Engineering Sciences. 211. 564-587. 10.1098/rspa.1952.0060.

[12] Fletcher, Harvey & Munson, Wilden A. (1933). Loudness, Its Definition, Measurement and Calculation. Journal of The Acoustical Society of America - J ACOUST SOC AMER. 5. 10.1121/1.1915637.

[13] W Robinson, D & S Dadson, R. (1956). A re-determination of equal-loudness relations for pure tones. British Journal of Applied Physics. 7. 166. 10.1088/0508-3443/7/5/302.

[14] Basner, Mathias & Babisch, Wolfgang & Davis, Adrian & Brink, Mark & Clark, Charlotte & Janssen, Sabine & Stansfeld, Stephen. (2013). Auditory and Non-Auditory Effects of Noise on Health. Lancet. 383. 10.1016/S0140-6736(13)61613-X.

[15] Engheta, Nader & Ziolkowsky, Richard W. (2006). Metamaterials, physics and engineering explorations. Wiley-interscience, USA.

[16] Chen, Shuang & Fan, Yuancheng & Fu, Quanhong & Wu, Hongjing & Jin, Yabin & Zheng, Jianbang & Zhang, Fuli. (2018). A Review of Tunable Acoustic Metamaterials. Applied Sciences. 8. 1480. 10.3390/app8091480.

[17] Zhang, Xu & Mei, Jun & Yang, Min & H Chan, N & Sheng, Ping. (2008). Membrane-Type Acoustic Metamaterial with Negative Dynamic Mass. Physical review letters. 101. 204301. 10.1103/PhysRevLett.101.204301.

[18] Mei, Jun & Ma, Guancong & Yang, Min & Yang, Zhiyu & Wen, Weijia & Sheng, Ping. (2012). Dark acoustic metamaterials as super absorbers for low-frequency sound. Nature communications. 3. 756. 10.1038/ncomms1758.

[19] Zheng, Li-Yang & Wu, Ying & Ni, Xu & Chen, Ze-Guo & Lu, Ming-Hui & Chen, Yan-Feng. (2014). Acoustic cloaking by a near-zero-index phononic crystal. Applied Physics Letters. 104. 161904-161904. 10.1063/1.4873354.

[20] Fang, Nicholas & Xi, Dongjuan & Xu, Jianyi & Ambati, Muralidhar & Srituravanich, Werayut & Sun, Cheng & Zhang, Xiang. (2006). Ultrasonic metamaterials with negative modulus. Nature materials. 5. 452-6. 10.1038/nmat1644.

[21] Hyeon Lee, Sam & Mahn Park, Choon & Seo, Yong An & Wang, Z & Kim, Chul. (2009). Acoustic Metameterial with Negative Modulus. Journal of physics. Condensed matter : an Institute of Physics journal. 21. 175704. 10.1088/0953-8984/21/17/175704.

[22] Hyeon Lee, Sam & Mahn Park, Choon & Seo, Yong An & Wang, Z & Kim, Chul. (2010). Composite Acoustic Medium with Simultaneously Negative Density and Modulus. Physical review letters. 104. 054301. 10.1103/PhysRevLett.104.054301.

[23] Climente, Alfonso & Torrent, Daniel & Sanchez-Dehesa, Jose. (2010). Sound focusing by gradient index sonic lenses. Applied Physics Letters. 97. 10.1063/1.3488349.

[24] Climente, Alfonso & Torrent, Daniel & Sanchez-Dehesa, Jose. (2012). Omnidirectional broadband acoustic absorber based on metamaterials. Applied Physics Letters. 100. 10.1063/1.3701611.

[25] Garcìa-Chocano, Victor & Sanchis, Lorenzo & Díaz-Rubio, Ana & Martinez-Pastor, J & Cervera, Francisco & Llopis-Pontiveros, Rafael & Sanchez-Dehesa, Jose. (2011). Acoustic cloak for airborne sound by inverse design. APPLIED PHYSICS LETTERS. 99. 10.1063/1.3623761.

[26] Stenger, Nicolas & Wilhelm, Manfred & Wegener, Martin. (2012). Experiments on Elastic Cloaking in Thin Plates. Physical review letters. 108. 014301. 10.1103/PhysRevLett.108.014301.

[27] D'Amico, Giuseppe (2018). Acoustic analysis of passive metamaterials panels using the finite element method and homogenized properties. Master thesis. Politecnico di Torino.

[28] Zaneboni Jason & Saint Jalmes Bruno. (2014). Aircraft with a cockpit including a viewing surface for piloting which is at least partially virtual, United States Patent, Pub. No. US 2014/0180508.

[29] Berth Christian & Hüttig Gerald & Lehmann Oliver. (2008). Research on integrated collimated cockpit visual and flight information system in Proceeding of ICAS 2008 26th International Congress of the Aeronautical Sciences, Anchorage, Alaska, U.S.A.

[30] Liebeck Robert H. (2004). Design of the Blended Wing Body Subsonic Transport, Journal of Aircraft, Vol. 41, No. 1, pp. 10-25.

[31] Van Der Voet Z. & Geuskens F.J.J.M.M. & Ahmed T.J. & Ninaber Van Eyben B. & Beukers A. (2012). Configuration of the Multibubble Pressure Cabin in Blended Wing Body Aircraft, Journal of Aircraft, Vol. 49, No. 4, pp. 991-100.

[32] Bagassi, Sara & Lucchi, Francesca & Persiani, Franco (2015). Aircraft Preliminary Design: a windowless concept. 5th CEAS Air&Space Conference Proceedings, 2015, pp. 1 - 7, paper no. 211.

[33] Bagassi, Sara & Lucchi, Francesca & Moruzzi, Martino C. (2017). The windowless concept: preliminary design of short-medium range windowless aircraft. In proc AIDAA 24th conference of the Italian association of aeronautics and astronautics, paper no. 031.

[34] Bagassi, Sara & Lucchi, Francesca & Moruzzi, Martino C. (2018). Preliminary design of a long range windowless aircraft concept. Project Conference ICAS 2018, Belo Horizonte, Brazil.

[35] Kinsler, Lawrence & Frey, Austin & Coppens, Alan & Sanders, James (2000). Fundamentals of Acoustics. New York: John Wiley & Sons, Inc. p. 126.

[36] Alimonti, Luca (2010). Refined finite element structural models for the vibro-acoustic response of plate-cavity systems. Master thesis. Politecnico di Milano.

[37] Ohayon, Roger & Soize, Christian (2017). Computational Vibroacoustics in Low- and Medium- Frequency Bands: Damping, ROM, and UQ Modeling. Applied Sciences. 7. 586. 10.3390/app7060586.

[38] https://www.mscsoftware.com/en-uk/product/actran-acoustics extracted on the 18th of March 2019.

[39] Free Field Technology (2016). Actran 17 Users Guide Vol. 1: Installation, Operations, Theory and Utilities . FFT, MSC Software Company.

[40] Free Field Technology. (2016). Actran 17 Users Guide Vol. 2: Extended DAT Input File Syntax, FFT, MSC Software Company.

[41] Free Field Technology. (2016). Actran VI 17 Users Guide, FFT, MSC Software Company.

[42] Vitiello, Pasquale & Bianco, Davide & Galasso, Bernardino & Ameduri, Salvatore & Lombardi, Riccardo & Cinefra, Maria & Petrone, Giuseppe & Colangeli, Claudio (2018). Innovative Passive N&V concepts definition, studies and numerical models delivery for optimization. Document n° AIR-CIRA-RPT(O B-4.4.6.2-1)-0001. Clean Sky 2 AIRFRAME ITD.

[43] http://mumps.enseeiht.fr extracted on the 1st of April 2019.

[44] Passabì, Sebastiano (2017). Vibroacustic noise analysis in the fuselage of regional turboprop aircraft using Actran MSC software. Master thesis. Politecnico di Torino.

Acknowledgements

I would like to thank Ing. Giuseppe D'Amico for his help in understanding the aircraft model and in Actran learning process, Ing. Mattia Barbarino and Ing. Pasquale Vitellio of CIRA for their help with the pressure loads files.